AN ABSTRACT OF THE DISSERTATION OF

Matthew Sean O'Banion for the degree of Doctor of Philosophy in Civil Engineering presented on October 12, 2017.

Title: Rigorous 3D Point Cloud Quality Assessment.

Abstract approved: _____

Michael J. Olsen

The capabilities of modern three-dimensional (3D) capture technology such as laser scanning and image-based 3D reconstruction are well suited to enhance the practice and research of civil engineering. However, given the often-overwhelming focus placed on the incredible capabilities of these tools and techniques, it is important to investigate the limitations of these technologies to ensure they are not misused. Currently, limited resources are available to assist in the evaluation of 3D geospatial data quality, which renders it difficult to efficiently quantify, and communicate the limitations of such data.

To this end, this research investigates the occurrence of data gaps in terrestrial laser scanning (TLS)-derived digital elevation models (DEMs), the quality and accuracy of Structure from Motion (SfM) image-based 3D reconstructions, and the inherent positional uncertainty of individual points in a TLS point cloud. Novel approaches for the detection and classification of data gaps, the evaluation of data suitability, and the efficient computation and visualization of per-point TLS point cloud uncertainty will be discussed.

With regards to TLS data gaps, a novel data gap classification methodology for TLS-derived DEMs was developed, which automatically detects and differentiates between occlusion and

dropout-based data gaps (Chapter 2). This methodology facilitates the assessment of TLS survey quality and can be used to determine the location and surface area of pooled water for scientific research. The data gap classification methodology can also be used for efficient quality evaluation of DEMs and subsequent optimization of TLS acquisition strategies (Chapter 3).

In situations where laser scanning results in significant occlusion-based data gaps that are difficult to mitigate, image-based 3D reconstruction (i.e., SfM) is a possible alternative. In support of investigating the capabilities and limitations of SfM-based 3D reconstructions, a suitability evaluation of unmanned aircraft systems (UAS) and handheld camera-based SfM was performed in the context of automated unstable rock-slope assessment (Chapter 4). The evaluation includes both a rigorous accuracy assessment and quality evaluation of SfM-derived 3D geometry. TLS-derived 3D geometry was found to be more accurate; however, using both UAS and handheld camera-based imagery is a viable option for unstable rock slope characterization when tied to rigorous survey control. Nevertheless, concerns such as over-smoothing and inconsistencies question the suitability of SfM reconstruction for reliably detecting small rock-slope changes over time.

Lastly, a TLS point cloud uncertainty visualization framework was developed to intuitively communicate per point uncertainty during interactive 3D visualization (Chapter 5). Uncertainty propagation amongst the points is performed out-of-core using vertex computations in the OpenGL pipeline made possible by OpenGL Shader Language (GLSL) programming. The flexibility of this visualization solution provides the ability to efficiently adjust error parameters and perform visual-sensitivity analyses. The proposed framework was tested on four unique datasets and aided in the development of a new beamwidth-derived range error equation that incorporates laser beam exit diameter.

Rigorous 3D Point Cloud Quality Assessment

by

Matthew Sean O'Banion

A DISSERTATION

submitted to

Oregon State University

in partial fulfillment of
the requirements for the
degree of

Doctor of Philosophy

Presented October 12, 2017
Commencement June 2018

Doctor of Philosophy dissertation of Matthew Sean O'Banion presented on October 12, 2017.

APPROVED:

_____

Major Professor, representing Civil Engineering

_____

Head of the School of Civil and Construction Engineering

_____

Dean of the Graduate School

I understand that my dissertation will become part of the permanent collection of Oregon State University libraries. My signature below authorizes release of my dissertation to any reader upon request.

_____

Matthew Sean O'Banion, Author

ACKNOWLEDGEMENTS

CONTRIBUTION OF AUTHORS

Dr. Michael Olsen contributed with forethought, guidance, and editing of all sections in this dissertation. Dr. Olsen also contributed to the computer algorithms used in Chapters 2 and 3.

Dr. Chris Parrish and Dr. Mike Bailey contributed greatly to my understanding and execution of the work presented in Chapter 5.

Dr. Joseph Wartman contributed to the development of project scope, assisted in data acquisition, the data acquisition section of the text, and performed overall editing for Chapter 4.

Claire Rault participated in data acquisition, contributed to the data processing section, and performed overall editing for Chapter 4.

Dr. Keith Cunningham contributed to project scope development, participated in data acquisition, and performed overall editing for Chapter 4.

Jeff P. Hollenbeck contributed to the discussion of ecological research in the text, and the performed overall editing for Chapter 2.

Michael J. Eddy participated in preliminary data acquisition, algorithm development, and contributed to the manuscript for Chapter 2.

TABLE OF CONTENTS

TABLE OF CONTENTS (Continued)

TABLE OF CONTENTS (Continued)

LIST OF FIGURES

LIST OF FIGURES (Continued)

LIST OF FIGURES (Continued)

LIST OF TABLES

1 INTRODUCTION

The field of modern geomatics continually evolves and is tightly coupled with the fast-paced world of technical innovation. The capabilities and resolution of three-dimensional (3D) capture technology such as laser scanning and image-based 3D reconstruction techniques, including Structure from Motion (SfM), are rapidly improving. In civil engineering, the ability to accurately and finely capture the world around us opens possibilities to understand how the structures we design and build and the terrain and subsurface we build upon behave across a wide range of spatial and temporal scales. Proper use of these advanced geomatics tools requires in-depth knowledge of their limitations in addition to their impressive mapping capabilities.

This dissertation addresses the occurrence of data gaps in terrestrial laser scanning (TLS)-derived digital elevation models (DEMs), the quality and accuracy of SfM image-based 3D reconstructions, and the inherent positional uncertainty of individual points in a TLS point cloud. TLS data is being utilized in an increasing number of engineering and scientific applications (e.g., Williams et al. 2013; Telling et al. 2017). Likewise, creation of SfM-derived point clouds has become extremely popular due to its compatibility with small unmanned aircraft systems (UAS) and low-cost of acquisition relative to laser scanning solutions. Variations in completeness and spatial accuracy of both the point cloud and derived products (e.g., surface models, 3D models, etc.) can have a significant impact on the validity of associated observations and findings. The civil engineering industry has some of the highest standards for quality and accuracy of geospatial products (Olsen et al. 2013) due to the adverse economic implications of relying on poor-quality data (Meneses et al. 2005). In addition to the identification and quantification of geospatial point cloud limitations, it is important to develop appropriate ways of

communicating this information. For the case of TLS point cloud uncertainty, modern computer graphics capabilities can facilitate the development of intuitive, efficient methods of visual communication.

1.1 RESEARCH OBJECTIVES

Limited resources are available to evaluate point cloud data quality at the point level and no published or accepted standard is currently available for the assessment and reporting of TLS and SfM data accuracy. As a result, point cloud data quality is predominately accomplished by evaluating derivative products such as models through limited survey data in conjunction with subjective expert judgement. Even fewer tools exist to quantify and communicate point level uncertainty. Given that both laser scanning and SfM-derived point cloud data quality can vary significantly across a single dataset, identifying and communicating problems in the data is paramount.

The overall objective of the research included in this dissertation is to provide novel solutions for assessing and communicating aspects of 3D point cloud quality including the presence of data gaps and positional uncertainty of point clouds at the point level.

1.2 OUTLINE OF DISSERTATION

The dissertation follows the manuscript format as specified below:

Chapter 2 (Manuscript 1) proposes a novel data gap classification methodology for TLS-derived DEMs. The methodology differentiates between occlusion and dropout-based data gaps. This

methodology can help surveyors assess the quality of their acquisition strategy. It can also be utilized to determine locations of pooled water for scientific research.

Chapter 3 (Manuscript 2) examines how TLS acquisition and DEM creation parameters affect the completeness of TLS-derived DEMs in a technical note. Utilizing the data gap classification methodology proposed in Chapter 2, a preliminary empirical DEM completeness database was developed and used to create a TLS acquisition planning tool.

Chapter 4 (Manuscript 3) provides a suitability evaluation of UAS and handheld camera-based SfM 3D reconstruction for the assessment of unstable rock slopes. In cases where critical regions of a scanned environment are not visible from areas accessible to a TLS scanner, an alternative tool/technique must be used to capture the obscured region(s). Both a rigorous accuracy assessment and quality evaluation of SfM-derived 3D geometry are performed based on a comparison with TLS-derived data.

Chapter 5 (Manuscript 4) proposes a flexible, intuitive, interactive, and efficient solution for communicating TLS per point uncertainty during 3D visualization through the use of OpenGL Shader Language (GLSL) programs (shaders).

Chapter 6 provides general conclusions, overall contributions, and future work relevant to this dissertation.

The Appendices of this dissertation includes the following supplemental resources:

- Appendix A: TLS acquisition planning tool Matlab script
- Appendix B: GLSL shader code for TLS point cloud uncertainty visualization in *Displaz*

1.3 REFERENCES

Meneses, A. S., Chasco, F. R., García, B., Cabrejas, J., and González-Audícana, M. (2005). "Quality Control in Digital Terrain Models." Journal of Surveying Engineering, 131(4), 118–124.

Olsen, M. J., Roe, G. V., Glennie, C., Persi, F., Reedy, M., Hurwitz, D., Williams, K., Tuss, H., Squellati, A., and Knodler, M. (2013). Guidelines for the Use of Mobile LIDAR in Transportation Applications. NCHRP, Transportation Research Board (TRB).

Telling, J., Lyda, A., Hartzell, P., and Glennie, C. (2017). "Review of Earth science research using terrestrial laser scanning." Earth-Science Reviews, 169, 35–68.

Williams, K., Olsen, M. J., Roe, G. V., and Glennie, C. (2013). "Synthesis of Transportation Applications of Mobile LIDAR." Remote Sensing, 5(9), 4652–4692.

Manuscript # 1

Data Gap Classification for Terrestrial Laser Scanning-Derived Digital Elevation Models DEMs

Matthew S. O'Banion, Michael J. Olsen, Jeff P. Hollenbeck, and Michael J. Eddy

2 DATA GAP CLASSIFICATION FOR TERRESTRIAL LASER SCANNING-DERIVED DIGITAL ELEVATION MODELS

2.1 ABSTRACT

Significant gaps in terrestrial laser scanning (TLS) data can be classified into two principal categories, occlusions and dropouts. Data gaps present in raw TLS point cloud data affect derived products such as 3D surface models and digital elevation models (DEMs), these effects can be problematic for analyses that require interpolation to produce a spatially continuous surface. Ultimately, the relative proportion of occlusions in a TLS survey is indicative of survey quality. Recognizing that regions of a scanned scene occluded from one scan position are likely visible from another point of view, a prevalence of occlusions can indicate an insufficient number of scans and/or poor scanner placement. Conversely, a prevalence of dropouts is not indicative of survey quality, as a scanner operator cannot usually control the presence of specular reflective or absorbent surfaces in a scanned scene. Hence, a need exists for a methodology to determine data completeness by properly classifying and quantifying the proportion of the site that consists of point returns and the two types of data gaps. Knowledge of the data gap origin can facilitate the judgement of TLS survey quality as well as identify pooled water when water reflections are the main source of dropouts in a scene. For example, identification of pooled water is important for ecological research, such as habitat modeling. The proposed data gap classification methodology was applied to DEMs for two study sites: a controlled test site established by the authors and a research site located on the Oregon coast (Rabbit Rock). The Rabbit Rock Site is a rocky intertidal environment that offers many challenges when acquiring TLS-derived topography. The results of the data gap classification methodology were used to

validate the proposed methodology and evaluate its application to a real-world research location. Results for the controlled test site indicate successful classification of occlusions and dropouts. Promising results were achieved with respect to identification of pooled water throughout the Rabbit Rock Site.

2.2 INTRODUCTION

Data gaps/voids (i.e., the absence of data) are a common occurrence that plague remote sensing data including terrestrial laser scanning (TLS) 3D point cloud data. TLS point cloud data gaps can have an adverse effect on subsequent point cloud-derived products, including digital surface models (DSMs), bare-earth digital elevation models (DEMs), triangulated surface meshes, and 3D solid models, among others. A point cloud data gap is unable to provide geometric or radiometric information to the chosen spatially continuous product; therefore, assumptions must be made to span the data gap, which inherently adds uncertainty to the derived product.

TLS data gaps stem from two primary sources (Figure 2-1): a line-of-sight obstacle resulting in an occlusion, and a dropout ("LiDAR Glossary | AGRG" 2017) resulting from a specular reflective or absorbent surface preventing the energy from a given laser pulse from returning to the TLS instrument. The extent of 3D point cloud data gathered by a TLS instrument is limited to what is directly visible by the scanner; line-of-sight obstacles (e.g., topographic high points, trees, etc.) result in occlusions on the side of the obstacle opposite the scanner. Hence, a comprehensive survey of a complex site requires multiple scan positions from varied points of view to mitigate occlusions (Telling et al. 2017). TLS data gaps can also stem from bodies of water (Höfle et al. 2013) and other specular reflective or highly absorbent surfaces. If the surface

of an object is such that a laser pulse emitted by the scanner is received and then reflected away never to return to the scanner, no point will be recorded at the current location in the scene and a data gap will result. Although dropouts can be difficult to distinguish from occlusions, the distinction between the two is important.
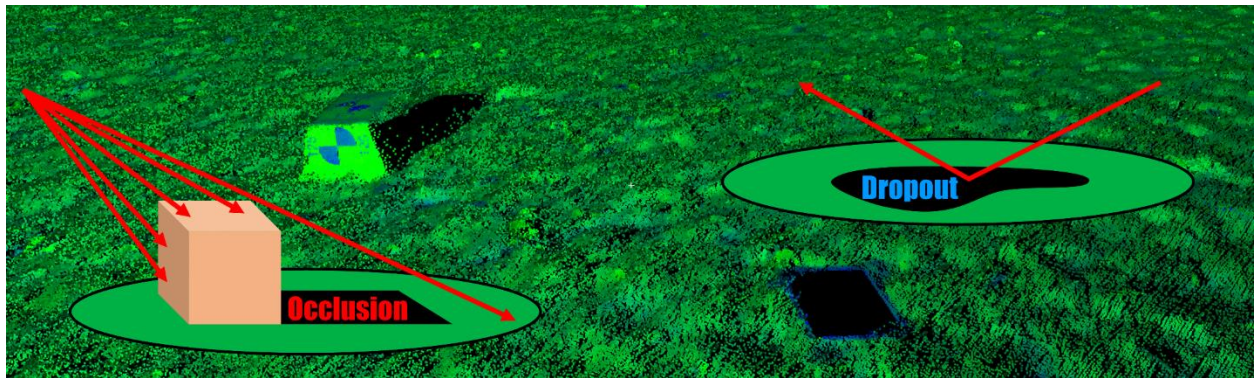
Figure 2-1: Examples of occlusion and dropout-based data gaps in TLS data.

The relative proportion of occlusions in TLS data is often indicative of the survey quality. Recognizing that regions of the scanned scene occluded from one scan position are commonly visible from another location, a prevalence of occlusions in point cloud data can indicate an insufficient number of scans and/or poor scanner placement. Conversely, a prevalence of dropouts is not tied as closely to survey quality. Generally, the scanner operator cannot control the presence of specular reflective or absorbent surfaces, be they water puddles, ponds, large bodies of water, or glass at certain incidence angles. Consequently, data gaps resulting from dropouts typically cannot be avoided by even the most careful and comprehensive of TLS surveys. In some cases, however, the timing of the survey, particularly in locations with tidal or seasonal fluctuations, can have a substantial influence on the presence of pooled water and can be considered.

To date, there is a lack of literature concerning both the identification and classification of data gaps in TLS data as well as TLS-derived products. Existing work has explored data gap filling methods (e.g., Olsen et al. 2015) and mitigation of occlusions (Telling et al. 2017); however, no prior work has been identified that differentiates between occlusion and dropout data gaps.

With respect to the classification of water, the literature seems to solely focus on applications relevant to airborne laser scanning (ALS) (Höfle et al. 2009; Smeeckaert et al. 2013; Wei et al. 2016; Deshpande and Yilmaz 2017). Unfortunately, methods for identifying and/or classifying bodies of water in ALS data are not relevant to TLS point cloud data due to differences in airborne and terrestrial points of view relative to horizontally oriented bodies of water. For instance, it is common in ALS data to have some points representative of the water surface with both low and very high laser pulse energy levels (intensity). Whereas, because of the commonly oblique incidence angle of TLS observations to the ground surface, it is likely no water surface points will be captured.

An important quality metric for TLS point cloud data and derived DEMs is completeness. Given that the presence of any data gaps in a point cloud can bring the survey quality into question and lead to increased levels of DEM uncertainty from over-interpolation, a need exists for a methodology to properly classify these data gaps, and quantify how much of the scanned area consists of point returns as well as the two types of data gaps. Knowledge of data gap origin can facilitate the judgement of TLS survey quality and the identification of pooled water in a scanned scene. An important quality metric for DEMs is completeness. Having the ability to quantify the presence of occlusions in a DEM provides the opportunity to evaluate the influence of TLS data acquisition and DEM creation parameters on the overall completeness of a given DEM. The

proposed methodology can also help inform gap filling/interpolation processes used in development of derivative products; as well as, communicate important information to those using the products. For example, identifying pooled water has implications for habitat modeling and mapping in ecological research. In particular, for species that respond substantially to variation in the submergent-emergent boundary.

As a result, we have developed a novel data gap classification methodology that includes two major steps. The first of these steps flags the boundaries of dropout-based gaps in a projected 2D representation of the point cloud data (2D TLS Image) while the second step uses the flags to classify the individual data gaps present in a TLS-derived DEM. We then apply this methodology to a field site located in the rocky intertidal ecosystem to assess a real-world application.

2.3 METHODOLOGY

The proposed methodology consists of two steps: identification of dropouts, followed by classification of individual data gaps as either occlusions or dropouts. Currently, all code for the data gap classification methodology is written in C/C++ for efficiency. A flow chart representing the proposed data gap classification methodology is presented in Figure 2-2.
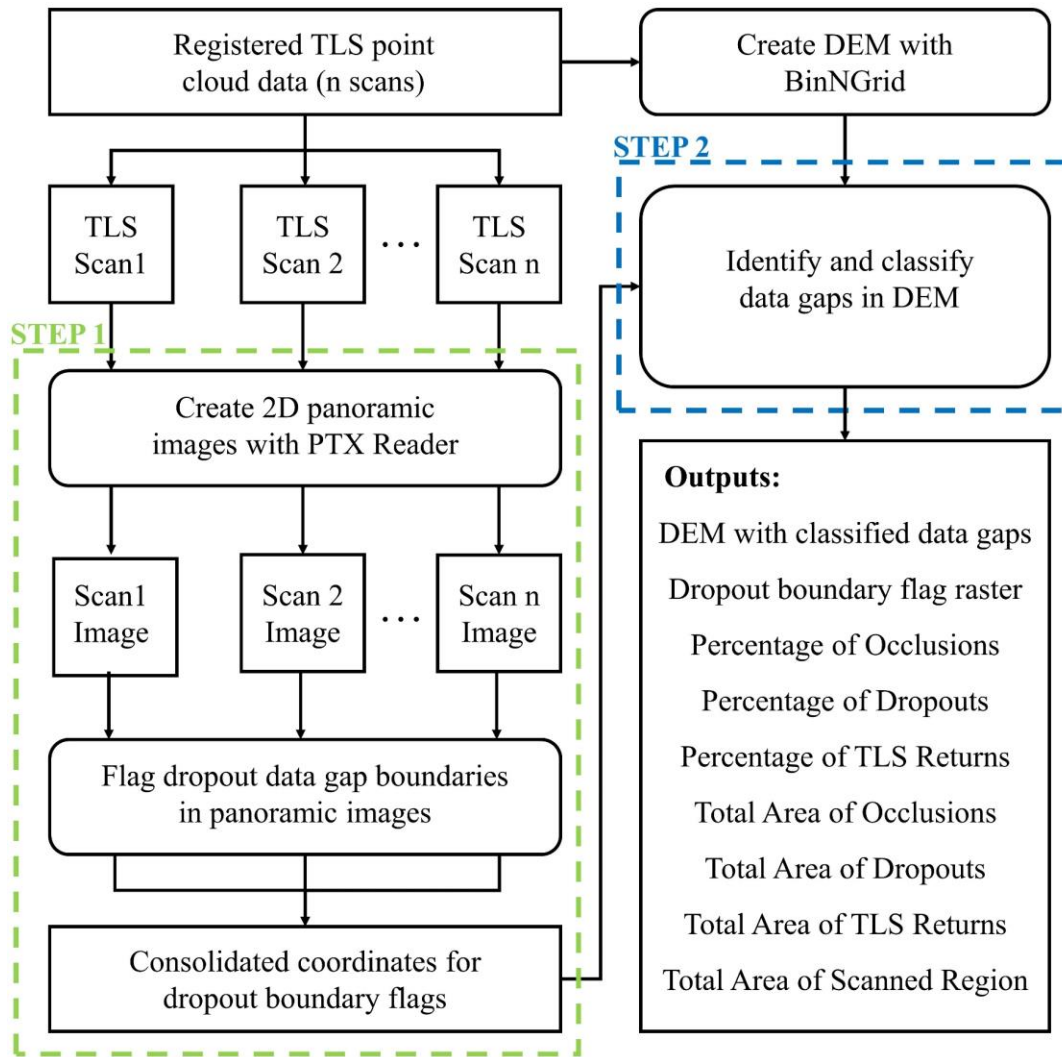
Figure 2-2: General flow chart for the proposed data gap classification methodology

This data gap classification methodology requires the scan data to be organized based on the data acquisition pattern, meaning the gridded structure/order in which the point returns were collected by the scanner must be preserved in the individual registered scans. For this study, the text-based PTX format (*Leica Cyclone 8.0 Help* 2014) was used, which supports the grid structure. Alternatively, the ASTM E57 (Huber 2011) format also preserves this information. The vertical scan lines can be reconstructed as a 2D panoramic image (Figure 2-3) that represents the point of view (POV) from the scanner origin where each pixel in the image is a point return. the TLS

instrument used for this study (Riegl VZ-400) collects points in a spherical coordinate system. With each pixel representing a point return, pixels in the TLS 2D image also have associated XYZ coordinates in the chosen reference frame. Pixels of the image in Figure 2-4 colored in shades of gray represent point cloud data colored by intensity and the blue pixels represent data gaps. With an individual scan represented as a panoramic image, 2D image processing can be utilized to identify features within the scan data (Barnea and Filin 2007; Olsen et al. 2010; Mahmoudabadi et al. 2016).
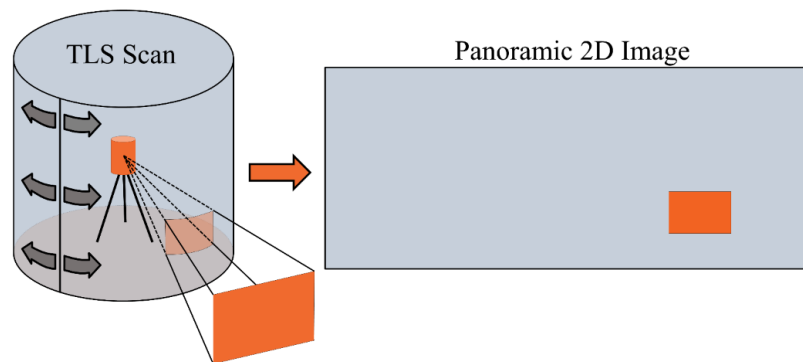
Figure 2-3: Conceptual depiction of projecting TLS data from native cylindrical coordinate system to panoramic 2D image.

Figure 2-4: Example of a TLS 2D panoramic image, colored by intensity (grayscale). Black pixels indicate that there were no returns and are present in the sky and in locations covered in water.

2.3.1 Identify Dropout Data Gap Boundaries – Step 1

Step 1 utilizes the TLS 2D image. Because the TLS image generated for each scan represents the scanner's POV, data gaps caused by occlusions are not visible in the image. However, dropout data gaps are visible, and therefore the boundaries can be identified.

Prior to flagging data gap boundaries in the TLS image, vertical passes through the imagery are performed to minimize the identification of data gaps along the near and far extents of the scanned scene, which correspond to the bottom and top of the TLS image, respectfully. The vertical passes are performed by iterating through the top and bottom rows of the image and for each column moving both in a top-down and bottom-up fashion, tagging each data gap pixel until a valid return pixel is reached. The result of the vertical passes is indicated by the green regions in Figure 2-5.
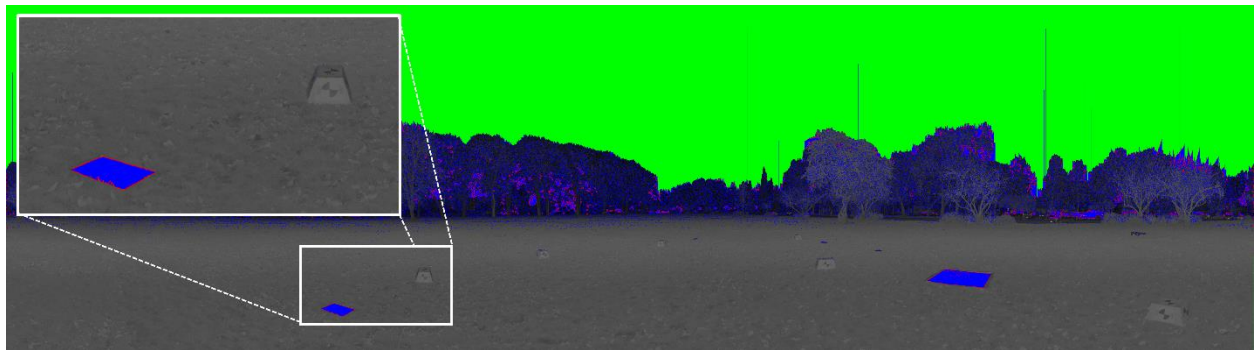
Figure 2-5: Example of a TLS 2D image with data gaps (blue), flagged dropout boundaries (red), and top and bottom vertical scan (green).

These green pixels are ignored during subsequent dropout boundary flagging, which reduces the amount of total flagged dropout pixels by minimizing the quantity of flags generated from long range-derived dropouts and those caused by the laser grazing distant topography at large incidence angles. As for the bottom-up passes, ignoring these pixels ensures that the scanner-

based occlusion found beneath a given scan position is not surrounded by flags and potentially misclassified as a dropout. The assumption is that the scanner would normally be setup over dry land.

Pixels that lie on the boundary of dropouts (Figure 2-4) are identified using a 3x3 pixel roving window (modified for image boundary pixels). For a given pixel in the TLS image, all nine neighbors are checked to see if any are no-data pixels (data gap). If greater than four of the neighboring pixels have no data, the current pixel is flagged as a dropout boundary point. A four-pixel threshold omits small (1-5 pixel) spurious dropouts that do not represent significant data gaps. Following identification of all significant dropout pixels, the XYZ coordinates for each flagged pixel are exported to a text file.

2.3.2   Classification of Data Gaps – Step 2

The list of dropout data gap boundary coordinates generated in Step 1 are analyzed with a TLS-derived DEM in Step 2. It is critical that the coordinate reference frame for the DEM and the boundary flags are consistent.

To begin, a unique ID must be assigned to each significant data gap in the DEM. Insignificant data gaps (e.g., spurious single cell/pixel gaps) are omitted from the ID assignment process via a neighbor check. If a given "no data" cell does not have at least four neighbors that are also "no data" cells, it is not further analyzed. This second wave of omitting small data gaps from the classification processes reduces the occurrence of classifying spurious data gaps as dropouts when they are in close proximity to dropout boundary flags. DEM pixels that are found to be part of a significant data gap are grouped together and assigned an ID using a two-pass Connected

Components algorithm (Dillencourt et al. 1992) and (Fisher et al. 2017). The first pass iterates through the grid from left to right and top to bottom examining the four neighboring DEM pixels found to the left and above the current pixel. Based on the following conditions a label ID for each pixel is generated: if all four neighboring pixels are zero, a new label is assigned to the current pixel; if only one neighbor has a non-zero label, its label is assigned to the current pixel; lastly, if neighboring pixels have different labels, assign one of them to the current pixel and record the equivalency with the other labels. Following the assignment of labels, the occurrence of any adjacent cells with differing labels (equivalencies) are recorded in a lookup table for later use (second pass). The first pass results in all pixels receiving a label; however, contiguous regions might still contain multiple label IDs. Following a convention that favors the minimum label for a region, a second pass is conducted in which the lookup table is used to consolidate label IDs. The resulting connected components raster represents each contiguous cluster of cells with a unique ID that can be queried for later processing and analysis.

Using the unique ID, each data gap is spatially compared against a dropout boundary raster. The dropout boundary raster is a binary raster where cells assigned a "1" coincide with a location where a dropout boundary flag exits. Creating a dropout boundary raster from the individual flag coordinates reduces the quantity of flag data since numerous flags will likely exist within a cell based on the selected DEM resolution and the observation of the boundary from multiple scan positions. The algorithm then iterates through the dropout boundary raster and classifies data gaps that are surrounded by flags as dropouts. To minimize the chances of large occlusions being misclassified based on the presence of a small quantity of dropout boundary flags, at least 10

dropout flags must be associated with a given data gap to result in a dropout classification. Following classification of dropout gaps, all remaining data gaps are classified as occlusions.

The last step of the classification methodology addresses a situation where a dropout connects with the occlusion formed beneath a TLS scanner position. For example, this occurs if a TLS scan position is placed adjacent to a puddle of water. In the case where a scanner-based occlusion is not filled in from another POV, the occlusion and the connected/intersecting dropout will be fused together by the connected components process and the data gap will be classified as a dropout. Under the assumption that a TLS instrument will likely not be setup in the center of a pool of water, we have included functionality that reclassifies any dropouts beneath a given scan position as an occlusion. The area beneath a scan position analyzed for reclassification is determined based on the field of view (FOV) of the specific TLS instrument used and an assumed scanner height (in this case, ~1.8 m). Areas outside of the scanner-based occlusion maintain their original classification.
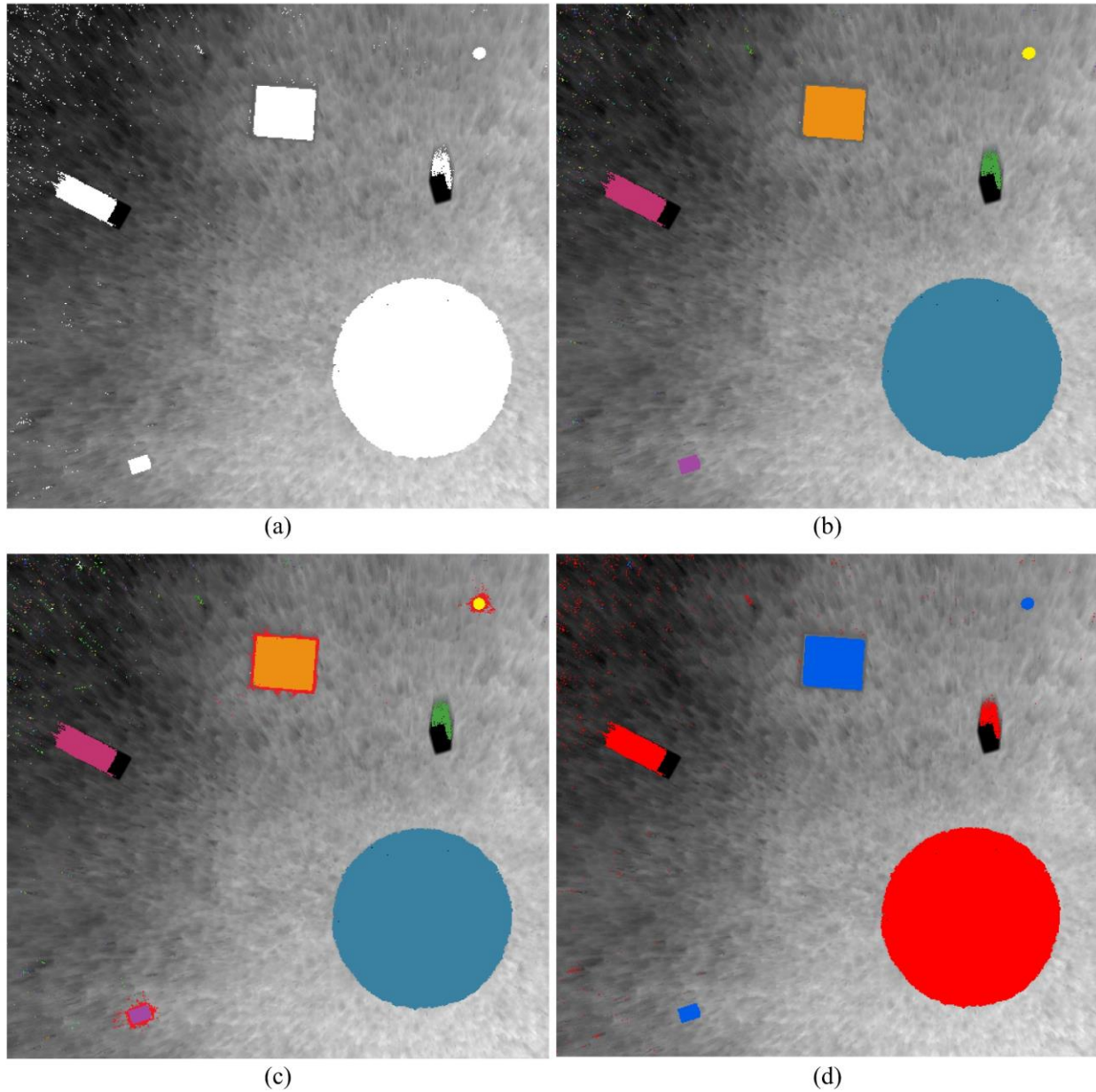
Figure 2-6: Demonstration of the TLS DEM data gap classification methodology. (a) unclassified data gaps in DEM identified in white. (b) Individual data gaps are assigned unique ID. (c) The dropout boundary flag raster (red pixels) is introduced. (d) the dropout boundary raster is used to classify data gaps as either occlusions (red) or dropouts (blue).

Figure 2-6 provides a visual progression of the data gap classification methodology for a controlled test site. Figure 2-6(a) presents the unclassified data gaps (white regions) followed by Figure 2-6(b) where the individual data gaps have been assigned unique IDs indicated by the different colors. Figure 2-6(c) includes the dropout boundary raster (red) used to differentiate between the occlusions and dropouts presented in Figure 2-6(d).

2.4 VALIDATION AND APPLICATION

The proposed data gap classification methodology was applied to two case studies, each evaluating two TLS datasets with different quantities of scans. The TLS datasets for the first case study were acquired in a controlled test site and were used for validation of the data gap classification methodology. TLS data for the second case study were acquired in a natural environment known as Rabbit Rock, a rocky intertidal site located on the Oregon Coast. The Rabbit Rock site serves as an example of applying the data gap classification to a real-world site in support of ecological research.

2.4.1 Test Site

The controlled test site was a rectangular area established in a flat, grassy field, measuring approximately 15 m x 20 m (Figure 2-7). Six cardboard boxes and six shallow receptacles filled with water were placed in the scanned area to generate occlusion and dropout data gaps, respectively. For the purposes of this study, TLS data were acquired from five scan positions (Figure 2-8) at an angular resolution of 0.02°. The TLS data were used to create two separate DEMs of the test site. The first DEM only used data from the one scan position located in the center of the site, and the second DEM used data from four scan positions located at each corner

of the site. A preliminary registration (initial orientation) of the four scan positions was completed using the black & white paper targets attached to the faces of the cardboard boxes. A final registration was performed using a cloud-to-cloud registration technique implemented in the PointReg v.3 software (Olsen et al. 2011). Creating a DEM using only the center scan position ensured the DEM would contain significant occlusion and dropout data gaps that the classification methodology would have to differentiate. Being much more complete, the second DEM does not contain large occlusion gaps, but it offers a second opportunity to validate if the classification methodology is properly identifying the dropout gaps in the scene. TLS data collected at the test site served to validate results of the data gap classification methodology because the location of significant occlusion and dropout data gaps were known. In addition, the surface area of pooled water in the scanned scene was calculated from inner dimension measurements of the water receptacles, which had well-defined shapes.
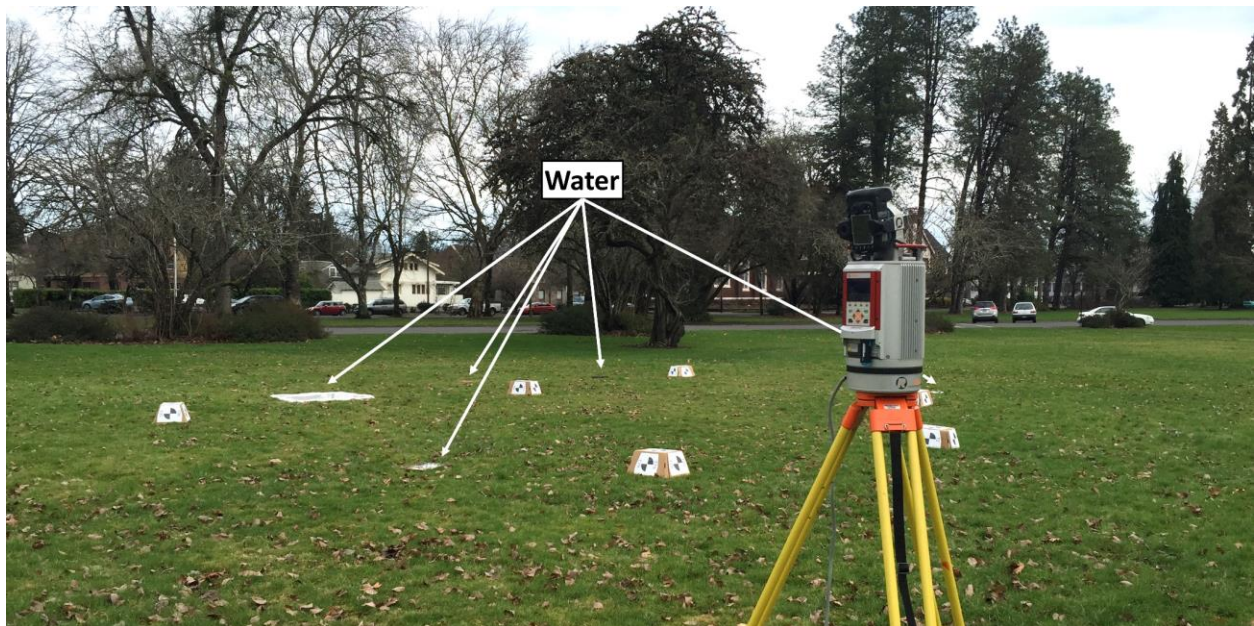
Figure 2-7: Photograph of the test site with the Riegl VZ-400 TLS, cardboard boxes, and water receptacles.
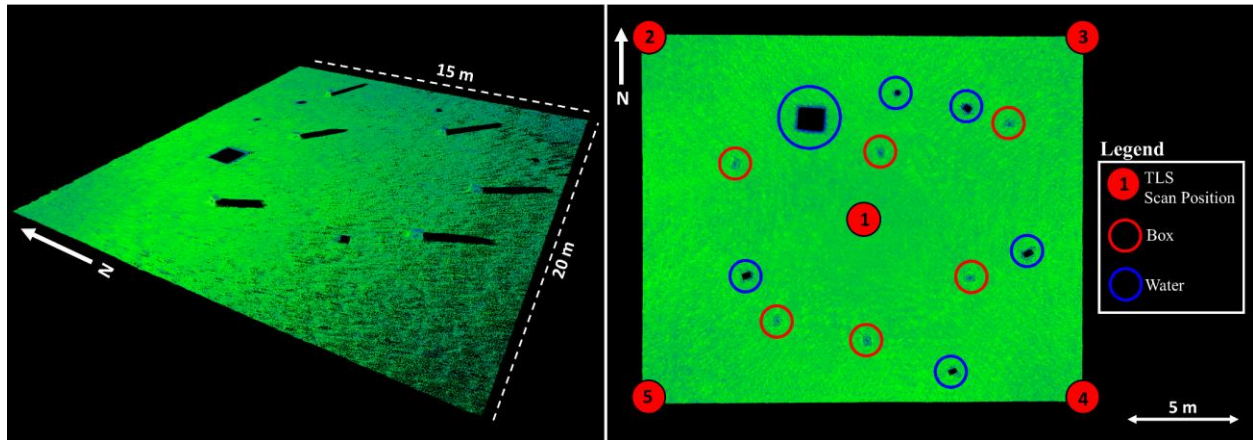
Figure 2-8: Overview of the test site (left) and layout map indicating scan locations and data gap sources (right).

The DEMs generated for the test site were created using the BinNGrid software (Olsen 2011). The DEMs were created with a resolution of 0.02 m, and the elevation for a given pixel was computed using the median elevation from the collection of relevant TLS points. Other elevation computation methods, such as using the minimum, maximum, or mean could have been used; however, this selection does not significantly influence the results with respect to validating the data gap classification methodology.

2.4.1.1 Results and Discussion

Visual inspection of the data gap classification results for the test site DEMs (Figure 2-9) indicate all significant occlusion and dropout data gaps were properly classified. Details of the data gap classification results for the test site are included in Table 2.1. Areas in Figure 2-9 colored in red represent occlusions and areas in blue represent dropouts, which in this case also represent pooled water.

Test Site A   **Test Site B**
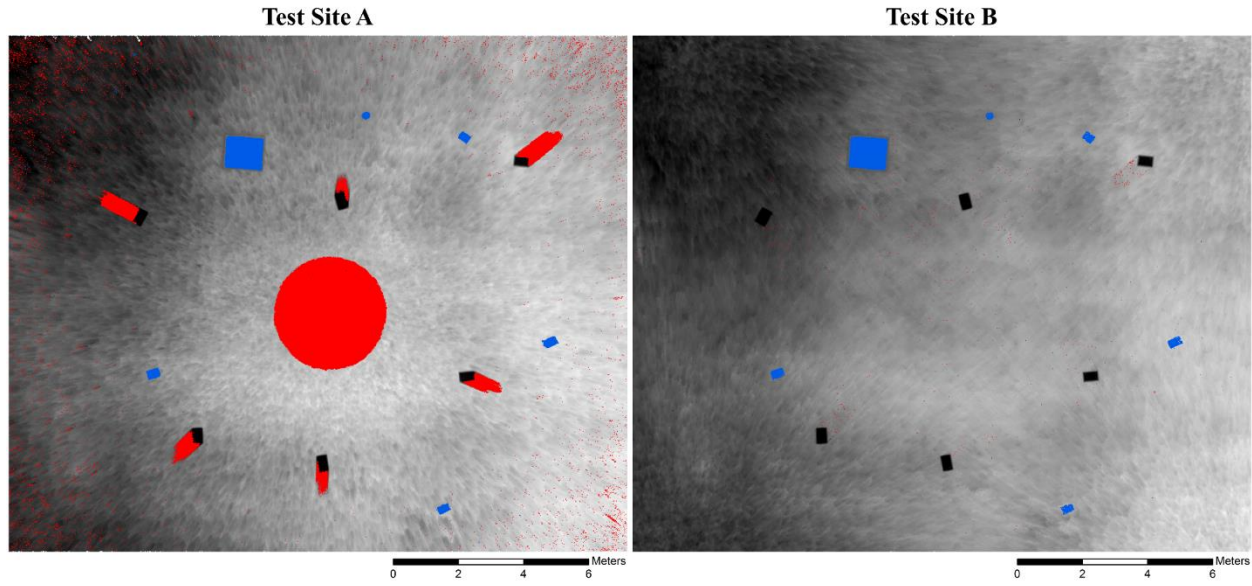
Figure 2-9: Data gap classification results for test site DEM A and DEM B. Areas in red represent occlusions and dropouts are colored blue. Locations of the cardboard boxes are colored black.

Table 2.1: Results of data gap classification for test site DEMs A and B.

Site	% Occlusions	% Dropouts	% Returns	Occlusion Area (m²)	Dropout Area (m²)	Return Area (m²)	Total Area (m²)
DEM A	5.04	0.54	94.42	15.15	1.62	283.81	300.58
DEM B	0.07	0.50	99.42	0.22	1.52	298.85	300.58

For both the one-scan (DEM A) and four-scan (DEM B) position scenarios, the location of the larger data gaps are where one would expect them to be. For DEM A, relatively large occlusions occur behind each of the cardboard boxes where a laser pulse shadow is cast, and beneath the scan position, which is outside the FOV of the TLS instrument. Additional small occlusions are present throughout DEM A that are attributed to laser pulse shadows cast by blades of grass and other small ground cover vegetation. No significant occlusions are observed in DEM B, but small occlusions can be observed throughout the DEM similar to those found in the one-scan

position model. The lack of major occlusions in DEM B is attributed to the acquisition of TLS data from four scan positions with different points of view; what was not seen from one scan position was filled in by another, including the large occlusion in the center of DEM A. Based on the results in Table 2.1, there is a decrease in percentage of occlusions of ~5% when using four scan positions instead of a single scan to capture the test site. This is not a dramatic difference, but also note that the obstacles (cardboard boxes) creating the occlusions in the test site were relatively small. Common obstacles such as trees, cars, and buildings can cause very extensive occlusions, which can occupy the majority of a given scanned scene if additional scans from different positions are not performed. In addition, a second scan from a new position would ordinarily be done to fill in the occlusions below the first scan position.

The total area of dropouts identified for DEM A is 1.62 m^2, which agrees well with the known area of pooled water at the test site of 1.66 m^2. For test site DEM A, the percent difference is ~3%; however, for DEM B it increases to ~9%. An explanation for the discrepancy in dropout area between DEM A and DEM B could be attributed to misalignment (registration error) amongst the four scans used to generate DEM B. Subtle shifts in the TLS data stemming from registration error would always result in the boundary of a dropout to creep into the data gap; thereby causing a decrease in dropout area. The TLS data used to generate DEM A did not require registration because only one scan position was used.

All of the artificial pooled water sources are correctly classified as dropouts in both of the test site DEMs. Additional, small dropouts were identified throughout the DEMs that are likely valid and attributed to varied reflective/absorption conditions in the grass-covered ground surface.

2.4.2   Rabbit Rock Study Site

The Rabbit Rock site is a complex, rocky intertidal environment (Figure 2-10) located along the central Oregon Coast, approximately 3.5 km north of Depoe Bay, OR along Hwy. 101. TLS data were collected at this location on two separate occasions during very low (minus) tides to model and identify foraging habitat for the Black Oystercatcher (*Haematopus bachmanii*), a rocky-intertidal obligate shorebird (Hollenbeck et al. 2014). TLS scan positions 1-14 were acquired on May 18th, 2011 and scans 15-21 were acquired on June 16th, 2011 (Figure 2-11). The second set of scans were acquired to fill in areas of the site inaccessible during the May survey because of higher tidal conditions. All TLS scans were acquired at angular resolutions of 0.03 or 0.05 degrees. Registration and geo-referencing of the point cloud data was performed with a cloud-to-cloud registration technique implemented in PointReg v3 (Olsen et al. 2011) based on GNSS coordinates, sensor inclination, and an estimated yaw angle for the TLS instrument at each scan position. Post-processed GNSS coordinates for the individual scan positions were generated using the rapid-static processing available through the National Geodetic Survey's Online Positioning User Service (OPUS-RS). Two 10 cm TLS-derived DEMs were generated for the Rabbit Rock Site, one using only TLS scans 1-14 (DEM RR1) and the second using data from all 21 scan positions (DEM RR2). Comparing the data gap classification results for DEM RR1 and DEM RR2 enable quantification of the benefit of the additional scans acquired in the second survey. Both DEMs were clipped to identical extents for proper comparison of results. Qualitative validation of the DEM RR2 results was also performed by comparing historical aerial and scanner-based imagery of the site with the classification results to see if the areas identified as water seem reasonable.

Figure 2-10: Undulating rock and pooled water conditions during the TLS survey of Rabbit Rock.
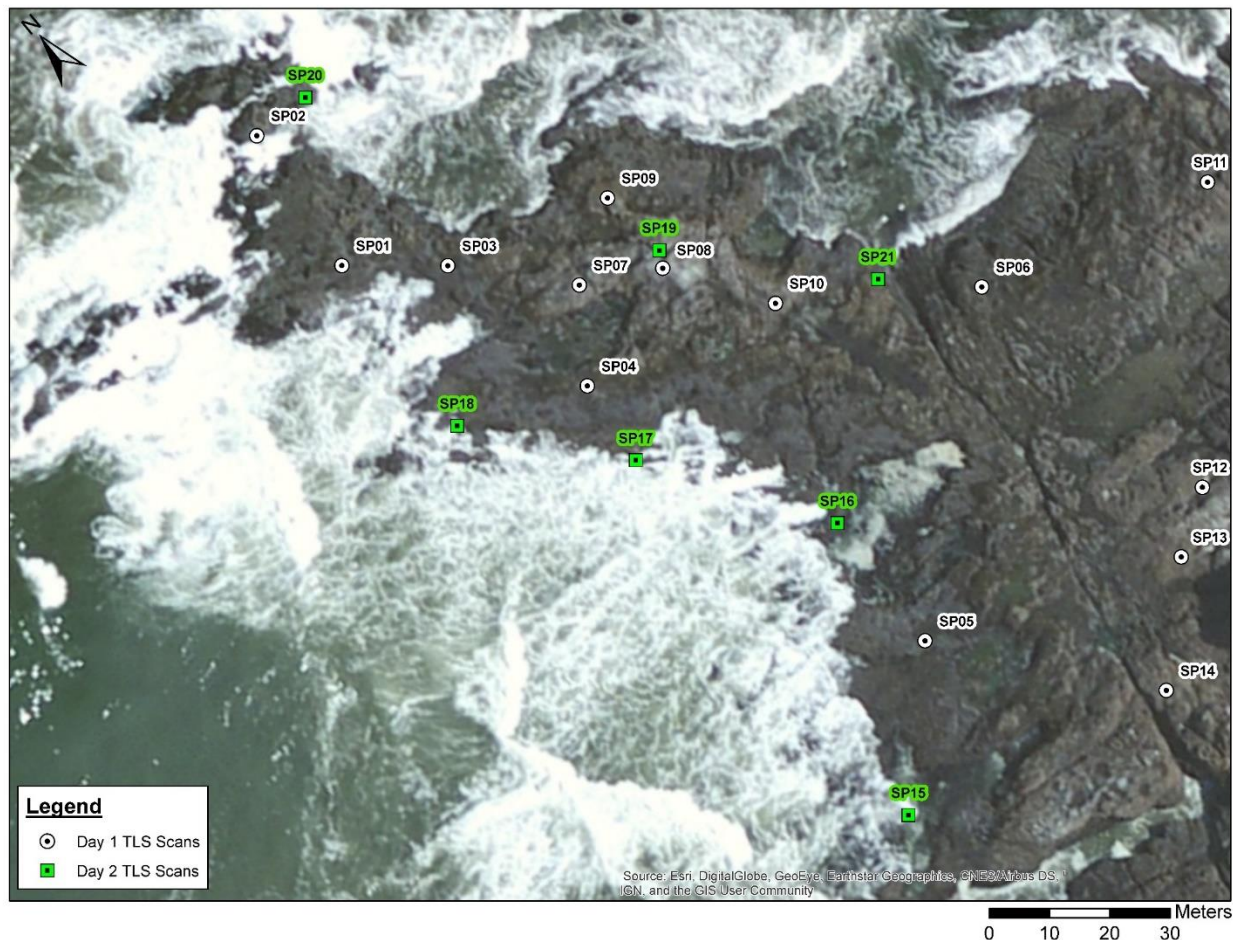
Figure 2-11: Overview map of Rabbit Rock Site with locations of TLS scan positions.

Given the presence of undulating rock and numerous pools of water at the Rabbit Rock Site (Figure 2-10), there are many opportunities for both occlusions and dropouts to exist in the scanned scene.

When examining the Rabbit Rock DEMs with unclassified data gaps, two questions arise: how well was the site captured (TLS survey quality) and what regions of the DEM are occupied by pooled water? The presence of pooled water within the Rabbit Rock Site is important for identifying and modeling shorebird foraging habitat. In the unclassified DEM, occlusions and dropouts caused by pooled water are indistinguishable. To assess the survey quality and identify

regions of the Rabbit Rock Site occupied by pooled water, the proposed data gap classification methodology was utilized.

2.4.2.1 Results and Discussion

The results of data gap analysis for Rabbit Rock DEM RR2 indicate that 1.4 % and 65.8 % of the scanned area is occupied by occlusions and dropouts, respectively. Inspection of the classified DEM (Figure 2-12) reveals the majority of dropouts are attributed to the ocean water surrounding the Rabbit Rock Site. In this case, the outer extent of the ocean-derived dropout is constrained by the chosen boundary of the "scanned area," which in this case is a rectangle fit to the outer boundaries of the TLS data used to generate the DEM. It is important to note that unlike static pooled water, the surrounding ocean water results in dropouts and water surface returns. Due to the heavy wave action, high water turbidity, and presence of sea foam and floating debris (e.g., driftwood, seaweed, etc.) common in an intertidal environment, returns will be registered by the TLS instrument and swaths of noisy points from the constantly changing ocean water surface will be created. In between the TLS points captured on the ocean surface, there will be localized regions where the water surface will create valid dropouts and the boundary of those regions are flagged in Step 1 of the data gap classification methodology. This results in a DEM that is surrounded by a large data gap that extends to the outer rectangular extent of the DEM. When cross referencing this large data gap with the dropout boundary flags, the surrounding ocean water was appropriately classified as a dropout. Prior to performing data gap classification, the initial DEM was trimmed in ESRI ArcMap 10.1 software to minimize the amount of ocean-derived noise. Regardless of the effort to trim the DEM, some ocean wave artifacts still exist, identified by the streak-like features observed along the outer boundary of the

site. To completely remove these wave-based artifacts would require meticulous manual cleaning of the TLS data and/or development of a custom filtering algorithm such as that in Che and Olsen (2017).
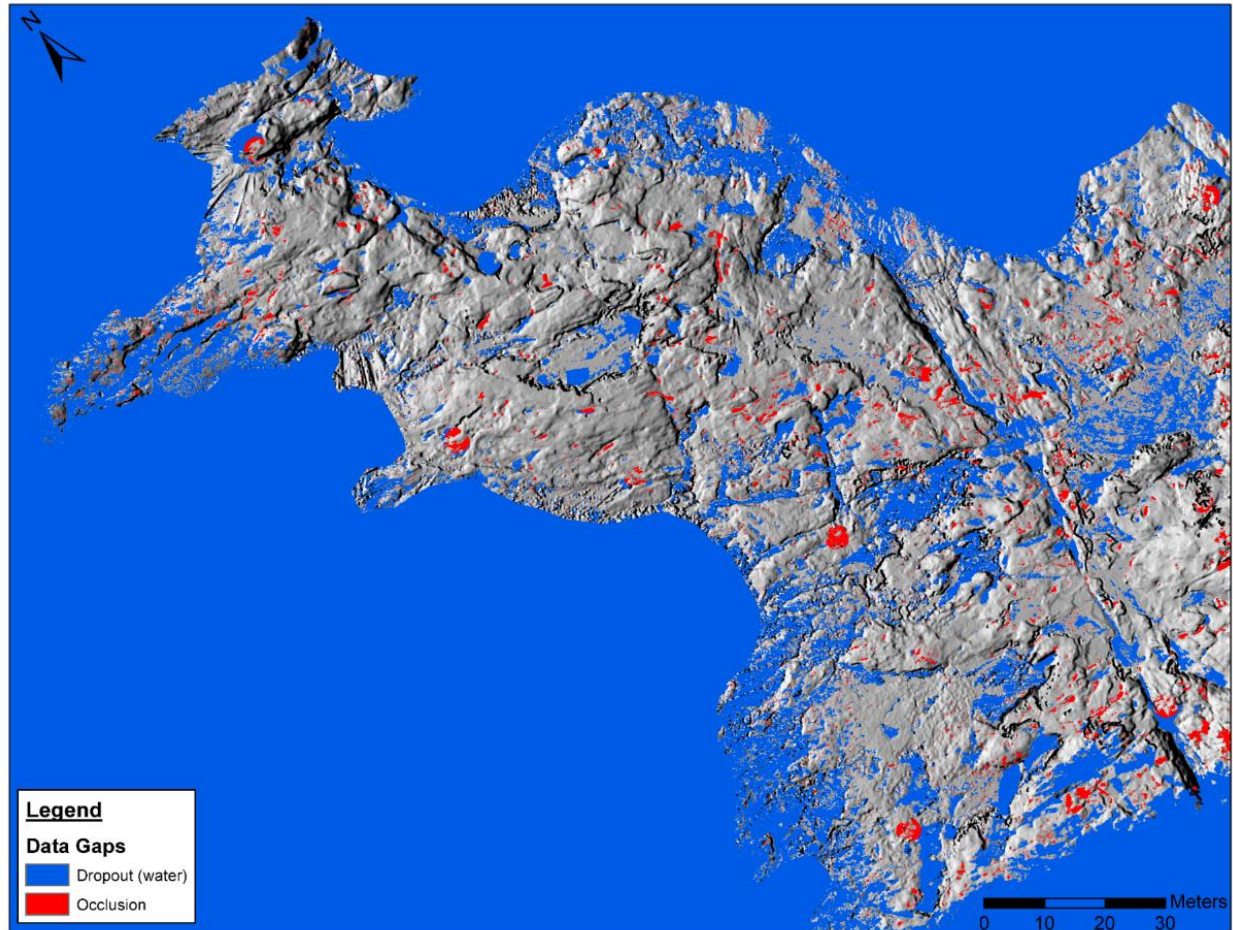
Figure 2-12: Results of data gap classification for the full extent of DEM RR2.

Occlusions identified on Rabbit Rock (Figure 2-12) are observed to be relatively small and more evenly distributed throughout the site when compared to the dropouts. The identified dropouts are observed to be significantly larger in size and are concentrated along the boundary and in the middle of Rabbit Rock. These are areas where the surrounding ocean was able to run-up on the rock surface and generate pools within the numerous topographic low points (i.e., tidepools).

These results are evidence that most of the data gaps were attributed to specular reflections (pooled water) and not occlusions. To reveal the quantities of returns, occlusions, and dropouts on the surface of Rabbit Rock, an approximate boundary was used to remove the surrounding ocean from the classification results for DEMs RR1 and RR2 (Figure 2-13). Results of this analysis (Table 2.2) indicate that for DEM RR1, 61% of the site is occupied by elevation data (TLS returns), 36% is occupied by dropouts, but only 3% is attributed to occlusions. For DEM RR2, 72% of the site is occupied by TLS returns, 25% is occupied by dropouts, and we see the same amount of occlusions at around 3%. Comparing the results for DEMs RR1 and RR2 show that an 11% increase in elevation data coverage was achieved from the second TLS field campaign. Based on the decrease in identified dropouts and the lack of change in percent occlusions from DEM RR1 to RR2, the entirety of the 11% increase in coverage is attributed to filling in areas that were obscured by high water conditions in the previous TLS survey.
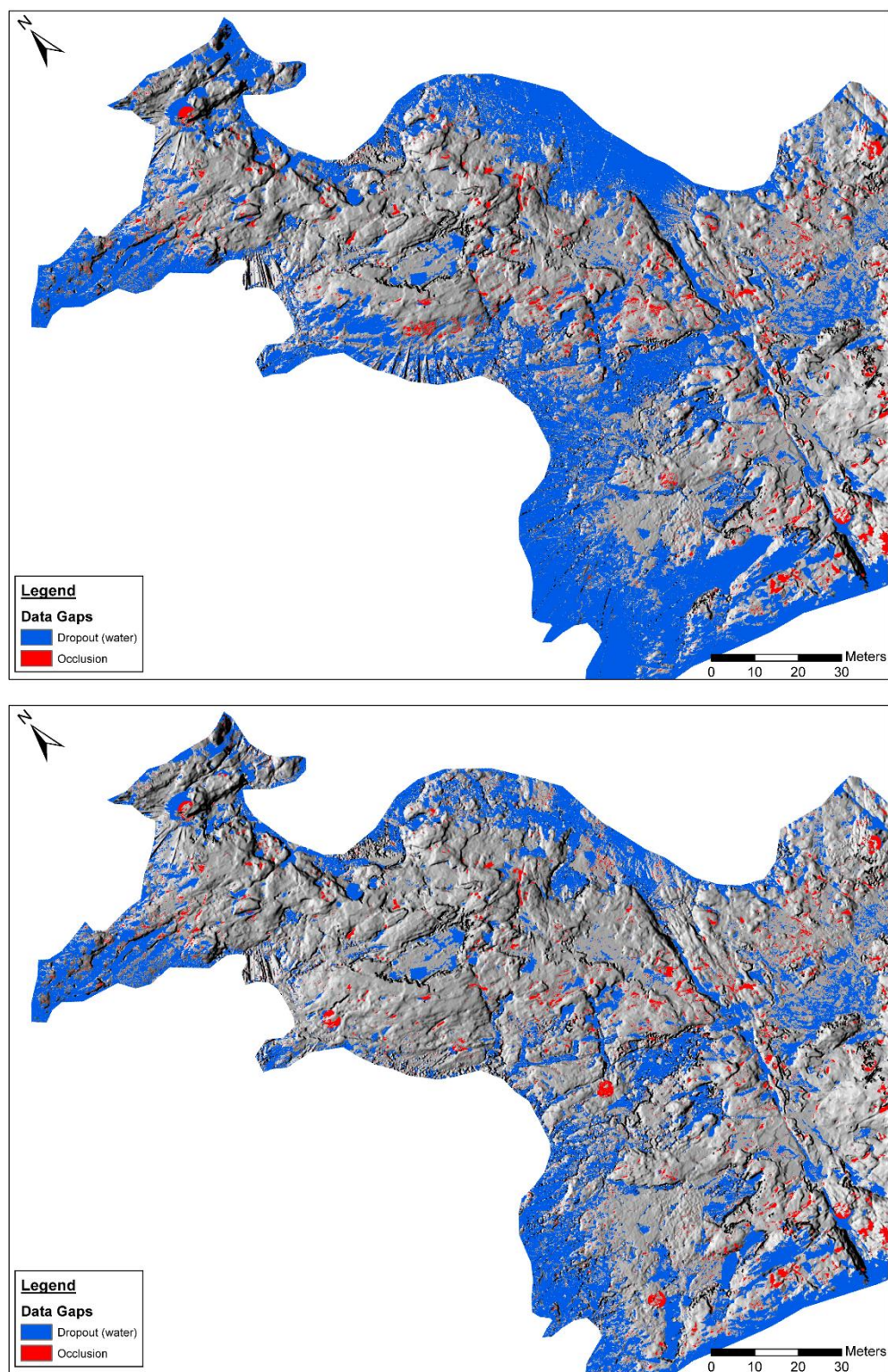
Figure 2-13: Clipped data classification results for DEMs RR1 (left) and RR2 (right).

Table 2.2: Results of data gap classification for the cropped Rabbit Rock DEMs 1 and 2.

Site	% Occlusions	% Dropouts	% Returns	Occlusion Area (m²)	Dropout Area (m²)	Return Area (m²)	Total Area (m²)
DEM RR1	2.68	36.07	61.25	457.3	6,145.27	10,436.54	17,039.12
DEM RR2	2.66	25.21	72.13	453.3	4,294.82	12,290.96	17,039.12

There are a few locations where dropouts were classified in close proximity to a TLS scan location. In these regions, the photographs taken from the scan position can be used to perform a qualitative validation of the results. The TLS-based imagery for scan positions SP15 and SP16 are presented in Figure 2-14. The pools of water visible in the imagery corroborate the classification results of extensive dropouts surrounding the scan positions. Circular occlusions are observed beneath SP15 and SP16 in Figure 2-14 due to other scan positions' inability to fill in these areas. It is important to note that these scanner-based occlusions are adjacent to pooled water, which makes it difficult to determine where exactly the pooled water stops and the occlusion begins. In this case, we have decided to be conservative with respect to judging survey quality; therefore, we assume that all data gaps within a certain radius of a given scan position shall be classified as occlusions. If we wanted to ensure that we were capturing all the potential water pools, we could change the algorithm to classify the entire, merged, data gap as a dropout.
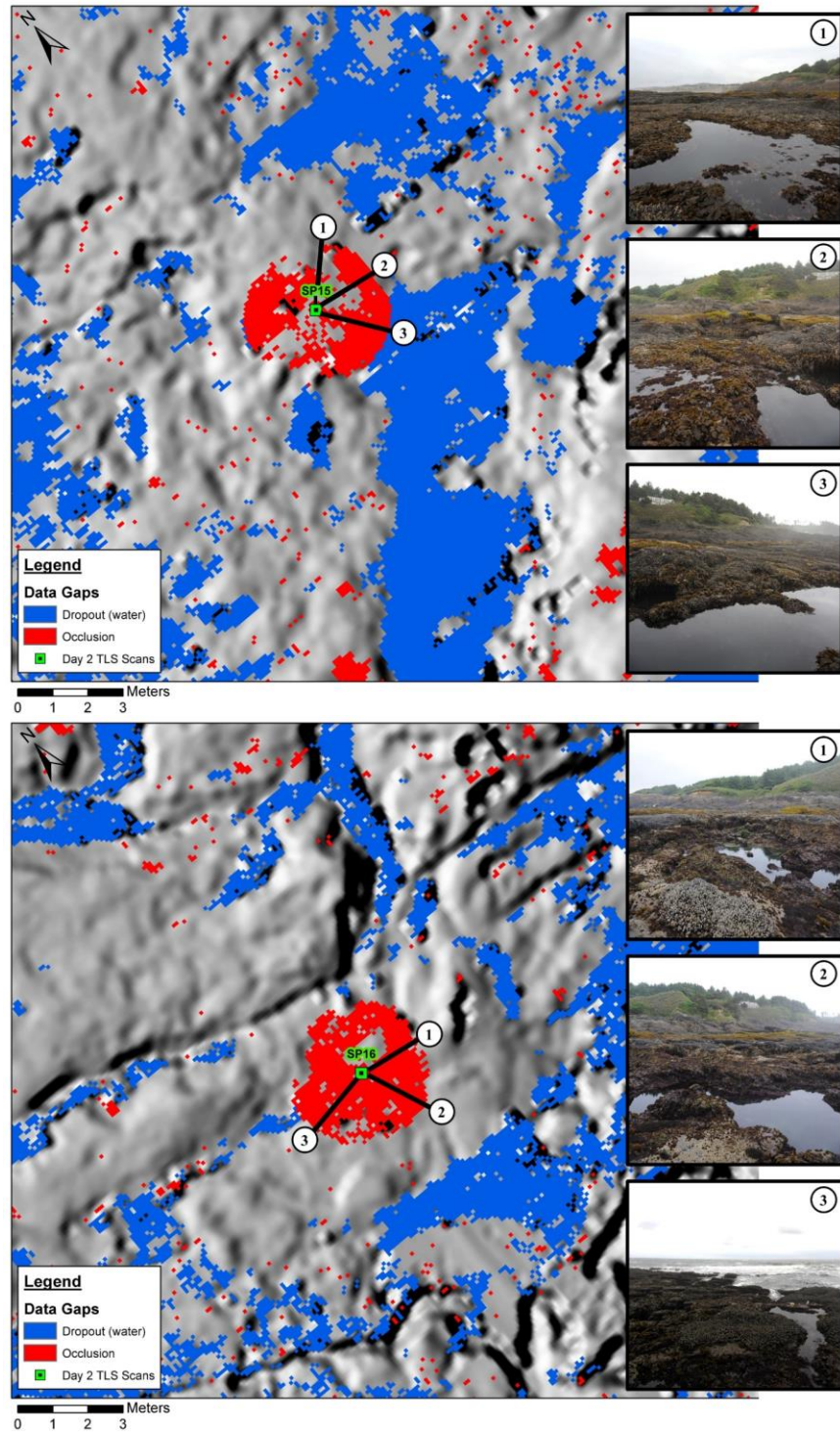
Figure 2-14: Comparison of results with co-acquired TLS scanner-based imagery for scan positions SP15 (top) and SP16 (bottom).

For additional qualitative validation of the Rabbit Rock data gap classification results, National Agriculture Imagery Program (NAIP) aerial imagery was acquired for 2005 and 2009 (Figure 2-15). Cross referencing of the NAIP imagery with the classification results enables us to judge the validity of the identified dropouts. The 2005 and 2009 NAIP imagery present two different water conditions at the Rabbit Rock Site. The 2005 imagery was acquired during a high tide (common issue with coastal aerial image acquisition), causing a significant portion of the Rabbit Rock Site to be submerged under water/breaking surf. The 2009 imagery was acquired during low tide and the majority of the Rabbit Rock Site was exposed. Together, these two NAIP images provide useful insight into how the surrounding ocean interacts with Rabbit Rock; thereby facilitating validation of the data gap classification results.
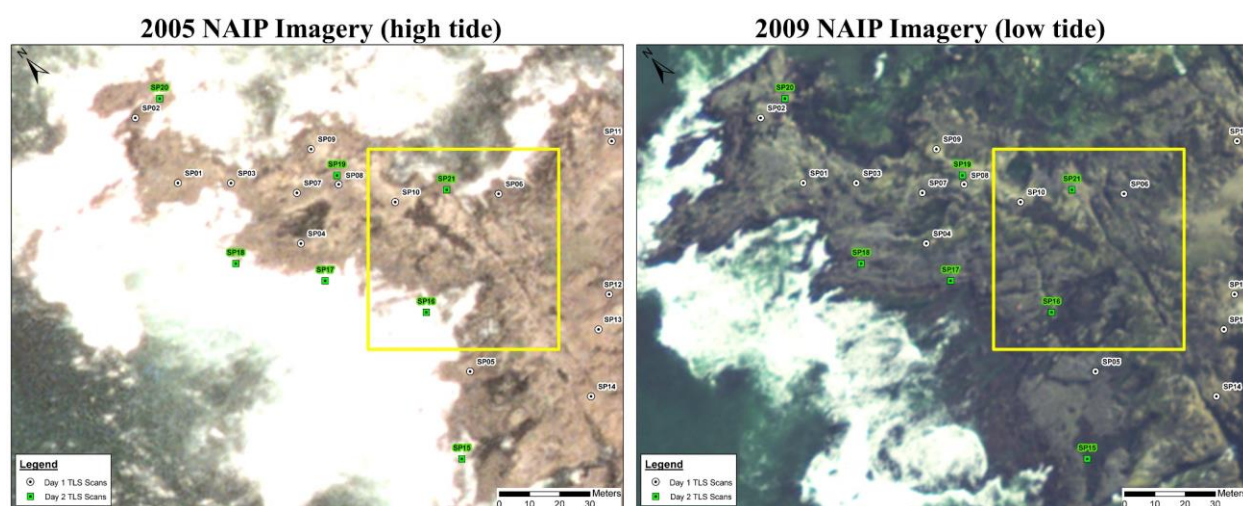
Figure 2-15: 2005 and 2009 NAIP Imagery with yellow inset box that corresponds to Figure 2-16.

2005 NAIP Imagery
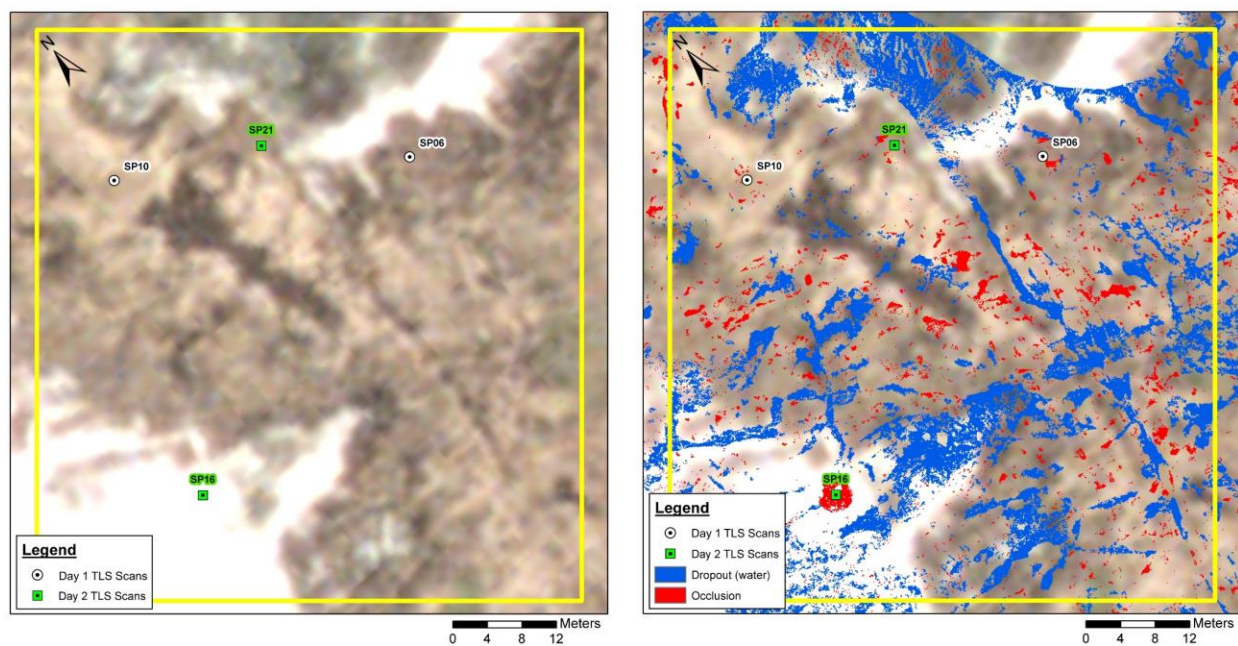
2009 NAIP Imagery
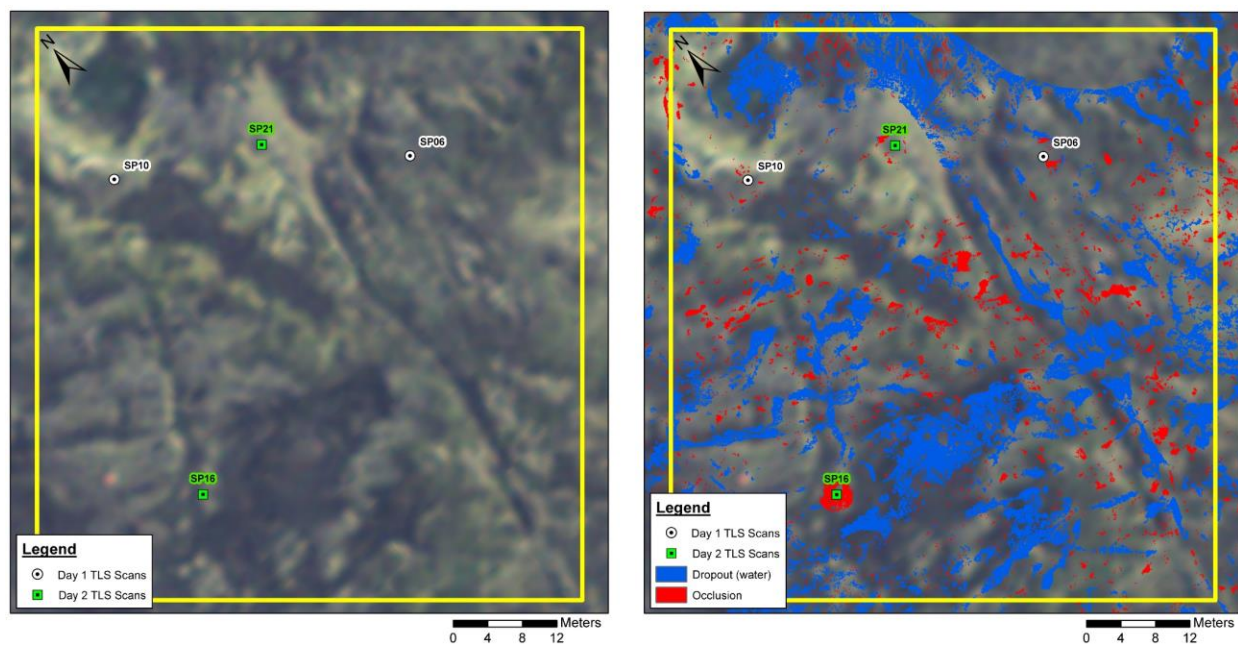
Figure 2-16: Comparison of selected region of 2005 and 2009 NAIP imagery with data gap classification results.

Inspection of the inset region of the Rabbit Rock Site presented in Figure 2-16 indicates concordance between where water is likely to exist and the majority of the identified dropouts. Dropouts also seem to align with areas of the 2009 imagery that are darker in color relative to the surrounding rock. There is a slight offset between the classified data gaps and the dark features; however, this offset is attributed to inconsistencies in geo-referencing between the TLS-derived DEM and the aerial imagery. Based on a review of photographs captured during TLS data collection, the dark regions appear to coincide with topographic low points that contain marine vegetation and algae on their surface due to the frequent presence of water; thus, corroborating the idea that pooled water likely existed there during the TLS surveys.

2.5 CONCLUSION

The proposed data gap classification methodology differentiates between occlusion and dropouts in a TLS-derived DEM using structured TLS point cloud data (PTX), and the associated DEM. The test site results indicate correct classification of occlusions and dropout-based data gaps and identification of a similar surface area of pooled water present in the scanned scene. The results for the Rabbit Rock Site analysis indicate the identified dropouts correlate well with the presence of water and the quality of the Rabbit Rock TLS survey is high given the low percent of occlusions.

For the test site and Rabbit Rock site, the significant dropouts could be attributed to pooled water present in the scanned scene. If this classification methodology were applied to a dataset that included other highly reflective objects (e.g., glass window panes), dropouts could not be solely attributed to the presence of water; however, they would still be separated from the occlusions,

which is important to be able to identify. For assessment of TLS survey quality, data gaps due to dropouts must be identified and removed before the relative percentage of data gaps due to occlusions is determined. The proposed data gap classification methodology enables us to make this required distinction.

In a complex environment such as Rabbit Rock, we can assume the primary source of dropouts is attributed to water. Thus, TLS offers tremendous potential for ecological studies in the rocky intertidal ecosystem. Due to the nature of this highly limited (spatially) ecosystem, TLS-derived DEMs may provide the foundation for scale-appropriate habitat models and simulations. Previous work using TLS-derived DEMs for modeling shorebird foraging habitat demonstrated substantial capability (Hollenbeck et al. 2014). However, a missing key attribute that influenced the development of habitat models was the accurate identification of submergent areas during low tides (i.e., tidepools). Because the rocky intertidal ecosystem is very spatially limited, submergent areas (ostensibly dropouts) may comprise a considerable proportion of total area of interest (see Table 2.2) and become important for subsequent habitat assessments and modeling. Also of importance is the identification of water area (tidepools) boundaries. This interface is a region of many important interactions between the terrestrial and aquatic components of the intertidal ecosystem. For example, the Black Oystercatcher foraging habitat model developed by Hollenbeck et al. (2014) lacked the ability to identify local regions of key prey items (limpets) that congregate at tidepool boundaries. Consequently, the ability to differentiate submergent areas from emergent areas that are exposed to the terrestrial component of the intertidal ecosystem is paramount for scale-appropriate habitat analyses and TLS-derived DEMs, processed to differentiate data dropouts and occlusions, and may hold significant promise for

intertidal research. Previously available methods for delineating these locales often involved intensive field methods or digitizing the DEM or point cloud which requires significant effort and is often not feasible in many ecological studies.

Additionally, knowledge of data gap sources can lead to better understanding of DEM quality and preferred post-processing techniques. An important quality metric for DEMs is completeness. Having the ability to quantify the presence of occlusions in a DEM provides the opportunity to evaluate the influence of TLS data acquisition and DEM creation parameters on the overall completeness of a given DEM. Examples of these parameters include, angular resolution of TLS data, quantity of scans/unit area, DEM resolution, and minimum required points/DEM pixel (Chapter 3). Lastly, classification of data gaps can enable optimizing post-processing techniques such as DEM gap filling. For instance, proper classification of data gaps in a DEM can enable one to select the appropriate method to interpolate such as using a thin plate spline method (Olsen et al. 2015) to fill occlusions and a hydro-flattening type (Deshpande and Yilmaz 2017) technique to fill water-derived dropouts. Our processing methods for TLS-derived DEMs, both in terms of occlusions and data dropouts, greatly improves the utility of these products for end users.

2.6 ACKNOWLEDGEMENTS

used in this study. Keith Williams (OSU), Abby Chin (OSU), and Shawn Butcher (OSU) assisted

with the acquisition and processing of the TLS data for the Rabbit Rock Site.

2.7 REFERENCES

Barnea, S., and Filin, S. (2007). "Registration of terrestrial laser scans via image based features." International Archives of Photogrammetry, Remote Sensing and Spatial Information Sciences 36 (Part 3), 32–37.

Che, E., and Olsen, M. J. (2017). "Fast ground filtering for TLS data via Scanline Density Analysis." ISPRS Journal of Photogrammetry and Remote Sensing, 129, 226–240.

Deshpande, S. S., and Yilmaz, A. (2017). "A semi-automated method to create a lidar-based hydro-flattened DEM." International Journal of Remote Sensing, 38(5), 1365–1387.

Dillencourt, M. B., Samet, H., and Tamminen, M. (1992). "A General Approach to Connected-component Labeling for Arbitrary Image Representations." J. ACM, 39(2), 253–280.

Fisher, R., Perkins, S., Walker, A., and Wolfart, E. (2017). "Connected Components Labeling." Image Processing Learning Resources, <http://homepages.inf.ed.ac.uk/rbf/HIPR2/label.htm>.

Höfle, B., Griesbaum, L., and Forbriger, M. (2013). "GIS-Based Detection of Gullies in Terrestrial LiDAR Data of the Cerro Llamoca Peatland (Peru)." Remote Sensing, 5(11), 5851–5870.

Höfle, B., Vetter, M., Pfeifer, N., Mandlburger, G., and Stötter, J. (2009). "Water surface mapping from airborne laser scanning using signal intensity and elevation data." Earth Surface Processes and Landforms, 34(12), 1635–1649.

Hollenbeck, J. P., Olsen, M. J., and Haig, S. M. (2014). "Using terrestrial laser scanning to support ecological research in the rocky intertidal zone." Journal of Coastal Conservation, 18(6), 701–714.

Huber, D. (2011). "The ASTM E57 File Format for 3D Imaging Data Exchange." Proceedings of the SPIE Vol. 7864A, Electronics Imaging Science and Technology Conference (IS&T), 3D Imaging Metrology, Pittsburgh, PA.

Leica Cyclone 8.0 Help. (2014). Leica Geosystems.

"LiDAR Glossary | AGRG." (2017). <http://agrg.cogs.nscc.ca/resources/lidar-glossary/> (Jun. 11, 2017).

Mahmoudabadi, H., Olsen, M. J., and Todorovic, S. (2016). "Efficient terrestrial laser scan segmentation exploiting data structure." ISPRS Journal of Photogrammetry and Remote Sensing, 119, 135–150.

Olsen, M. (2011). "Bin 'N' Grid: A simple program for statistical filtering of point cloud data." LIDAR Magazine. <http://www.lidarmag.com/content/view/8378/199/>.

Olsen, M. J., Ponto, K., Kimball, J., Seracini, M., and Kuester, F. (2010). "2D open-source editing techniques for 3D laser scans." Proceedings of the 38th Annual Conference on Computer Applications and Quantitative Methods in Archaeology, CAA, 47-50.

Olsen, M., Johnstone, E., Kuester, F., Driscoll, N., and Ashford, S. A. (2011). "New Automated Point-Cloud Alignment for Ground-Based Light Detection and Ranging Data of Long Coastal Sections." Journal of Surveying Engineering, 137(1), 14–25.

Olsen, M., Wartman, J., McAlister, M., Mahmoudabadi, H., O'Banion, M., Dunham, L., and Cunningham, K. (2015). "To Fill or Not to Fill: Sensitivity Analysis of the Influence of Resolution and Hole Filling on Point Cloud Surface Modeling and Individual Rockfall Event Detection." Remote Sensing, 7(9), 12103–12134.

Smeeckaert, J., Mallet, C., David, N., Chehata, N., and Ferraz, A. (2013). "Large-scale classification of water areas using airborne topographic lidar data." Remote Sensing of Environment, 138, 134–148.

Telling, J., Lyda, A., Hartzell, P., and Glennie, C. (2017). "Review of Earth science research using terrestrial laser scanning." Earth-Science Reviews, 169, 35–68.

Vosselman, G., and Maas, H.-G. (2010). Airborne and Terrestrial Laser Scanning. Whittles Publishing, Scotland, UK.

Wei, L.-X., Yang, B., Jiang, J.-P., and Cao, G.-Z. (2016). "Adaptive algorithm for classifying LiDAR data into water and land points by multifeature statistics." Journal of Applied Remote Sensing, 10(4), 045020–045020.

Manuscript # 2

Efficient Planning and Acquisition of Terrestrial Laser Scanning-derived Digital Elevation Models – A Proof of Concept Study

Matthew S. O'Banion and Michael J. Olsen

3 EFFICIENT PLANNING AND ACQUISITION OF TERRESTRIAL LASER SCANNING-DERIVED DIGITAL ELEVATION MODELS – A PROOF OF CONCEPT STUDY

3.1 ABSTRACT

Development of a digital elevation model (DEM) with terrestrial laser scanning (TLS) point cloud data of inadequate resolution and/or completeness will result in a poor-quality DEM with significant gaps. In many cases, this fact can be obscured from the user because a triangular irregular network (TIN) is often created prior to DEM creation, resulting in a seamless DEM where data gaps in the source TLS data have been interpolated across by the TIN. However, evaluating completeness of DEMs created directly from the point cloud data provides more feedback regarding the suitability of a given TLS point cloud for supporting a specified DEM resolution. An empirical DEM completeness database and associated TLS acquisition planning tool is proposed that can assist in optimizing TLS survey parameters (quantity of scans, and scanning resolution) for achieving a high-quality DEM of specified resolution and completeness.

3.2 INTRODUCTION

Planning a terrestrial laser scanning (TLS) acquisition campaign for the purpose of generating a digital elevation model (DEM) of specified resolution can be a challenging task. Striking a balance between collecting enough information to capture the topography while avoiding excess redundant data can be a sensitive process (Olsen et al. 2009), which commonly requires the TLS surveyor, at a minimum, to appropriately estimate the quantity of scan positions and the required scanning resolution (Fan and Atkinson 2015). Oftentimes, overly conservative planning and

execution of field work (e.g., Zhang et al. 2016) is needed to ensure a DEM can be created that meets the specified requirements. For instance, Pietro et al. (2008); Carrivick et al. (2015) both state that higher resolution DEMs could have been created with the acquired TLS data; however, lower resolution models were favored due to their higher manageability. This approach tends to result in cost overages due to the increased time associated with additional scans and/or scanning at unnecessarily high resolutions. An unnecessary increase in data quantity/density also increases the amount of processing time required in the office. Conversely, an insufficient number of scans can result in significant occlusions. This problem is compounded for environments where ground filtering of points is required prior to generating a DEM (e.g., Meng et al. 2010), which can further reduce the completeness of the TLS dataset as well as degrade the resolution.

Attempting to generate a DEM with TLS point cloud data of inadequate resolution and/or completeness will result in a poor-quality DEM with many data gaps. Data gaps within DEMs usually require interpolation, extrapolation, and/or a specialized surface patching technique (e.g., Olsen et al. 2015) to fill the gaps and create a continuous model. Filled-in DEM data gaps indirectly rely on actual measurements and the quantity and magnitude of these regions should be minimized for a high-quality DEM.

In support of assisting TLS surveyors balance the various parameters needed to efficiently survey an area while minimizing the amount of data gap filling required in subsequent DEMs, a TLS acquisition planning tool is presented herein that relies on an empirical DEM completeness database. Based on user provided inputs, the TLS planning tool provides recommendations for the total number of scan positions, scanning resolution, and estimated survey time. The

recommendations represent a lower limit and are meant to provide a starting point for TLS acquisition planning.

3.3 BACKGROUND

Many of the studies that evaluate quality of laser scanning-derived DEMs focus on geometric accuracy (e.g., Meneses et al. 2005; Bater and Coops 2009; Heritage et al. 2009; Bolkas et al. 2016); Nevertheless, an important quality metric for laser scanning data and therefore derived DEMs is completeness (Olsen et al. 2013). While in some applications, gaps in the DEM may be acceptable, in many applications such as hydrological modeling, a continuous and complete DEM is required. To ensure a complete DEM can be generated, it is common to create a triangular irregular network (TIN) from the point data prior to developing the grid-based DEM (Fan and Atkinson 2015). A potential problem with this method is that poor-quality point cloud data with many data gaps will still result in a continuous DEM due to the inherent interpolation performed by the TIN algorithm. Unfortunately, the user is often unaware of which cells contain sufficient data and which cells contain interpolated values. In contrast, creating a DEM directly from the ground filtered point cloud data through binning provides a better opportunity to evaluate if the TLS dataset is capable of accurately supporting the chosen DEM resolution. Also, DEM completeness represents a quality metric that can be determined without the need for an external reference (e.g., ground control points) as required in empirically-based accuracy assessments. Furthermore, completeness is related to geometric accuracy in the sense that the largest errors in a DEM will likely be located where interpolation or surface patching is heavily relied upon due to the lack of adequate point density.

Whether the resolution of a point cloud is adequate for creation of a high-quality DEM, depends on the required resolution for the DEM and how close the TLS scans were performed to the area of interest (AOI). Because TLS data is acquired at fixed angles of rotation from a fixed location, point density/spacing can be quite heterogeneous, with point density decreasing with increased distance from the scanner (Vosselman and Maas 2010). This variability can result in only part of the TLS dataset being adequate for the chosen DEM resolution. The completeness of TLS point cloud data is impacted by two types of significant data gaps: occlusions and dropouts (Chapter 2). Occlusions occur from objects blocking the view of the scanner; whereas, dropouts occur from wet or reflective surfaces that do not result in a laser return. In most cases, occlusions in the TLS data can be mitigated by additional scan positions from well-chosen points of view (Telling et al. 2017); however, dropouts can be more difficult to mitigate during TLS acquisition and should not be considered when evaluating TLS survey or DEM quality unless they could be avoided (e.g., scanning at a different time).

From the literature, we know that TLS scanner placement has a significant effect on point cloud quality (e.g., Buckley et al. 2008; Heritage et al. 2009; Olsen et al. 2009). When it comes to survey planning for airborne laser scanning (ALS), detailed methodologies for choosing appropriate parameters such as flying height, sampling rate, and swath overlap exist to ensure collection of systematic, high-quality data (ASPRS 2013). However, relative to ALS, the support for planning TLS-based topographic surveys has lagged behind (Starek et al. 2010). This is likely due to the heterogeneous nature of TLS surveys stemming from the variable point density of the data and the highly variable characteristics associated with terrestrially scanned environments. When *a priori* topographic information is available, scan placement optimization can be

performed using spatial statistics and/or viewshed analyses (e.g., Starek et al. 2010; Carrivick et al. 2015); however, when existing topographical data of comparable resolution to that generated with TLS does not exist, these methods cannot be properly utilized. The *TopoPlanner* software (Certainty 3D 2017) provides assistance in planning a TLS survey campaign; however, focus is placed on adjacent scan overlap (approximated by 2D circles) and neglects to consider scanning resolution or the occurrence of data gaps from obstructions.

In addition to data gaps passed on to the DEM from occlusions and dropouts in the TLS data, additional data gaps can form in the DEM based on the chosen DEM resolution or by requiring a threshold of a minimum number of points within each DEM cell used to calculate the elevation. Choosing a DEM resolution that is too fine results in data gaps when the DEM cells sample space that lies in-between the point cloud points. Alternatively, choosing too coarse of a resolution will result in a DEM free of data gaps; however, geometric detail will be lost due to the smoothing effect of the relatively large cell size utilized. As for the minimum points/DEM cell parameter, when working with bare-earth ground filters, it is common to analyze a collection of points for a given DEM cell to determine which elevation most likely represents the ground surface in that cell followed by a comparison of neighboring cells. Stipulating a high number (e.g., 10 points) is very useful when creating a bare-earth DEM from point cloud data of a vegetated area; however, it requires a higher point density to ensure adequate sampling in each cell to distinguish vegetation. Requiring only 1 point/DEM cell will be more successful in avoiding data gaps in low point density situations but less information is available for determining the elevation. Lower values for minimum points/DEM cell are often used in

environments where the ground/terrain surface is clear and unobstructed, and higher values are used when the terrain is obscured by vegetation.

3.4   DEM COMPLETENESS DATABASE

Using the automated data gap classification methodology presented in Chapter 2, the completeness of a given DEM can be accurately quantified while ignoring any dropout data gaps. Dropouts are omitted from the proposed DEM completeness evaluation because they are not caused by the chosen quantity of scans and scanning resolution, nor by the selection of DEM creation parameters. Dropouts are ordinarily beyond the control of the surveyor. By analyzing completeness of numerous DEMs with varying input data and DEM creation parameters, the relationship between these values and the quality of the resulting DEM can be better understood and the results can be used to aid in TLS acquisition planning for future projects.

3.4.1   Study Site

The empirical DEM completeness database and subsequent TLS planning tool were developed from TLS data acquired with a Riegl VZ-400 TLS instrument at a controlled site cordoned off in an open grassy field. Nevertheless, the tool is valid for similar terrestrial scanners. The study site measured approximately 14 m x 20 m in size and contained six cardboard boxes and six shallow receptacles filled with water. The boxes served as both a surface to mount black & white survey targets and as basic, occlusion causing, objects. The water receptacles were used to generate dropout data gaps for another research project (Chapter 2). These data gaps were classified and omitted from the DEM completeness evaluation. For the purpose of this study, eight independent scans of the ~ 300 m^2 AOI were acquired at four different angular resolutions (0.02, 0.04, 0.06,

and 0.08°). The eight scans were used to create five different scanning scenarios as depicted in Figure 3-1.
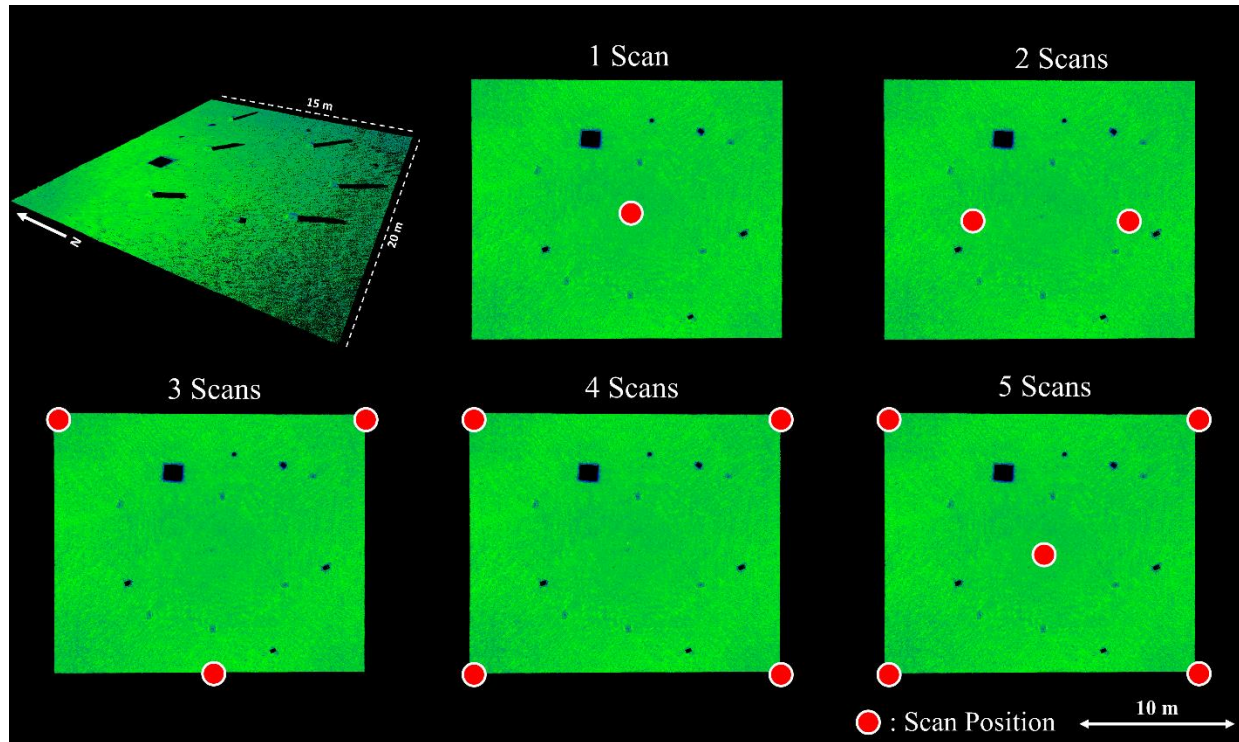
Figure 3-1: 3D overview of study site along with the five different scanning scenarios in which different quantities of TLS scans were used. The red dots indicate locations where the scanner was setup.

A preliminary registration (initial alignment) of the eight scan positions was completed using the survey targets located on the faces of the cardboard boxes. A final, cloud-to-cloud-based registration was performed using the PointReg v.3 software (Olsen et al. 2011).

3.4.2   DEM Creation and Analysis

The registered TLS point cloud data was used to generate 560 individual DEMs that represent unique permutations through varying the following four parameters: Quantity of Scans, Scanning

Resolution, DEM Resolution, and Minimum Points/DEM cell. Values used for each of these parameters are presented in Table 3.1.

Table 3.1: Values used for the TLS acquisition and DEM creation parameters.

Parameter	Values
Qty. of Scans	1, 2, 3, 4, 5
Scanning Resolution (°)	0.02, 0.04, 0.06, 0.08
DEM Resolution (m)	0.01, 0.02, 0.04, 0.10, 0.25, 0.50, 1.00
Min. Pts/DEM cell	1, 2, 5, 10

The collection of DEMs were efficiently generated using batch scripting and the DEM creation software, BinNGrid (Olsen 2011). Elevations were computed for each DEM cell using the median elevation from the relevant TLS points in each cell. All DEMs were then automatically evaluated for the overall percentage of occlusion data gaps (inverse of completeness) using the data gap classification methodology presented in Chapter 2. This data gap classification methodology identifies data gaps in a TLS-derived DEM and subsequently classifies them as either occlusions or dropouts. To differentiate between the two types, dropout boundary flags developed using projected 2D representations of the point cloud data are used. It should be noted that data gaps stemming from the selection of DEM resolution, and points/DEM cell are considered as occlusion data gaps by the utilized methodology. Logarithmic plots of the results of this analysis are presented in Figure 3-2.
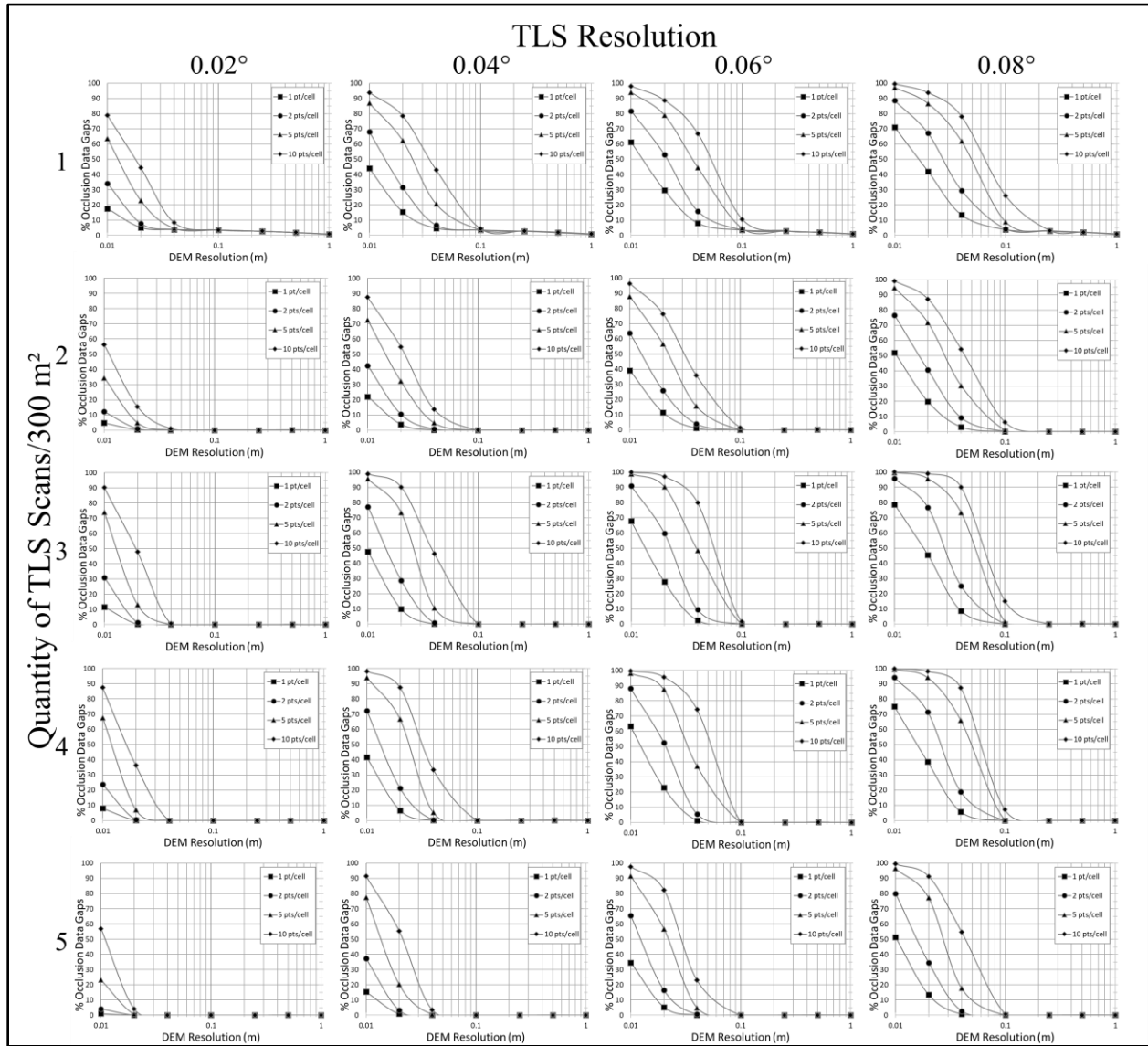
Figure 3-2: Plots representing the DEM completeness evaluation results for 560 unique DEMs based on the quantity of scans, scan resolution, desired DEM resolution, and minimum number of points required in each cell.

Not surprisingly, the highest frequency of DEM data gaps is observed when performing a low number of scans at a coarse scanning resolution (0.08°). Alternatively, a very complete (> 90%), high-resolution (2 cm) DEM requiring 10 points/DEM cell is possible; however, it requires 5

scans/300 m^2 at a scanning resolution of 0.02°. In between these extremes, there are many details that can aid in better planning TLS acquisition to achieve the desired results efficiently.

3.5   TLS ACQUISITION PLANNING TOOL

The DEM completeness results presented in Figure 3-2 were used to develop a software application that can aid in the planning of a TLS acquisition campaign for the development of a DEM. This proof of concept planning tool was developed in Matlab and, at this time, relies solely on the empirical results generated for the study site. The Matlab code for this tool is included in Appendix A. In addition to the DEM completeness results, survey time estimates were introduced into the program based on the time taken when using a Riegl VZ-400 at the selected scanning resolutions. The assigned times for 0.02°, 0.04°, 0.06°, and 0.08° resolution scans are 15 min, 10 min, 7 min, and 6 min, respectively. These time estimates include time to set up and take down the TLS instrument between scan positions and are simply multiplied by the recommended number of scans to determine the total survey time. These times could be adjusted to represent other scanners as well as other factors, such as, if images are co-acquired with the scan data.

Based on user provided inputs for the size of the AOI (m^2), the desired DEM resolution (DEM$_{Res}$), the minimum number of points/DEM cell used to calculate an elevation (DEM$_{Pts}$), and the desired completeness (DEM$_{Comp}$), the planning tool recommends the total number of scans, scanning resolution and provides an estimated time for the survey. The recommended quantity of scans is meant to be a starting point (minimum number of scans). Increases in terrain complexity

and/or quantity of occlusion causing objects, and any limitations with regard to scanner placement or view will cause the quantity of required scans to increase.

The logic used to make these recommendations is presented in the flow chart in Figure 3-3. It is important to note that although the DEM completeness database includes results for a single scan scenario, the planning tool will always recommend a minimum of two scans so that the large data gaps that are present beneath TLS instruments have a chance of being filled in by the second position. Also, when searching for the scenario that results in the least amount of time, if more than one option has the same low time, the scenario that results in the highest quantity of scans will be selected. Favoring more scan positions increases the chances of filling in occlusions and results in a more uniform distribution of point density.
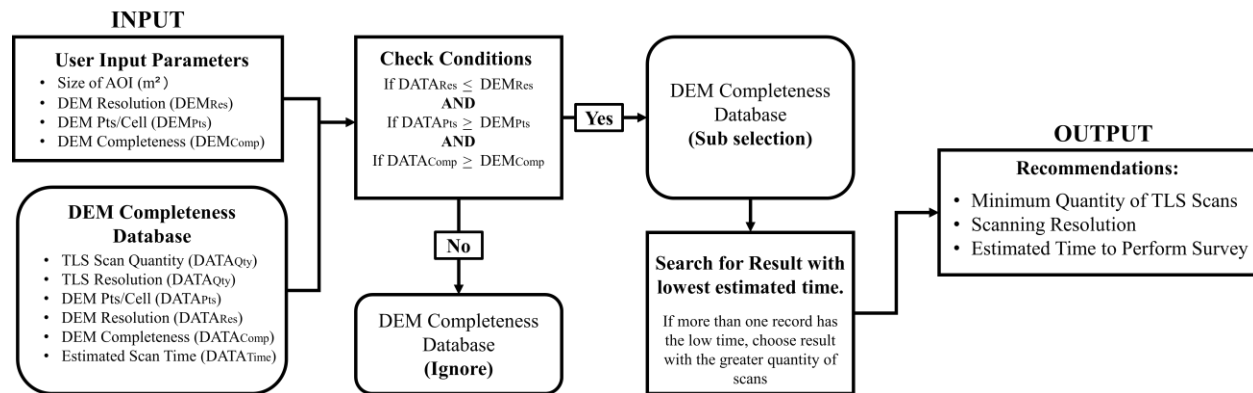
Figure 3-3: Flow chart of TLS planning tool logic.

For demonstration purposes, a collection of example inputs and results from the TLS acquisition planning tool are included in Figure 3-4. For each of the four categories (Figure 3-4a, 3-4b, 3-4c, and 3-4d) 4 scenarios were run through the tool where a single input parameter (outlined by dotted line) was varied while the others remained constant.

a) **Varied AOI Size**

Input				
AOI Size (m²):	500	1000	1500	2000
DEM_{Res} (m):	0.04	0.04	0.04	0.04
DEM_{Pts} :	1	1	1	1
DEM_{Comp} (%):	90	90	90	90
Output				
Quantity of Scans:	2	4	5	7
Scanning Resolution (°):	0.06	0.06	0.06	0.06
Estimated Time (Min.):	14	28	35	49

b) **Varied DEM Resolution**

Input				
AOI Size (m²):	500	500	500	500
DEM_{Res} (m):	0.25	0.10	0.04	0.02
DEM_{Pts} :	1	1	1	1
DEM_{Comp} (%):	90	90	90	90
Output				
Quantity of Scans:	2	2	2	2
Scanning Resolution (°):	0.08	0.08	0.06	0.02
Estimated Time (Min.):	12	12	14	30

c) **Varied DEM Points/Cell**

Input				
AOI Size (m²):	500	500	500	500
DEM_{Res} (m):	0.04	0.04	0.04	0.04
DEM_{Pts} :	1	2	5	10
DEM_{Comp} (%):	90	90	90	90
Output				
Quantity of Scans:	2	2	2	2
Scanning Resolution (°):	0.06	0.06	0.06	0.02
Estimated Time (Min.)	14	14	14	30

d) **Varied DEM Completeness**

Input				
AOI Size (m²):	500	500	500	500
DEM_{Res} (m):	0.04	0.04	0.04	0.04
DEM_{Pts} :	1	1	1	1
DEM_{Comp} (%):	70	80	90	99
Output				
Quantity of Scans:	2	2	2	4
Scanning Resolution (°):	0.08	0.08	0.06	0.04
Estimated Time (Min.)	12	12	14	40

Figure 3-4: Demonstration of TLS planning tool recommendations (Outputs) for 16 different scenarios. For the four categories of scenarios, the following parameters are varied while the others remain constant: a) AOI size, b) required DEM resolution, c) minimum points/DEM cell, and d) required DEM completeness (%).

When varying the AOI size (Figure 3-4a) from 500 to 2000 m² by increments of 500 m², there is a steady increase in the quantity of scans and therefore the estimated survey time. The recommended scanning resolution remains constant at 0.06° due to the unchanging required DEM resolution. Based on the results for varied DEM resolutions (Figure 3-4b), a 0.10 m DEM can be achieved with the same TLS survey parameters required for a lower resolution, 0.25 m DEM. When increasing the resolution to 0.04 m, a small increase in scanning resolution is recommended. A more significant jump in required resolution and estimated time is reported

when tasked with a 0.02 m DEM. Increasing the required DEM points/cell parameter (Figure 3-4c) has little effect on the recommend survey parameters until 10 pts/cell is required; at which time, the recommended scanning resolution and estimated time increases from 0.06° to 0.02°, and 14 to 30 minutes, respectively. Lastly, we consider the required DEM completeness values input from 70 to 99% (Figure 3-4d). No differences are reported when increasing from a 70 to 80% completion requirement. A small increase in scanning resolution is recommended to achieve 90% and an increase in both quantity of scans (2 to 4) and scanning resolution (0.06 to 0.04°) is recommended to achieve 99% completion for a 0.04 m DEM of a 500 m^2 AOI and requiring only 1 point/DEM cell.

3.6 CONCLUSION

The proposed TLS acquisition planning tool utilizes an empirical DEM completeness database to aid in estimating the minimum required quantity of scans and scanning resolution required to achieve a DEM of specified resolution and completeness. This tool represents a proof of concept and is currently limited by the contents of the DEM completeness database, which was developed for a simple site. More complex scenes will require additional scans than the minimum value reported by the tool.

The fundamental purpose of the proposed DEM completeness database and TLS planning tool is to enable a TLS surveyor to balance the various factors that control TLS-derived DEM completeness in favor of surveying efficiency while still meeting the desired quality specifications. This solution provides an opportunity to share practical knowledge and

experience amongst the community of TLS surveyors that is usually held solely by those with expert knowledge and extensive experience.

Future work will incorporate additional empirical data into the database that is representative of a variety of site conditions. In addition, a future version of the TLS planning tool may include qualitative, site specific, parameters for terrain complexity and obstacle quantity. The addition of these qualitative parameters along with a more comprehensive database will assist the planning tool in making better recommendations for a given site. Lastly, in situations where repeat surveys are necessary and therefore existing topography would be available, the proposed planning tool could be combined with an advanced scan placement optimization methodology such as that proposed in Starek et al. (2010).

3.7 REFERENCES

ASPRS. (2013). Manual of Airborne Topographic Lidar. American Society for Photogrammetry and Remote Sensing, Bethesda, MD.

Bater, C. W., and Coops, N. C. (2009). "Evaluating error associated with lidar-derived DEM interpolation." Computers & Geosciences, 35(2), 289–300.

Bolkas, D., Fotopoulos, G., Braun, A., and Tziavos, I. N. (2016). "Assessing Digital Elevation Model Uncertainty Using GPS Survey Data." Journal of Surveying Engineering, 142(3), 04016001.

Buckley, S. J., Howell, J. A., Enge, H. D., and Kurz, T. H. (2008). "Terrestrial laser scanning in geology: data acquisition, processing and accuracy considerations." Journal of the Geological Society, 165(3), 625–638.

Carrivick, J. L., Smith, M. W., and Carrivick, D. M. (2015). "Terrestrial laser scanning to deliver high-resolution topography of the upper Tarfala valley, arctic Sweden." GFF, 137(4), 383–396.

Certainty 3D. (2017). TopoPlanner. < http://certainty3d.com/products/topoplanner/>

Fan, L., and Atkinson, P. M. (2015). "Accuracy of Digital Elevation Models Derived From Terrestrial Laser Scanning Data." IEEE Geoscience and Remote Sensing Letters, 12(9), 1923–1927.

Heritage, G. L., Milan, D. J., Large, A. R. G., and Fuller, I. C. (2009). "Influence of survey strategy and interpolation model on DEM quality." Geomorphology, 112(3), 334–344.

Meneses, A. S., Chasco, F. R., García, B., Cabrejas, J., and González-Audícana, M. (2005). "Quality Control in Digital Terrain Models." Journal of Surveying Engineering, 131(4), 118–124.

Meng, X., Currit, N., and Zhao, K. (2010). "Ground Filtering Algorithms for Airborne LiDAR Data: A Review of Critical Issues." Remote Sensing, 2(3), 833–860.

Olsen, M. (2011). "Bin 'N' Grid: A simple program for statistical filtering of point cloud data." LIDAR Magazine.

Olsen, M. J., Johnstone, E., Driscoll, N., Ashford, S. A., and Kuester, F. (2009). "Terrestrial Laser Scanning of Extended Cliff Sections in Dynamic Environments: Parameter Analysis." Journal of Surveying Engineering, 135(4), 161–169.

Olsen, M. J., Roe, G. V., Glennie, C., Persi, F., Reedy, M., Hurwitz, D., Williams, K., Tuss, H., Squellati, A., and Knodler, M. (2013). Guidelines for the Use of Mobile LIDAR in Transportation Applications. NCHRP, Transportation Research Board (TRB).

Olsen, M., Johnstone, E., Kuester, F., Driscoll, N., and Ashford, S. A. (2011). "New Automated Point-Cloud Alignment for Ground-Based Light Detection and Ranging Data of Long Coastal Sections." Journal of Surveying Engineering, 137(1), 14–25.

Olsen, M., Wartman, J., McAlister, M., Mahmoudabadi, H., O'Banion, M., Dunham, L., and Cunningham, K. (2015). "To Fill or Not to Fill: Sensitivity Analysis of the Influence of Resolution and Hole Filling on Point Cloud Surface Modeling and Individual Rockfall Event Detection." Remote Sensing, 7(9), 12103–12134.

Pietro, L. S., O'Neal, M. A., and Puleo, J. A. (2008). "Developing Terrestrial-LIDAR-Based Digital Elevation Models for Monitoring Beach Nourishment Performance." Journal of Coastal Research, 246, 1555–1564.

Starek, M., J., Mitasova, H., and Harmon, R., S. (2010). "Optimization of Terrestrial Laser Scanning Survey Design for Dynamic Terrain Monitoring." Poster, AGU 2010, San Francisco, CA.

Telling, J., Lyda, A., Hartzell, P., and Glennie, C. (2017). "Review of Earth science research using terrestrial laser scanning." Earth-Science Reviews, 169, 35–68.

Vosselman, G., and Maas, H.-G. (2010). Airborne and Terrestrial Laser Scanning. Whittles Publishing, Scotland, UK.

Zhang, C., Kalasapudi, V. S., and Tang, P. (2016). "Rapid data quality oriented laser scan planning for dynamic construction environments." Advanced Engineering Informatics, 30(2), 218–232.

Manuscript # 3

Suitability of Structure from Motion for Rock-Slope Assessment

Matthew S. O'Banion, Michael J. Olsen, Claire Rault, Joseph Wartman, and Keith Cunningham

4 SUITABILITY OF STRUCTURE FROM MOTION FOR ROCK-SLOPE ASSESSMENT

4.1 ABSTRACT

Terrestrial laser scanning (TLS) has been widely and effectively used to assess and monitor unstable slopes; however, limited visibility of a slope or cliff from accessible scan locations can result in significant data occlusions. Employing unmanned aircraft systems (UAS) in concert with a handheld camera to gather overlapping digital imagery can generate similar 3D point cloud reconstructions by way of Structure-from-Motion (SfM) and multi-view stereo (MVS) photogrammetric techniques. Acquisition of geometry using UAS can provide superior accessibility for portions of a slope not visible from locations on the ground accessible to TLS. This study examines three sites in Alaska with unstable rock-slopes that were both surveyed using TLS and SfM techniques. The datasets were acquired simultaneously and linked to a rigorous survey control network. An accuracy evaluation of the SfM-derived surface models was performed using TLS data and numerous reflectorless total station observations collected across the rock-slopes. A quality evaluation was conducted to examine differences in point density, model completeness, and distributions of morphological properties between the SfM and TLS datasets. The results indicate that SfM is a viable option for unstable rock-slope assessment when a sufficient quantity of images with adequate overlap are acquired, and the reconstruction is tied to a survey control network. The best results in terms of accuracy and completeness were achieved when combining both UAS-based aerial imagery and terrestrial imagery for the SfM reconstruction. However, artifacts observed in the SfM data, such as over-smoothing and

geometric inconsistencies bring into question the suitability of SfM for detection of small changes over time.

4.2 INTRODUCTION

Terrestrial laser scanning (TLS), also known as terrestrial or ground-based lidar, has proven to be a valuable, reliable technique for the assessment and monitoring of unstable slopes; however, even with numerous setups, portions of a slope or cliff may not be visible from areas accessible to the scanner, resulting in the inability to capture important features of the slope morphology. In lieu of TLS, unmanned aircraft systems (UAS) and a handheld camera may gather overlapping digital imagery to generate similar three-dimensional (3D) point clouds by way of Structure-from-Motion (SfM) and multi-view stereo (MVS) photogrammetric techniques (hereafter collectively referred to as SfM). Use of UAS can provide superior accessibility to cliffs and the acquisition of cliff geometry compared to TLS methods.

This study examines three unstable road cuts along the Glenn Highway in Alaska, U.S.A. with different morphologies to evaluate the suitability of SfM for rock-slope assessment. SfM suitability is judged relative to TLS methods with regards to absolute accuracy (i.e., including geo-referencing error) and quality of the 3D data. While previous studies have attempted to assess the accuracy of SfM-based image reconstructions (e.g., Harwin and Lucieer, 2012; James and Robson, 2012; Eltner et al., 2016; Westoby et al., 2012; Fonstad et al., 2013; Lato et al., 2015b; James et al., 2017a; James et al., 2017b), they commonly use a single, independent reference consisting of airborne or terrestrial lidar. In many of these cases, no accuracy assessment of the lidar-based reference is performed or documented. This study presents an

accuracy assessment that is both rigorous and comprehensive. Two independent references are used for the accuracy assessment: co-acquired TLS data and a collection of reflectorless total station (TS) points collected across the surface of the rock-slopes. The rock-slope TS points serve to evaluate the accuracy of the TLS data, ensuring it is appropriate for judging the accuracy of the SfM data. The rock-slope TS points also serve as a second reference for judging the accuracy of the SfM data. Occasionally, studies will report accuracies of SfM models that simply represent geo-referencing residuals from surveyed ground control points (GCPs) or based on discrepancies with surveyed checkpoints. When surveyed checkpoints are visible in the imagery as high contrast targets (e.g., Harwin and Lucieer, 2012; Fassi et al., 2013), the accuracy assessment can be overly optimistic. The performance of a SfM algorithm when automatically identifying key features in overlapping imagery is directly correlated to the presence of high contrast, textural differences in photographs. Employing highly visible, high contrast GCPs, therefore, results in evaluating accuracy at locations where SfM is theoretically performing at its best (Javadnejad and Gillins, 2016). The independent references used for this study were chosen to evaluate the accuracy throughout the majority of the SfM reconstruction.

This paper presents an evaluation of the suitability of SfM for rock-slope assessment. Accuracy is analyzed through a comparison with two high-accuracy, high precision independent references, tied to a rigorous survey control network. In addition, a quality assessment of SfM data relative to TLS examines important factors such as point density, surface model completeness, and surface morphology. These additional quality metrics have not been thoroughly or formally evaluated in prior work, which has focused primarily on geometric accuracy. In the context of the accuracy and quality evaluations, comparisons were performed

between ground and UAS-based SfM models, as well as, combination SfM (Combo SfM) models in which both ground and UAS-imagery was utilized.

4.3 BACKGROUND

Road cuts through rocky terrain often result in steep rock-slopes, which can be susceptible to rockfall – a process involving detachment, fall, rolling, and bouncing of rocks (Hungr et al., 2014). Rockfall is a reoccurring hazard along transportation corridors in mountainous regions throughout North America. Tens of millions of dollars ($US) are spent annually on rock-slope maintenance and mitigation (Turner and Jayaprakash, 2013).

Current methods for characterization of rockfall hazards and risk rely on rock mass classification (e.g., Pantelidis, 2009) or rockfall hazard rating systems (e.g., Pierson, 2013) that depend on manual visual inspection and simplified calculations. These methods are both qualitative in nature (Budetta and Nappi, 2013) and coarse in spatial resolution. TLS allows for systematic acquisition of rock-slope 3D geometry at high, cm-scale spatial resolutions (Jaboyedoff et al., 2012; Abellán et al., 2014). TLS has been proven as an appropriate method for rock-slope characterization (Jaboyedoff et al., 2012; Abellán et al., 2009; Abellán et al., 2010; Abellán et al., 2014; Alba et al., 2009; Alba and Scaioni, 2010; Kemeny and Turner, 2008; Rabatel et al., 2008; Girardeau-Montaut, 2017; Kromer et al., 2015; Gigli and Casagli, 2011), and monitoring (Lim et al., 2005; Lim et al., 2010; Rosser et al., 2005; Rosser et al., 2007; Lato et al., 2009; Olsen et al., 2009; Olsen, 2013).

TLS offers advantages in terms of accuracy, repeatability, and reliability; however, challenges exist such as cost and the common occurrence of occlusions. SfM-based image reconstruction

has the potential to solve these challenges (Fonstad et al., 2013; Chandler and Buckley, 2016). Acquisition of imagery for SfM reconstruction using a UAS offers further advantages in terms of terrain accessibility (e.g., Lato et al., 2015b). UAS imagery acquisition and subsequent SfM model reconstruction have proven useful for landslide analysis and digital rock outcrop acquisition. Researchers have utilized repeat surveys from UAS platforms to quantify landslide displacements of large, slow-moving landslides (Niethammer et al., 2012; Fernández et al., 2015; Fernández et al., 2016; Lucieer et al., 2014; Turner et al., 2015). Others have utilized the imagery for mapping landslide features such as scarps and deposits for small areas (e.g., Al-Rawabdeh et al., 2016). For example, Murphy et al. (2016) utilized UAS to map damages from the 2014 Oso landslide in Washington, and Greenwood et al. (2016) utilized UAS to map rock masses and slides in Nepal after the 2015 earthquake event. Lastly, Manousakis et al. (2016) utilized UAS SfM for rockfall hazard analysis. SfM-based digital outcrop acquisition has been successfully performed by various studies (e.g., James and Robson, 2012; Bemis et al., 2014; Lato et al., 2015a; Wilkinson et al., 2016). However, results of a comparison with co-acquired TLS data from Wilkinson et al. (2016) indicates that the precision of SfM data can deteriorate near the outcrop edges and over-smoothing rounds off sharp rock edges within the outcrop. It is also worth noting that Wilkinson et al. (2016) states that an "elaborate" data acquisition and processing approach is often required to achieve results similar to TLS.

Eltner et al. (2016) present an extensive review of SfM accuracies reported by 39 different published geoscientific studies. The following factors introduce error into SfM-based 3D reconstructions: the scale of the object/environment being captured, the distance of the camera from the imaged object(s), camera calibration, image network geometry, image-matching

performance, surface texture and lighting conditions, and GCP characteristics (Eltner et al., 2016). In terms of accuracy of SfM, Eltner et al. (2016) report no significant issues that cannot be mitigated by placement of GCPs, camera calibration or a high number of images. This is true with the exception to having a lack of textural detail in the imaged scene. Homogeneous surface texture commonly prevents automated feature matching algorithms from resolving coincident points and generating accurate 3D geometry (Bemis et al., 2014). Nevertheless, many aspects of image acquisition, GCP network design, and subsequent SfM processing vary substantially study to study. These ad-hoc approaches result in difficulties when attempting to systematically compare accuracies reported by numerous studies (Eltner et al., 2016; James et al., 2017a), and when reporting accuracies of a given SfM collection based on previously achieved accuracies. These disparities are partly due to unknowns with regards to performance and uncertainty associated with image feature matching utilized by SfM algorithms (Eltner et al., 2016), some of which are proprietary (e.g., Agisoft PhotoScan). It is for this reason that the use of a trusted independent reference such as TLS is needed to appropriately judge the accuracy of SfM under the unique conditions and methods followed for a given study.

4.4 STUDY AREA

The study area is located approximately 110 km northeast of Anchorage, Alaska, U.S.A. along the Glenn Highway (Hwy. A-1) (Figure 4-1). The region is primarily comprised of sedimentary rocks of the Matanuska and Chickaloon Formations. The Matanuska Formation is a marine sedimentary deposit formed during the orogenic rise of the Talkeetna Mountains. The Chickaloon Formation was deposited as propagating alluvial fans on top of the Matanuska Formation that formed as the Talkeetna Mountains were uplifted and sequentially eroded

(Belowich, 2006). The highway follows the glacial cut into the Chickaloon Formation; however, no other glacial evidence may be found in the area (Trop et al., 2015). Regions of the Matanuska Formation exposed in road cuts along the Glenn Highway largely consist of dark mudstones while Chickaloon Formation outcrops mainly consist of carbonaceous siltstone, coal, and sandstone (Trop et al., 2015).
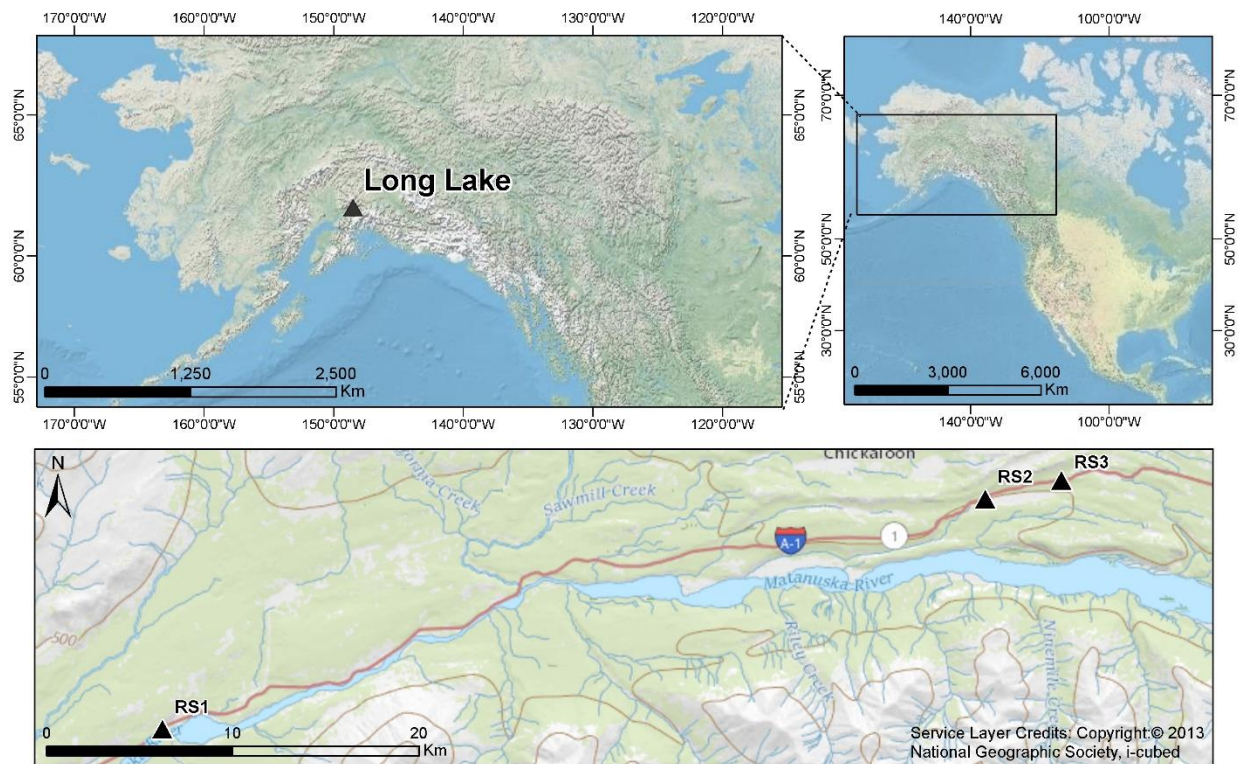
Figure 4-1: Study area location plan. Three independent sites were selected: RS1, RS2, and RS3. Map panels were creating using ArcGIS® software by Esri. ArcGIS® and ArcMap™ are the intellectual property of Esri and are used herein under license. Copyright © Esri. All rights reserved.

Three independent sites were selected for this study (Figure 4-2). Rock-Slope 1 (RS1, milepost 71) is a nearly vertical (70° to 90°) road cut approximately 50 to 60 m high and 140 m wide. RS1 is composed of well-indurated dark mudstone of the Matanuska Formation. Rock-Slope 2 (RS2,

milepost 85.5) is a 60° road cut approximately 8-10 m high and 40 m wide. RS2 consists of highly fractured, fine to medium-grained, moderately weathered grey and tan hard sandstone of the Chickaloon Formation. The fractures are oriented such that the sandstone is broken into cobble-sized blocks. Rock-Slope 3 (RS3, milepost 87) is a 55° slope approximately 10 m high and 110 m wide. RS3 is predominantly comprised of soft carbonaceous siltstone of the Chickaloon Formation that has been intruded by hard, well-indurated mafic basalt sills. Numerous cantilever overhangs exist on RS3 because of localized erosion of the soft siltstone beneath the sills.

RS1

RS2

RS3

🌀 Ground Control Point (GCP)
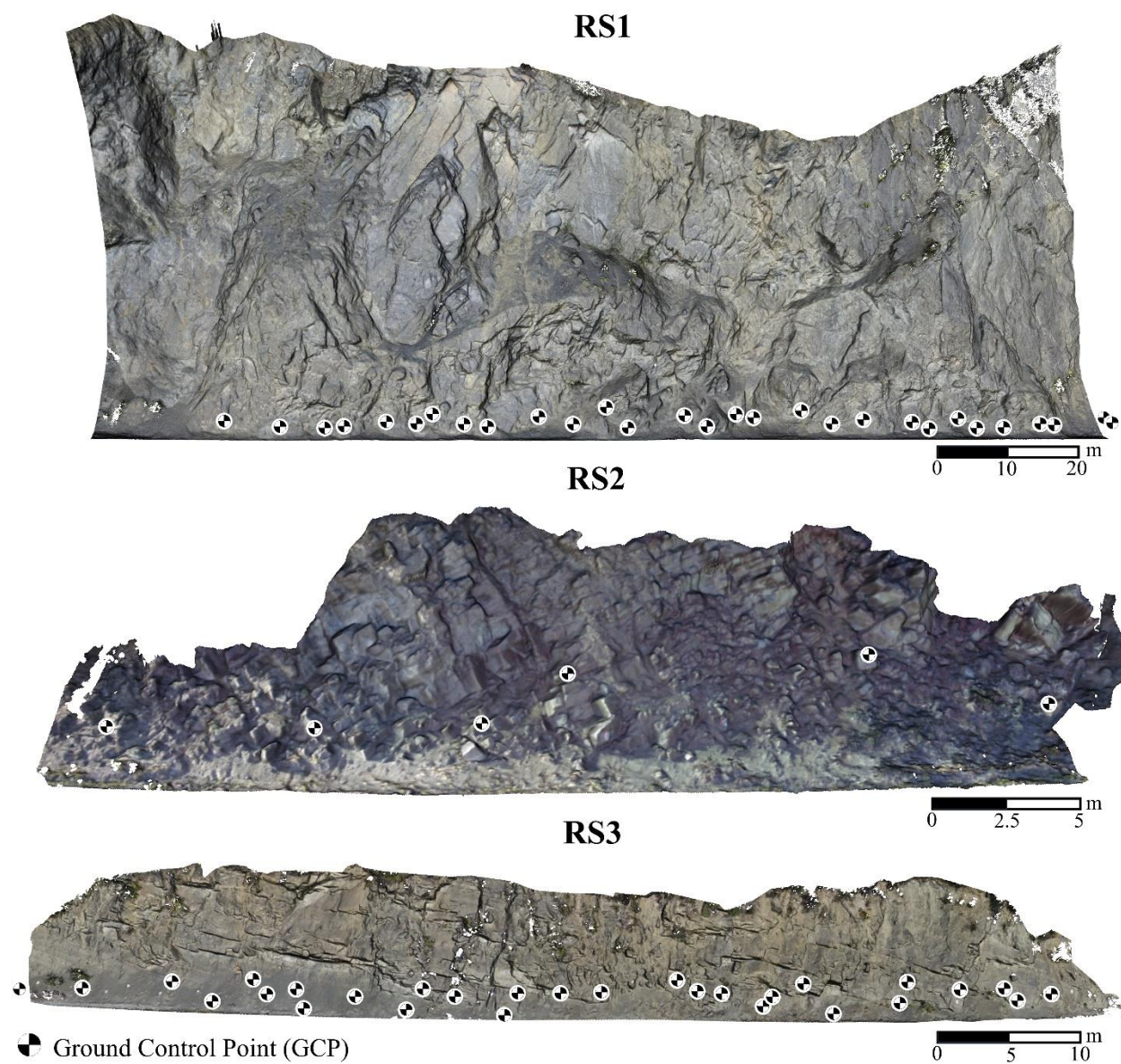
Figure 4-2: SfM-derived 5 cm surface models of the three rock slopes (RS1, RS2, and RS3) with the layout of black & white targets used as ground control points (GCP).

4.5   METHODOLOGY

4.5.1   Data Collection

4.5.1.1   Survey Control

A survey control network was developed for each study site to ensure proper scaling of the SfM reconstructions and for geo-referencing of both the SfM and TLS data. The control network consisted of Static and Rapid Static (RS), Global Navigation Satellite System (GNSS) occupations, and paper-based black & white targets, which served as GCPs. Two types of paper-based GCPs were used, generic black & white targets, commonly used in TLS survey workflows, and PhotoScan branded targets which can be auto-extracted in the Agisoft PhotoScan software (Agisoft, 2017). The layout of GCPs for each rock-slope site is presented in Figure 4-2. Sites RS1 and RS3 have GCPs that are not located on the selected rock-slope surface. These GCPs were used during development of the SfM models; however, they do not lie within the clipped region of the rock-slope. Components of the survey control network were tied together using a Leica TS15 (1") total station instrument. Two total station positions were used to establish the control network for both RS1 and RS3. A single total station position was adequate for RS2 given its limited horizontal and vertical extent. Processing of the total station data and subsequent adjustment of the control network was performed in StarNet 8.0 (Control Network Processing Section). The control network was established in the Alaska State Plane Coordinate System Zone 4, North American Datum 1983 (2011) Epoch 2010.00. Orthometric heights were estimated in the North American Vertical Datum of 1988 by differencing the ellipsoid heights with geoid heights from GEOID 12A.

Two types of RS observations were collected: RS control points positioned along the highway and marked with a magnetic survey nail, and scan position occupations acquired using a scanner mounted GNSS receiver. A survey-grade GNSS receiver (Leica GS14) was set up over an established control point and served as a base station to post-process short (< 15 min) RS GNSS observations using relative positioning techniques.

RS control points were incorporated into the survey control network using a TS instrument, prism rod, and 360° prism. The center point of all black & white paper target placed within a scanned/imaged scene was acquired by the TS in reflectorless mode.

The TS was also used to acquire reflectorless points scattered across the rock-slope faces. The purpose of these points is twofold, first to serve as an independent reference for evaluating the accuracy of the TLS-derived surface models and second, to evaluate the accuracy of SfM models in portions of the rock-slope unoccupied by GCPs. The rock-slope TS points are not to be confused with the survey control network; they were simply acquired with the TS instrument during the development of the control network.

4.5.1.2 TLS Survey

TLS surveys were performed using a Riegl VZ-400 laser scanner following a stop-and-go scanning approach similar to that presented in (Olsen et al., 2009; Olsen et al., 2015) for efficient mobilization of equipment along the shoulder lane of the highway. The TLS configuration included a calibrated, digital SLR (Nikon D700) camera and survey-grade Leica GS14 GNSS receiver mounted on top with known calibrated offsets. Precise inclination sensors (±0.008°, 1-σ) integrated into the TLS instrument (Silvia and Olsen, 2012) enable the scans to be accurately

leveled despite the unlevel wagon platform. Electronic Distance Measurement (EDM) scaling corrections were applied for atmospheric conditions, including temperature, pressure, and relative humidity. All scans had a field-of-view of 360° horizontally and +60° to -40° vertically relative to the horizontal plane. Scans were acquired from the shoulder opposite of the rock-slope at 40-60 m intervals (adapting to features of interest on the cliff) with an angular resolution of between 0.02 and 0.05°.

Prior to collection of TLS scans at each site, black and white pattern targets mounted to rigid clipboards were placed throughout the anticipated scanned scene.

4.5.1.3 UAS Imagery

Aerial photographs were obtained using a DJI Phantom 3 Professional quadcopter UAS platform. The Phantom 3 weighs 1.3 kg (including camera payload), is approximately 40-cm-wide, and has a flight endurance of about 20 minutes. The UAS platform includes an integrated 3-axis gimbal system to stabilize the camera during flight, thus minimizing vibration-induced blur in the aerial images. The gimbal provides a pitch range of -90° (i.e., nadir) to +30°, which can be adjusted in-flight using DJI's mobile flight control application GO. The Phantom 3's integrated camera has a 20 mm (35-mm equivalent) f/2.8 lens coupled with a 6.2 mm x 4.6 mm sensor that produces 12.4-megapixel images with an effective resolution of 4000 x 3000 pixels. Similar to the terrestrial images, the aerial photographs were obtained with a fixed focal length (i.e., no zooming), in bright daylight, and recorded in RAW image format. The UAS was flown in the manual mode (i.e., without a pre-programmed flight path) by a pilot positioned within sight of the aircraft at the base of each rock-slope. An automated flight plan solution that was capable of maintaining a safe distance from the near-vertical rock-slopes while avoiding

obstacles such as vegetation was not available. During the flight, a second crew member operated the UAS camera using the DJI GO application. The UAS was flown at altitudes ranging from approximately 10 m to 100 m above the base of each rock-slope. The aerial platform provided greater flexibility for positioning the camera system, allowing us to obtain images from a variety of perspectives including close-range views of incised and recessed morphological features (e.g. small gorges) and broad-range views of nearly the entire rock-slope. Attempts were made to capture imagery with the camera oriented approximately perpendicular to the rock-slope surface. In general, the aerial photographs of the rock-slope face were obtained in a gridlike pattern with ~8 m horizontal spacing along ~8 m-spaced lines of fixed altitude, resulting in approximately 80% overlap in the images. Photographs were captured at downward pitches (-60° to -10°), capturing benches and other features that were not visible from the ground. The median distance of the UAS from the rock-slope was 11 m, 10 m, and 14 m for RS1, RS2, and RS3, respectfully. The UAS aerial photography required about 40 minutes to complete at each site, including time for at least one landing and re-launch sequence for battery replacement.

4.5.1.4 Terrestrial Imagery

Terrestrial photographs were acquired using a Sony Cyber-shot DSC-RX10 II digital camera with a 24-200 mm (35-mm equivalent) f/2.8 lens and 13.2 mm by 8.8 mm sensor, resulting in images with an effective resolution of 20.2 megapixels (5496 x 3672). Before the fieldwork in Alaska, we performed trial photography campaigns at a benchmarked outdoor test site to determine the optimal camera settings for the SfM acquisition. In our test trials, we obtained the most accurate results when the camera's focal length was fixed at 24 mm, and the aperture was set to f/5.6. Adopting these settings, we photographed the rock-slopes in bright ambient daylight

(flash was disabled) and recorded the images in RAW format. Although storage intensive, the RAW image format produces minimally processed "digital negatives" whose white balance and color grading can be subsequently adjusted, if necessary. The photographer shot the images in handheld mode from a position on the far road shoulder of the 2-lane highway located at the base of the rock-slopes. The camera-to-subject distances varied depending on the width of the shoulder area. Median camera-to-subject distances were 20 m, 9 m, and 10 m for RS1, RS2, and RS3, respectfully. Photograph locations were obtained at ~5 m intervals along the base of the rock-slopes, with the aim of having at least 50% vertical and horizontal overlap in the neighboring images. In general, single photographs from multiple perspectives were preferred over multiple photographs taken by pivoting from a single location. The terrestrial photography required about an hour to complete at each site.

4.5.2   Data Processing

4.5.2.1   Control Network Processing

The GNSS base station coordinates were established using the Static processing available through the National Geodetic Survey's (NGS) Online Positioning User Service (OPUS-S). RS GNSS control points were processed against the base station using baseline vector processing in Leica Geo Office v.8.3 (Leica Geosystems, 2012). These coordinates were also obtained using rapid-static processing available through the NGS's Online Positioning User Service (OPUS-RS) for validation.

For each site, a 3D, constrained, least squares adjustment of the control network was completed using StarNet 8.0 to produce the final coordinates and uncertainties for the control targets and reflectorless measurements on the rock-slope surfaces. The following observations were input for

the adjustment: GNSS control point coordinates and associated uncertainties obtained from OPUS (peak-to-peak error) and OPUS-RS (standard deviations), GNSS baseline vectors between the base station and rover positions with associated covariance matrices, and the measured distances, horizontal angles, vertical angles, and uncertainties for the total station measurements for each setup. The GNSS baseline vector uncertainties were scaled by a factor of 25 to account for the overly optimistic estimates (sub-mm) obtained during baseline processing (Ovstedal, 2000; Kashani et al., 2004; Weaver et al., 2018). A Chi-square statistical test against the stochastic model was completed and passed at the 5% level. Estimated propagated errors of the coordinates for the stations were <1.5 cm (3D RMS) at the network level and <7mm (3D RMS) at the local level. Note that these estimates do not include geoid modeling error.

4.5.2.2 TLS Processing

Post-processing of TLS data is required to merge individual scans into a cohesive point cloud. This process requires adjustment of the position and orientation of a given scan location, resulting in a rigid-body transformation of the 3D point cloud acquired from that location. Information derived from the onboard inclination sensors, the top-mounted GNSS receiver and the relative position of GCP targets captured in the scan enable the determination of transformation parameters, including rotations and translations along orthogonal axes.

Prior to performing local registration of the point cloud data, individual scans were leveled in accordance with values reported by the onboard inclination sensors. Local registration and geo-referencing of the TLS data was performed in Leica Cyclone v.9.1 software (Leica Geosystems, 2015) using target matches and cloud-to-cloud surface matching constraints. The co-registered

point clouds were subsequently geo-referenced using both the adjusted survey control network and the scan position coordinates derived from the top-mounted GNSS receiver.

Quality control of point cloud registrations included a review of misalignment error vectors for target constraints, a review of total error associated with cloud-to-cloud constraints, and visual inspection of registered point clouds, including cross-section inspection. Visual inspections of the registered point clouds were performed to identify the presence of any point cloud misalignment artifacts that would require re-registration.

4.5.2.3   SfM Processing

Image-based 3D reconstruction was performed using Agisoft PhotoScan Professional v.1.3.4 (Agisoft, 2017). Three models were developed for each study site: Ground (solely ground-based imagery), UAS (only the UAS imagery), and Combo (ground and UAS imagery). Prior to importing the digital images into PhotoScan, the UAS-based images (DNG format) were processed using the DJI DNG Cleaner software and both the cleaned DNG and RAW images were converted to JPEG using the Adobe Lightroom software.

The "Align Photos" tool was used for initial camera alignment and subsequent development of a sparse 3D point cloud with the following settings: Accuracy = High, Generic preselection, Key point limit = 45,000, and Tie point limit = 4,000. Following the creation of the sparse point cloud, GCP coordinates derived from the survey control network for each site were imported. The "Detect Markers" tool was used to automatically extract the centers of any PhotoScan branded targets. The centers of additional non-PhotoScan targets were manually extracted from the imagery. All marker assignments, including those auto-extracted from PhotoScan targets,

were reviewed to ensure proper extraction of GCP centers and to omit constraints relying on blurry images. After this thorough review, the "Optimize Cameras" tool recalculated external and internal orientation (including lens distortion parameters) of the camera(s) to refine all GCP markers. The "Build Dense Cloud" tool then generated the final high-resolution point cloud with the following settings: Quality = High, and Depth filtering = Mild.

4.5.2.4 Surface Generation

Finalized SfM and TLS point clouds were cropped to identical extents, including only portions of a given rock-slope to be studied. Coarse vegetation removal was performed by manually selecting and deleting regions of vegetation in the point cloud. Efforts were made to be consistent when performing manual vegetation removal; however, in many cases, vegetation in a given area appeared differently in the SfM and TLS datasets. For example, a dense shrub observed as a surficial shell of points in the SfM data may appear as a noisy fuzz of points in the TLS data resulting from the laser beam penetrating the foliage resulting in mixed pixels. 3D surface models (5 cm resolution) for each study site were created from the cropped and cleaned point cloud data using the optimal plane triangulation methodology presented in (Olsen et al., 2015).

4.5.3 Accuracy Assessment

Two independent references (both tied to the aforementioned control network) are available for assessing the accuracy of the SfM models: the TLS-derived surface models, and the rock-slope TS points. In this case, the TLS surface models are preferred over the rock-slope TS points because they offer many more nodes/vertices for 3D differencing. When comparing two surface models of similar extent, all nodes that comprise a surface mesh can be compared to those of the

reference surface. The quantity of rock-slope TS points for the different study sites ranges from 50 to 100 discrete points, which is far fewer than the 1×10^5 to 2×10^6 nodes made available by the surface models.

Prior to assessing the accuracy of the SfM-derived surface models, the accuracy of the TLS-derived models was evaluated using the rock-slope TS points. This important step validates the TLS surface models as an appropriate reference for assessing the accuracy of the SfM models. They also serve as an additional reference for assessing the accuracy of the SfM models.

Surface-to-surface (comparing TLS and SfM surfaces) and surface-to-point (comparing a surface to the rock-slope TS points) assessments were completed using the "Color from Distance" tool in Maptek I-Site Studio 6.0 software (Maptek, 2016). A maximum distance threshold of $\pm$ 0.20 m was chosen as not to include larger discrepancies associated with the presence of inconsistent vegetation removal. The reported distances represent 3D discrepancies measured along the surface normal of the base surface to the closest point or surface node. Comparison of the interpolated surface models was chosen instead of a solely point-to-point evaluation because the accuracy of surface models is more relevant to our preferred, unstable rock-slope assessment and monitoring techniques (Olsen et al., 2015; Dunham et al., 2017). In addition, point-to-point comparisons are more appropriate for preliminary error assessments as they are prone to outliers and differing point densities (Eltner et al., 2016). Nevertheless, point-to-point comparisons performed using CloudCompare software (Girardeau-Montaut, 2017) achieved similar results.

4.5.4   Quality Evaluation

The SfM quality evaluation focuses on the suitability of SfM for the assessment of rock-slopes. Multiple characteristics including point density, completeness, and the capabilities of SfM to capture surface morphology (e.g., slope and roughness) were evaluated relative to TLS.

Point density was determined by sub-sampling the TLS and SfM point clouds into 5 x 5 cm grid cells and recording the number of points within each cell. The completeness metric was determined based on relative values of model surface area at each site. A baseline surface area representing full completeness was established for each site based on the Combo SFM point cloud with surface data gaps (holes) filled. Small holes in the 3D surface models were filled using the thin plate spline technique presented in (Olsen et al., 2015). The Combo SfM model was assumed to be the most complete because of its use of both ground and UAS-based imagery which minimizes the occurrence of data gaps. Completeness values were determined by comparing the surface area of a model with no hole filling to the site-specific baseline surface area representative of a complete model (Eq. 1).

$$Completeness = \left(\frac{Surf.\ Area\ of\ Model\ with\ out\ Holes\ FIlled}{Surf.\ Area\ of\ Combo\ SfM\ Model\ with\ Holes\ Filled} \right) \times 100 \qquad (1)$$

Comparative distribution plots were developed to present the differences in surface morphology captured by TLS and SfM methods. The chosen surface parameters include slope, surface roughness, and the Rockfall Activity Index (RAI). RAI is a point-cloud-derived, morphology-based classification methodology used to evaluate rockfall hazards (Dunham et al., 2017). Two types of surface roughness (standard deviation of slope) were examined: small window (SW) roughness, which is computed using a 35 x 35 cm window; and large window (LW) roughness

utilizing an 85 x 85 cm window. The window sizes were selected because of their relevance to the RAI methodology.

Lastly, a visual qualitative inspection of the TLS and SfM derived point clouds was performed using an immersive virtual reality (VR) system, GeoMat VR (O'Banion 2016), which was constructed based on a hardware and software configuration developed at UC Davis (Kreylos 2017). GeoMat VR consists of a 65-inch active 3D LED television coupled with an Optitrack infrared (IR) tracking array and VR software (Vrui). The array of three IR cameras track the user's stereoscopic 3D glasses and a Nintendo Wii remote used for data interaction. When working with high resolution, complex 3D point cloud data, an immersive VR system supporting stereoscopic visualization facilitates enhanced data interaction and spatial awareness. For this study, both TLS and SfM point clouds were added to the same environment for direct visual comparison. The color of the SfM cloud was modified to have a red tint so these points could easily be differentiated from those gathered by TLS. This advanced visualization technique enabled detailed inspection of geometric discrepancies between the TLS and SfM datasets.

4.6 RESULTS

SfM and TLS point cloud data attributes (Table 4.1) include the type of point cloud, the number of images used for SfM reconstruction or the number of scans for TLS data, the quantity of GCP targets used for registration, the total amount of points in the point cloud on the rock-slope surface, and the mean point density for each dataset.

Table 4.1: Details of the SfM and TLS point clouds.

Site	Approximate Slope Surface Area (m²)	Type	Number of Images/Scans	Number of GCPs	Total Points	Mean Point Density (pts/m²)
RS1	9,300	Ground SfM	140	29	43,441,327	6,151
		UAS SfM	132	25	19,807,042	2,804
		Combo SfM	272	29	39,411,287	5,579
		TLS	6	29	55,681,383	7,875
RS2	450	Ground SfM	124	8	43,839,216	122,830
		UAS SfM	30	5	4,420,183	12,378
		Combo SfM	154	7	31,091,288	86,751
		TLS	3	10	12,095,566	33,871
RS3	1,680	Ground SfM	164	29	81,738,569	63,585
		UAS SfM	61	25	11,571,375	9,001
		Combo SfM	225	29	63,474,055	49,361
		TLS	5	30	28,706,943	21,684

The number of images and TLS scans, and GCPs used for RS1 and RS3 are very similar; however, their approximate surface areas are quite different (further discussed in Discussion section). Site RS2 required fewer images, TLS scans, and GCPs due to its relatively smaller horizontal extent. For RS1, the TLS point cloud has the largest number of points, followed by the Ground SfM, Combo SfM, and UAS SfM point clouds, listed in order of decreasing point count. The point count for RS2 and RS3 indicate a different trend in which the Ground SfM dataset has the largest quantity of points, followed by the Combo SfM, TLS, and UAS SfM datasets. A significant difference in total points exists between the TLS datasets for RS1 and RS2 despite the fact that there is a similar number of scans completed. This occurs predominately because the rock-slope is much taller for RS1. For all three rock-slope sites, the Ground SfM model has a greater number of points and higher mean point density when compared to the Combo SfM model. Average ground resolution (i.e., ground sampled distance (GSD)) of the SfM imagery as reported by PhotoScan is as follows: 7.12 mm/pixel, 12.5 mm/pixel, and 9.18 mm/pixel for the RS1 Ground, UAS, and Combo SfM models, respectfully; 1.77 mm/pixel, 5.85 mm/pixel, and 2.25 mm/pixel for the RS2 Ground, UAS, and Combo SfM models, respectfully; and 2.09

mm/pixel, 6.93 mm/pixel, and 2.94 mm/pixel for the RS3 Ground, UAS, and Combo SfM models, respectfully.

4.6.1 Accuracy Assessment

Rock-slope surface maps depicting the spatial distribution of geometric discrepancies identified between the SfM and TLS surface models were developed for each of the study sites (Figure 4-3, Figure 4-4, Figure 4-5). The minimal discrepancy between the SfM and TLS surface models is represented by regions colored in green. Regions colored in shades of blue represent where the SfM surface is located in front of the TLS surface, and shades of red represent where the SfM surface is located behind the TLS surface model. Regions of the rock-slope colored magenta indicate surface discrepancies larger than a $\pm$ 0.2 m threshold to omit vegetation-derived discrepancies from the evaluation.

Similar error patterns are observed for the various SfM surface models depicted in Figure 4-3, Figure 4-4, and Figure 4-5. The Ground and Combo SfM surface models demonstrate close alignment with the TLS surfaces; while, the UAS SfM surfaces result in a distinct error pattern, which includes a discontinuity across the rock-slope face where discrepancies with the TLS surface transition from positive to negative. Statistics, including the mean, standard deviation, RMSE, and 95% confidence error of the 3D discrepancies of the surface-to-surface comparisons are included in Table 4.2. The percentage of the SfM-derived surface model in front of the TLS surface model is also provided. Values deviating significantly from 50% indicate a drifting trend for the SfM surface.

Results of the surface-to-surface comparison between SfM and TLS models indicate 3D errors at 95% confidence ranging from $\pm$ 0.044 m to $\pm$0.048 m for Ground SfM models, $\pm$ 0.048 m to $\pm$ 0.112 m for UAS SfM models, and from $\pm$ 0.041 m to $\pm$ 0.048 m for Combo SfM models. Likewise, the results of the surface-to-points comparison between TLS and SfM surface models and the rock-slope TS points are presented in Table 4.3. Comparison of the TLS surface models to the TS points indicates a consistent surface model accuracy of $\pm$ 0.015 m at 95% confidence across all sites.

RS1 Surface Comparisons
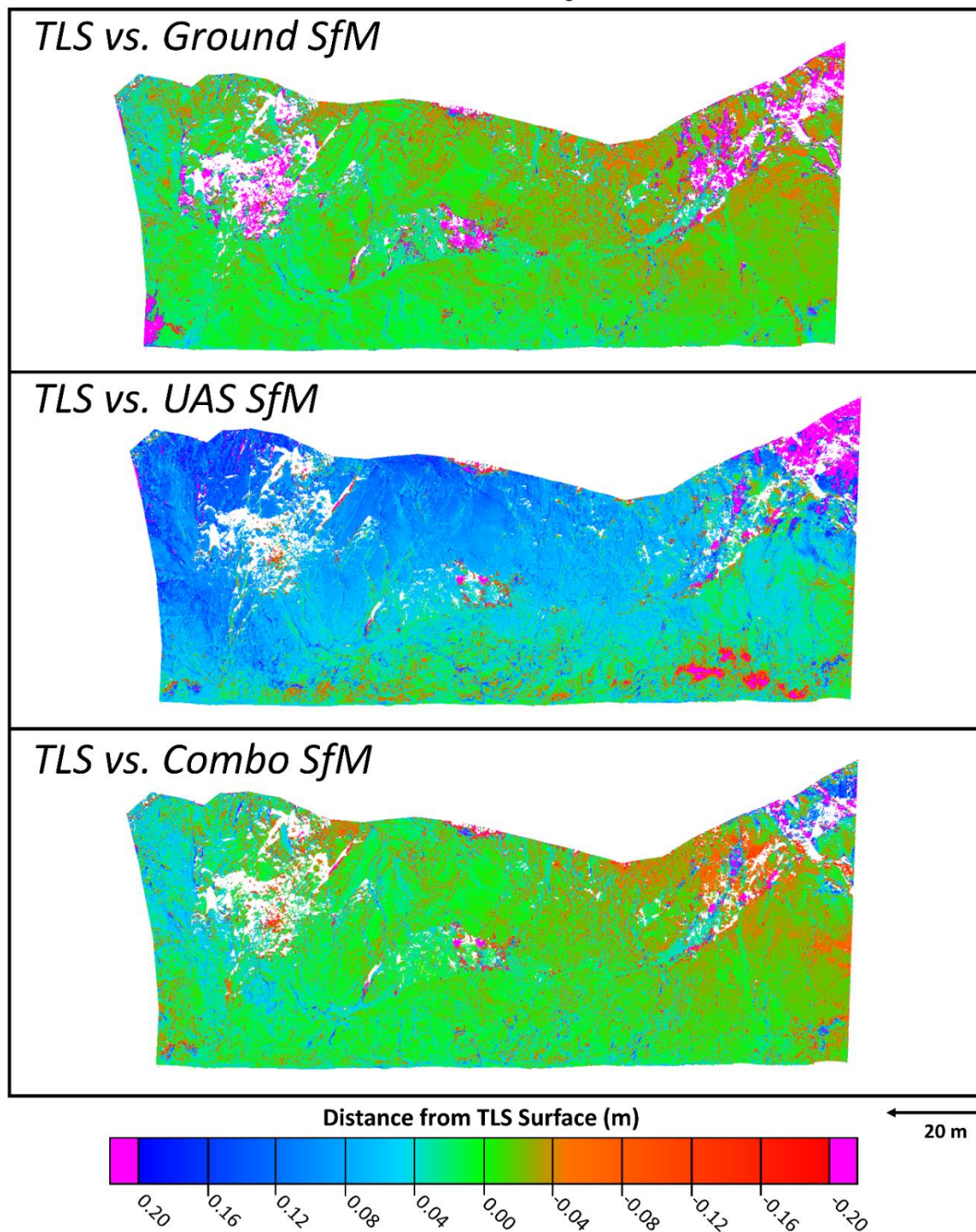
Figure 4-3: Geometric discrepancies for RS1 identified by differencing TLS and SfM surface models.
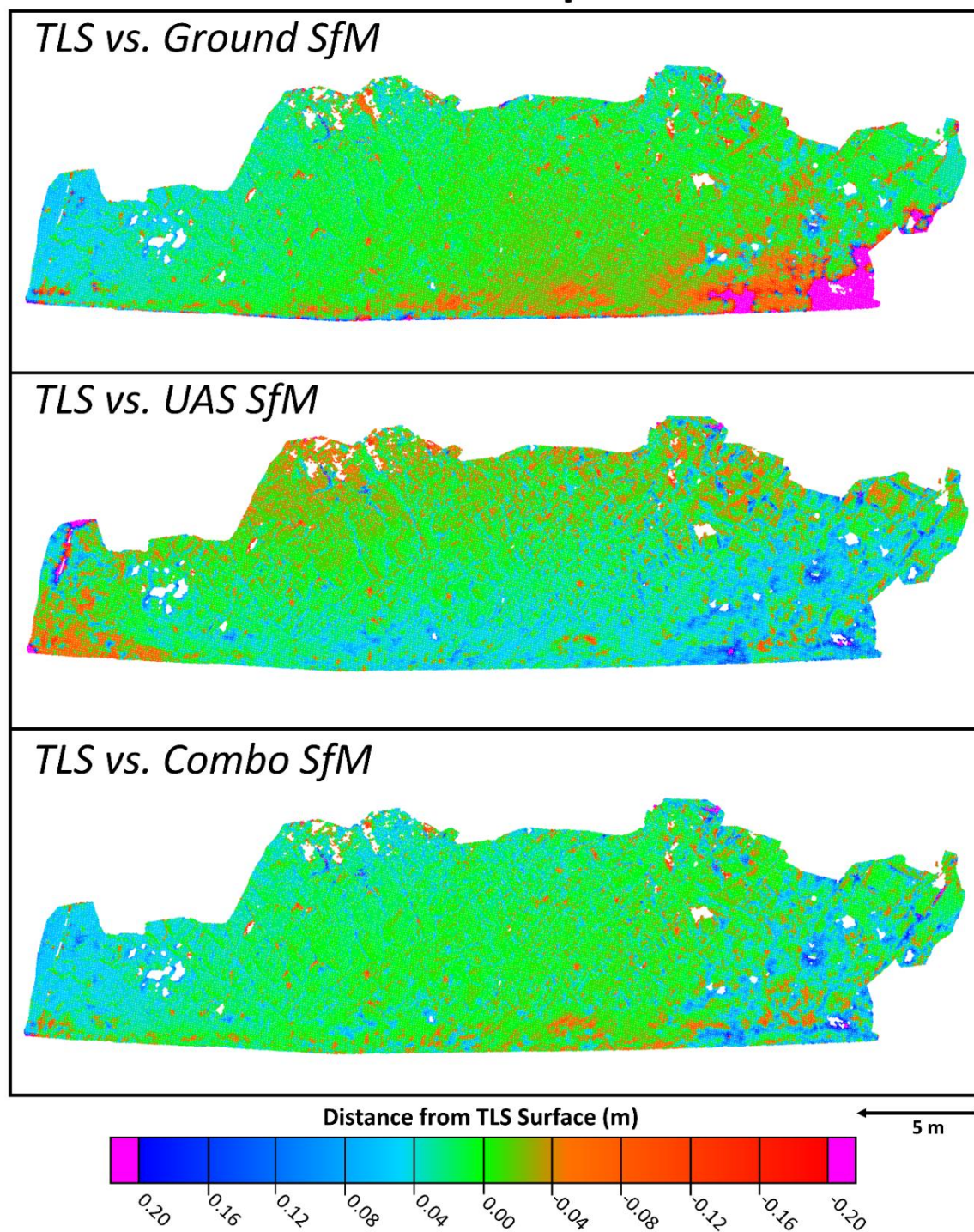
Figure 4-4: Geometric discrepancies for RS2 identified by differencing TLS and SfM surface models.

RS3 Surface Comparisons
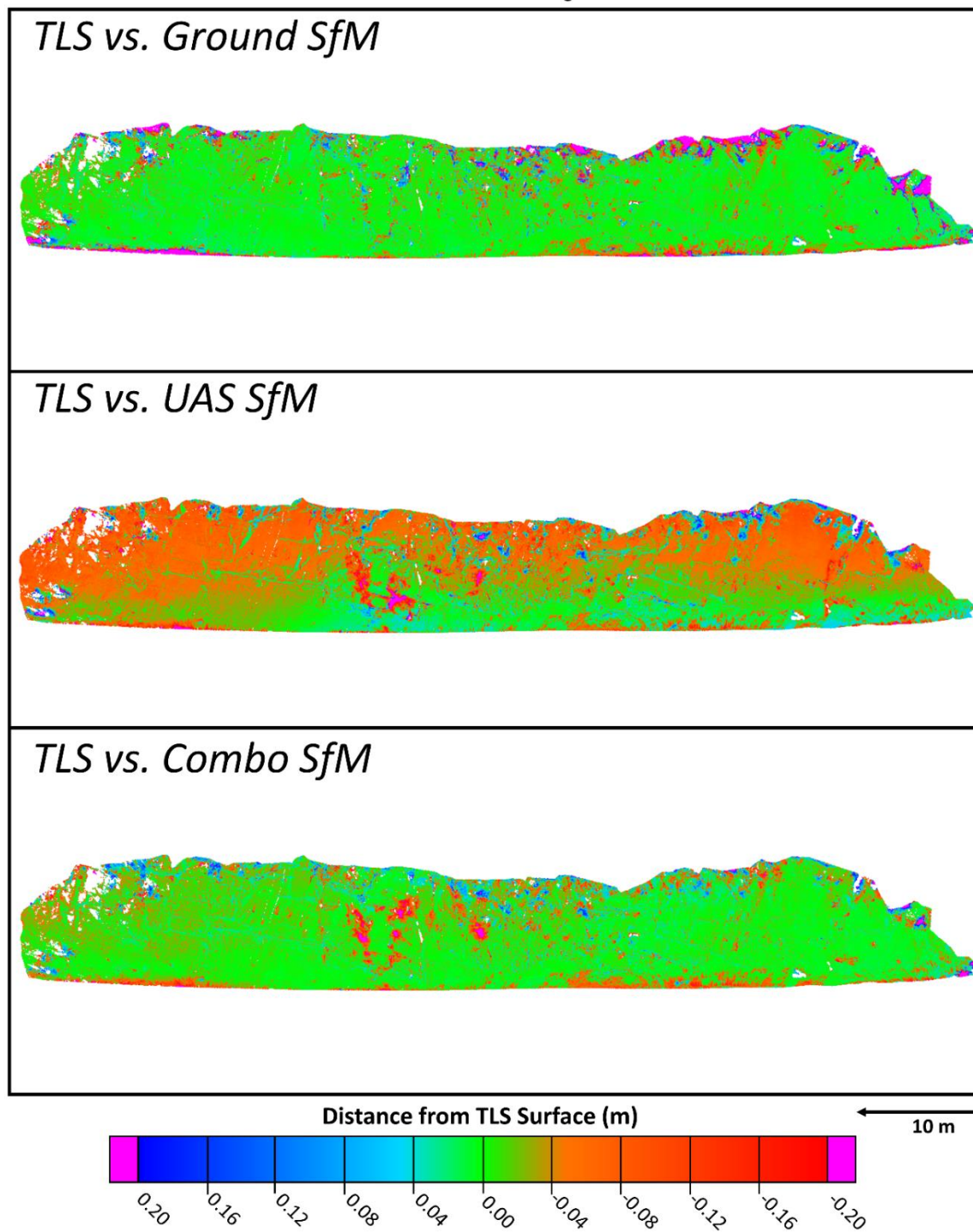
Figure 4-5: Geometric discrepancies for RS3 identified by differencing TLS and SfM surface models.

Table 4.2: Statistics regarding 3D geometric discrepancies between SfM and TLS-derived 5cm resolution 3D surfaces.

SfM Model	Type	Mean Diff. (m)	σ (m)	RMSE (m)	Error 95% Conf. (m)	% of SfM in Front of TLS
RS1	Ground SfM	-0.003	± 0.029	± 0.029	± 0.047	55.4
	UAS SfM	-0.051	± 0.046	± 0.069	± 0.112	94.1
	Combo SfM	-0.006	± 0.029	± 0.030	± 0.048	60.5
RS2	Ground SfM	-0.002	± 0.027	± 0.027	± 0.044	58.3
	UAS SfM	-0.010	± 0.028	± 0.030	± 0.048	65.3
	Combo SfM	-0.010	± 0.023	± 0.025	± 0.041	72.9
RS3	Ground SfM	0.000	± 0.030	± 0.030	± 0.048	56.9
	UAS SfM	0.020	± 0.036	± 0.041	± 0.066	23.0
	Combo SfM	0.003	± 0.026	± 0.027	± 0.043	43.8

Table 4.3: Statistics regarding 3D geometric discrepancies between SfM and TLS-derived 5cm resolution 3D surfaces and the Rock-Slope TS points.

Site	Type	Mean Diff. (m)	σ (m)	RMSE (m)	Error 95% Conf. (m)	% of Surface in Front of TS Points
RS1	Ground SfM	-0.001	± 0.015	± 0.015	± 0.025	57.14
	UAS SfM	-0.032	± 0.041	± 0.052	± 0.084	82.69
	Combo SfM	-0.006	± 0.020	± 0.021	± 0.033	56.19
	TLS	0.002	± 0.009	± 0.010	± 0.015	41.90
RS2	Ground SfM	0.002	± 0.024	± 0.025	± 0.040	48.98
	UAS SfM	0.006	± 0.029	± 0.029	± 0.047	36.73
	Combo SfM	-0.001	± 0.024	± 0.024	± 0.039	57.14
	TLS	0.003	± 0.009	± 0.009	± 0.015	31.25
RS3	Ground SfM	-0.001	± 0.008	± 0.008	± 0.013	63.86
	UAS SfM	0.013	± 0.025	± 0.028	± 0.046	22.89
	Combo SfM	-0.001	± 0.011	± 0.011	± 0.017	53.01
	TLS	0.001	± 0.009	± 0.009	± 0.014	55.42

4.6.2 Quality Evaluation

4.6.2.1 Point Density

Point density heat maps were developed for each of the three study sites (Figure 4-6, Figure 4-7, Figure 4-8). The rock-slope point density maps demonstrate both the varying magnitude and spatial distribution of point density throughout the different SfM and TLS point cloud datasets. A smaller point density range was applied to the color ramp for RS2 to account for the lower point densities identified for RS2. The Ground SfM surface models for RS2 and RS3 are saturated

with red due to their high point density relative to the other surface models generated for those sites. Comparative distribution plots of point density for the three rock-slope sites are presented in Figure 4-9.

Similar trends in point densities are observed for sites RS2 and RS3. Study site RS1 demonstrates unique results with regards to the relative distributions of point density. For RS1, the TLS point cloud has the highest mean point density and standard deviation. The ranking of the remaining SfM datasets is Ground SfM, Combo SfM, and UAS SfM, listed in order of decreasing mean point density. The point density evaluation for RS2 and RS3 reveals a ranking for mean point density that differs from that observed for RS1. Listed in order of decreasing mean point density, the Ground SfM data has the highest mean, followed by the Combo SfM, TLS, and UAS SfM datasets. Additionally, a clear separation in point density is observed for RS2 and RS3; this separation is not as apparent for RS1. When comparing results for RS2 and RS3, the standard deviations for all datasets are higher for RS2, resulting in a larger range of point density values across the rock-slope. The mean point density of the RS1 SfM models is around an order of magnitude smaller than the SfM point densities reported for RS2 and RS3.

All point density distributions computed for the Ground SfM model have a noticeable increase in low point density values. This increase is attributed to the relatively large quantity of zero values added to the Ground SfM datasets to account for data gaps that contribute to the lower completeness percentage of these data. Zero values were added to all SfM and TLS datasets to account for data gaps; however, changes to the distributions were negligible given the high completeness percentage of all but the Ground SfM datasets.
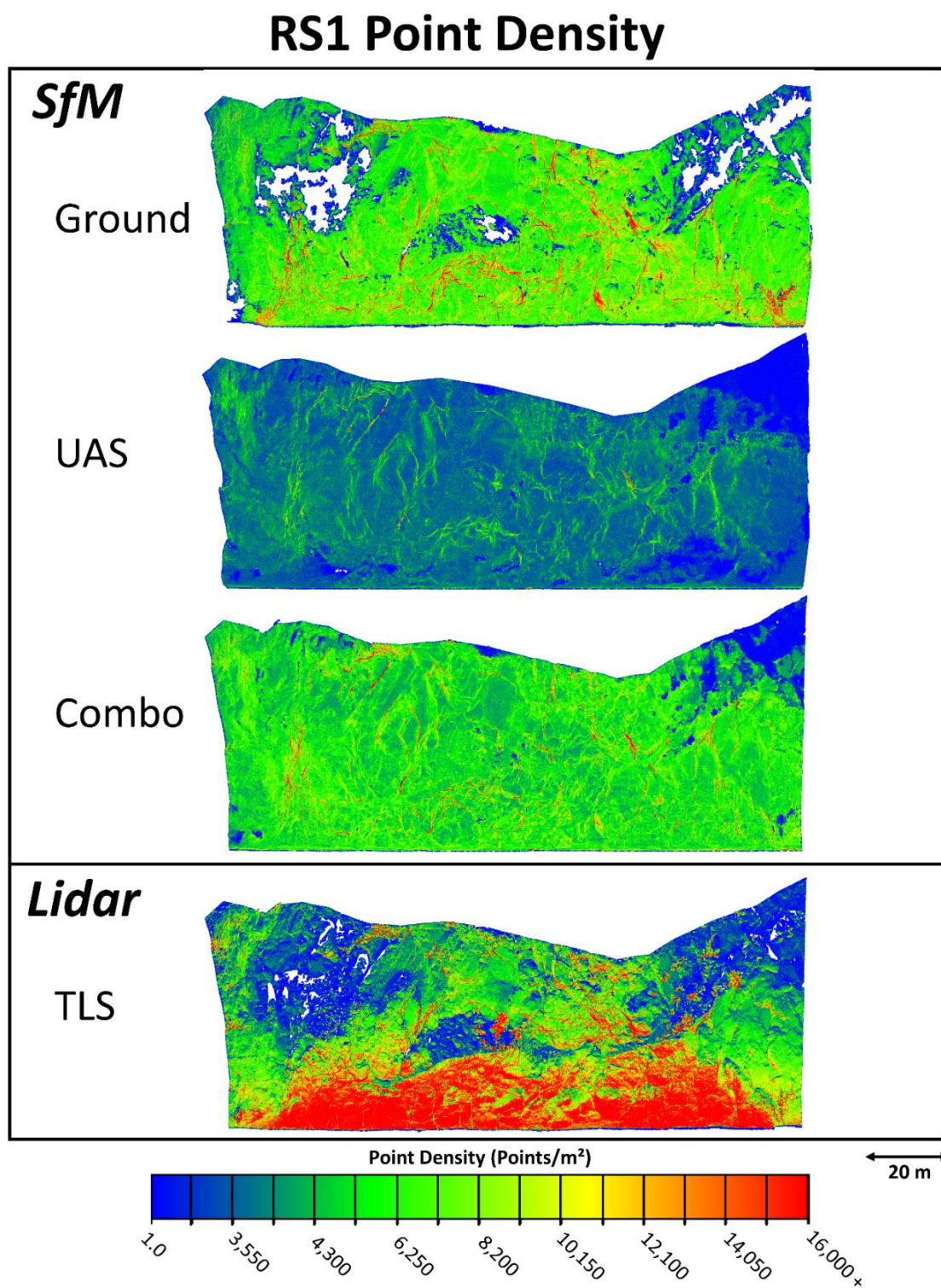
RS1 Point Density

Figure 4-6: Point density heat maps for RS1 SfM and TLS-derived 3D point cloud data.
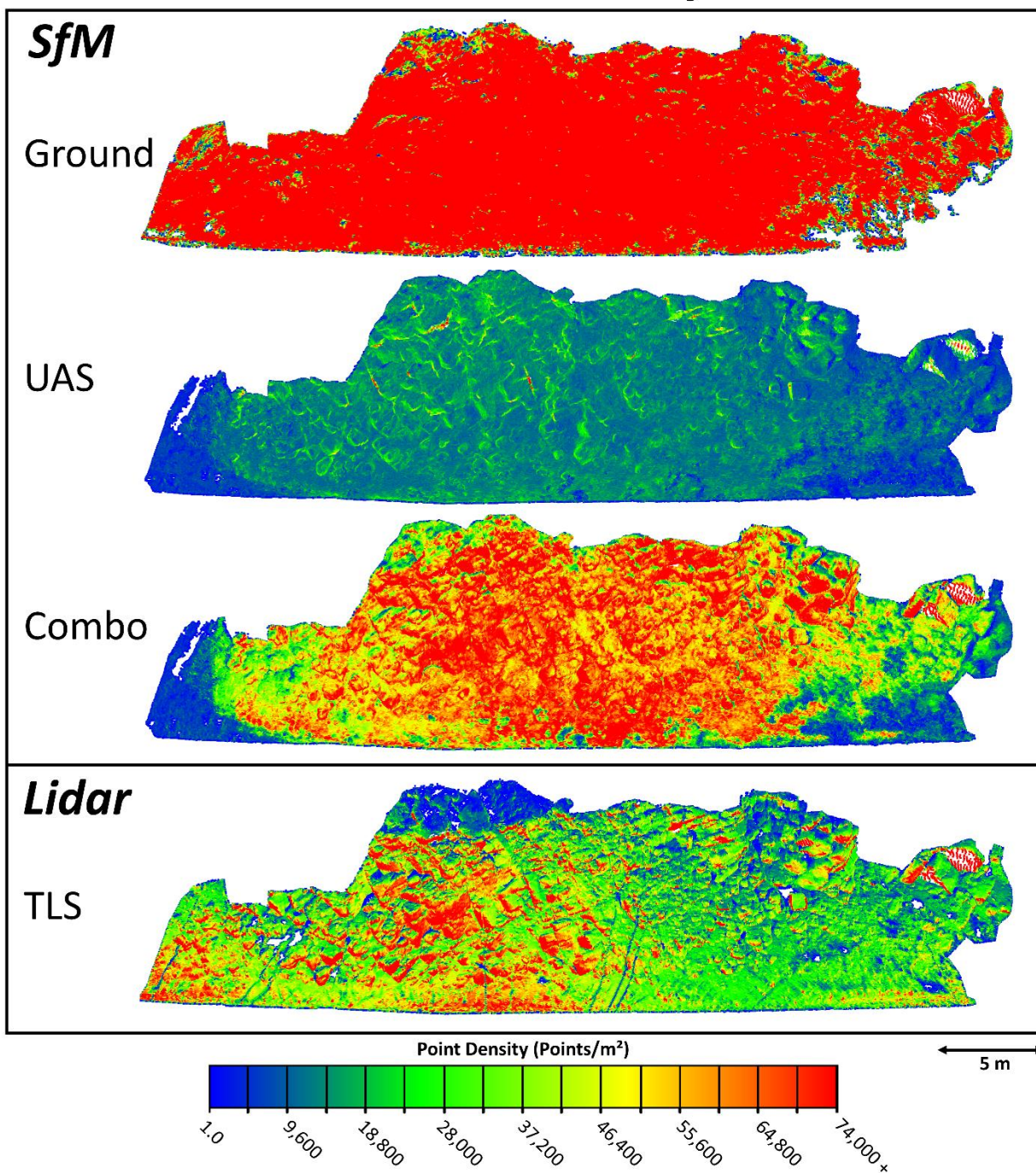
Figure 4-7: Point density heat maps for RS2 SfM and TLS-derived 3D point cloud data.
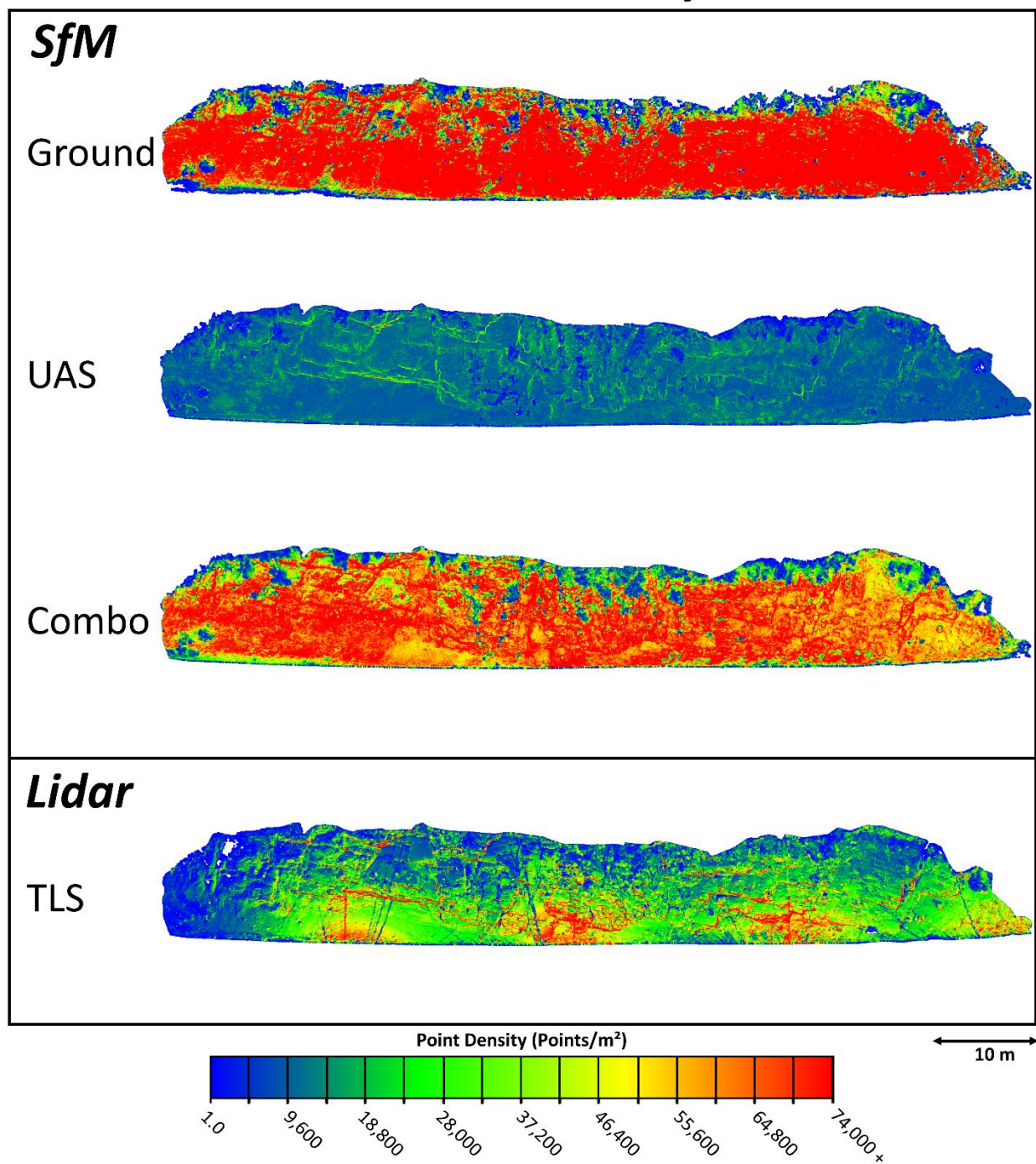
Figure 4-8: Point density heat maps for RS3 SfM and TLS-derived 3D point cloud data.
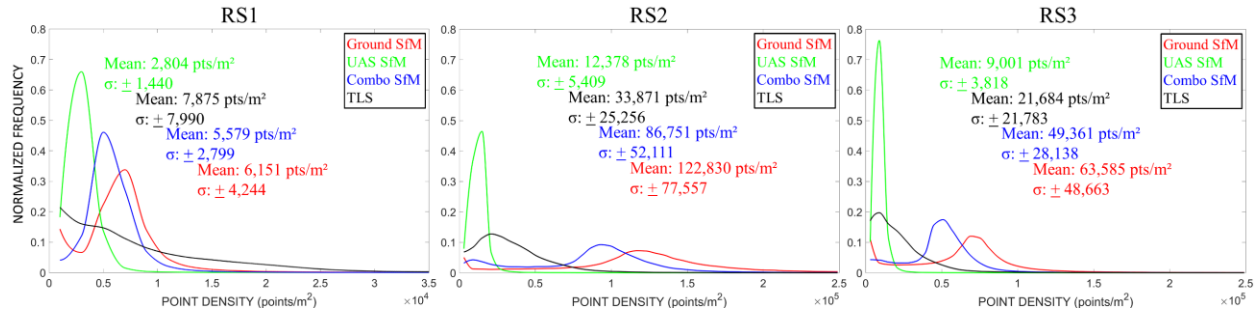
Figure 4-9: Comparative distribution plots of point density for SfM and TLS datasets.

4.6.2.2   Completeness

Completeness of the surface models range from 89.4% to 99.5% for RS1, 96.9 % to 99.8% for RS2, and 94.4% to 99.5% for RS3 (Table 4.4). For all three study sites, the Ground SfM models result in the least complete surface model, and the UAS or the Combo SfM models are the most complete. Paradoxically, the Ground SfM models contained the largest number of points.

Table 4.4: Completeness of TLS and SfM 5cm surface models, based on surface area calculations.

Site	Type	Completeness (%)
RS1	Ground	89.4
	UAS	99.5
	Combo	99.0
	TLS	92.4
RS2	Ground	96.9
	UAS	99.3
	Combo	99.7
	TLS	99.6
RS3	Ground	94.4
	UAS	99.5
	Combo	99.5
	TLS	98.6

4.6.2.3   Surface Parameters

Comparative distribution plots were developed to present the differences in surface morphology captured by TLS and SfM methods. Surface parameters evaluated for this study include slope,

SW surface roughness, and LW surface roughness (Figure 4-11, Figure 4-12, Figure 4-13). All distribution plots were normalized to account for differences in completeness amongst the surface models.

Overall, the normalized distributions of slope for the surface models at each site are very similar. The results for RS1 indicate the distributions of slope for the Combo and UAS SfM models differ from the distributions of slope for the Ground SfM and TLS models. The Combo and UAS SfM datasets have a localized increase in slope values at around 40° that is not observed in the others.

With regard to mean of SW roughness, the UAS SfM model is most similar to the TLS data for RS1, and the Ground SfM model is most similar to the TLS data for Sites RS2 and RS3. When examining standard deviation of SW roughness, the Combo SfM model is most similar to the TLS data for Sites RS1 and RS3, and the Ground SfM model is most similar to TLS for RS2 (Figure 4-11).
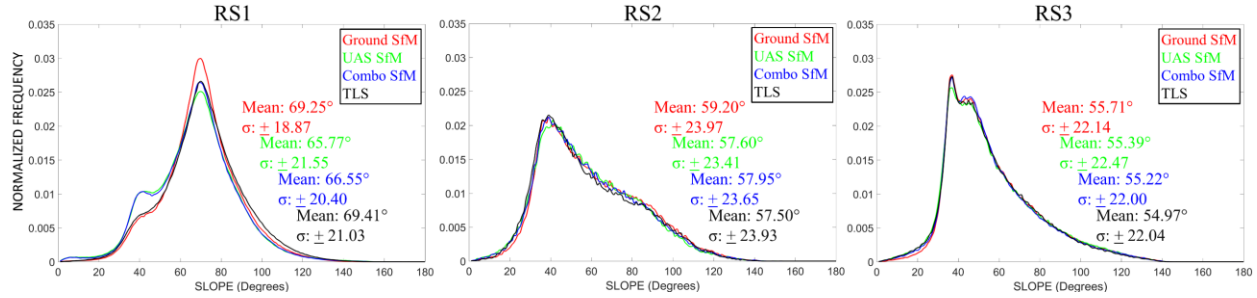
Figure 4-10: Comparative distribution plots for surface slope.
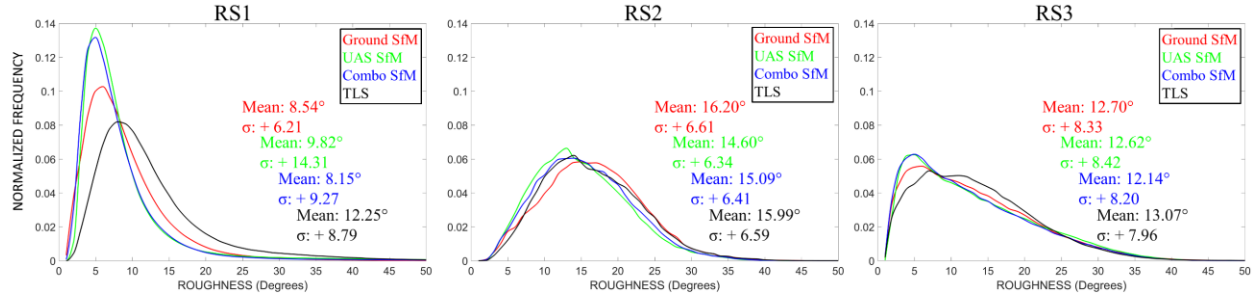
Figure 4-11: Comparative distribution plots for small window (35x35 cm) roughness.
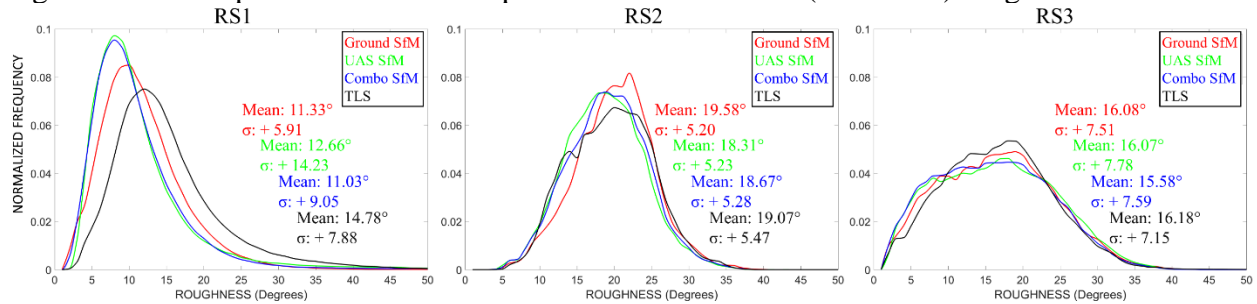
Figure 4-12: Comparative distribution plots for large window (85x85 cm) roughness.

For Site RS1, there is a clear separation in the distributions of SW roughness between the SfM and TLS datasets and the distributions for the Combo and UAS SfM models are very similar (Figure 4-11). The TLS distribution of SW roughness for RS1 is significantly different from the SfM datasets, indicated by an average mean shift of + 3.4°. For Sites RS2 and RS3, the distributions of SW roughness for the Ground SfM data are slightly shifted toward a higher roughness when compared to the other SfM datasets. Results for RS2 indicate similar distributions of SW roughness for the Combo SfM and TLS datasets; however, the TLS and Ground SfM distributions become more aligned for SW roughness values > ~22°. The mean SW

roughness values for the RS3 Combo SfM and TLS models are similar but, the distributions are different. The SW roughness distributions for the Combo SfM model has a clear increase in frequency at SW roughness values of ~5° that is not present in the TLS distribution (Figure 4-11).

In general, the results of the LW surface roughness evaluation are similar to those reported for the SW surface roughness with a few subtle differences. In terms of the mean of LW roughness, the UAS SfM model is most similar to the TLS data for RS1, the Combo SfM model is most similar to the TLS data for RS2, and the Ground SfM is most similar for RS3. When examining standard deviation of LW roughness, the Combo SfM model is most similar to the TLS data for Sites RS1 and RS2, and the Ground SfM model is most similar to TLS for RS3 (Figure 4-12).

For Sites RS2 and RS3, the distributions of LW roughness for the Ground and SfM data are slightly shifted toward a higher roughness when compared to the other SfM datasets. Results for RS2 indicate similar distributions of LW roughness for the Combo SfM and TLS datasets; however, the Combo SfM distribution has an increase in frequency at LW roughness values of ~15° with respect to the TLS distribution, and the Ground SfM model becomes more aligned with the TLS distribution for LW roughness values > ~25°. For Site RS3, the LW roughness distributions for all SfM models are shifted towards lower roughness values with respect to the TLS distributions. However, the SfM and TLS distributions become better aligned for LW roughness values > ~22°.

4.6.2.4   Rock-Slope Morphology Classification

The RAI classification evaluation is presented as comparative histogram plots in Figure 4-13. A significant over-prediction of intact rock (I) occurs for RS1 followed by an under-prediction of the fragmented (Df), closely spaced (Dc), and widely to moderately spaced (Dw) discontinuous rock units, as well as steep (Os) and cantilever (Oc) overhangs when compared to the TLS surface. The distribution of RAI classifications for RS2 is similar amongst the SfM and TLS surface models. The most significant discrepancies are an over-prediction of Df and an under-prediction of Dw by the UAS SfM data. Similar to the results for RS1, we observe an over-prediction of I and under-prediction of Dc for RS3; however, the discrepancies are not as large as those observed for RS1.

Overall, the RAI classifications for Ground SfM-derived surfaces are most similar to the RAI classifications determined for the TLS surfaces. Example RAI classification maps for RS1 are presented in Figure 4-14. The over-prediction of RAI Class I observed in Figure 4-13 is depicted in Figure 4-14 by the dominance of bright green observed for the SfM surface model. The insets presented in Figure 4-14 provide a close-up view of the RAI classifications the Combo SfM and TLS surface models. The TLS inset shows the prevalence of Dc and Dw classifications that is not observed in the insets of the SfM-derived surface.
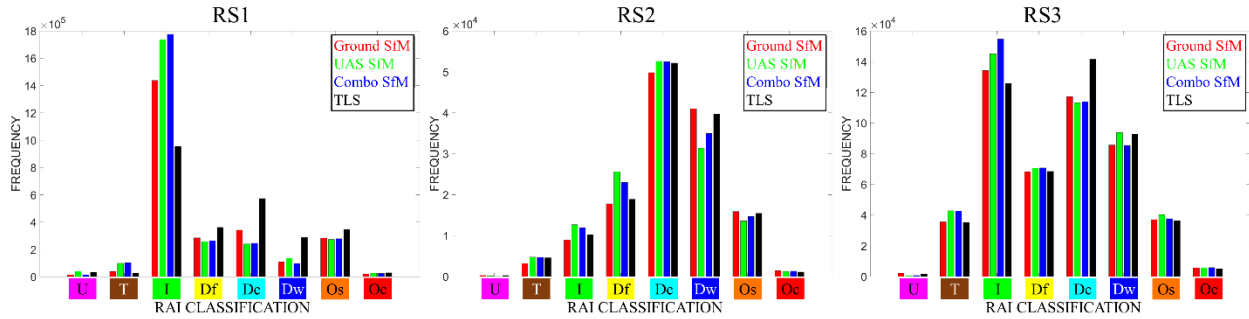
Figure 4-13: Comparative histogram plots for RAI classification. RAI classifications are as follows: Unclassified (U), Talus (T), Intact Rock (I), Fragmented discontinuous rock (Df), Closely spaced discontinuous rock (Dc), Widely to moderately spaced discontinuous rock (Dw), Steep overhang (Os), and Cantilever overhang (Oc).
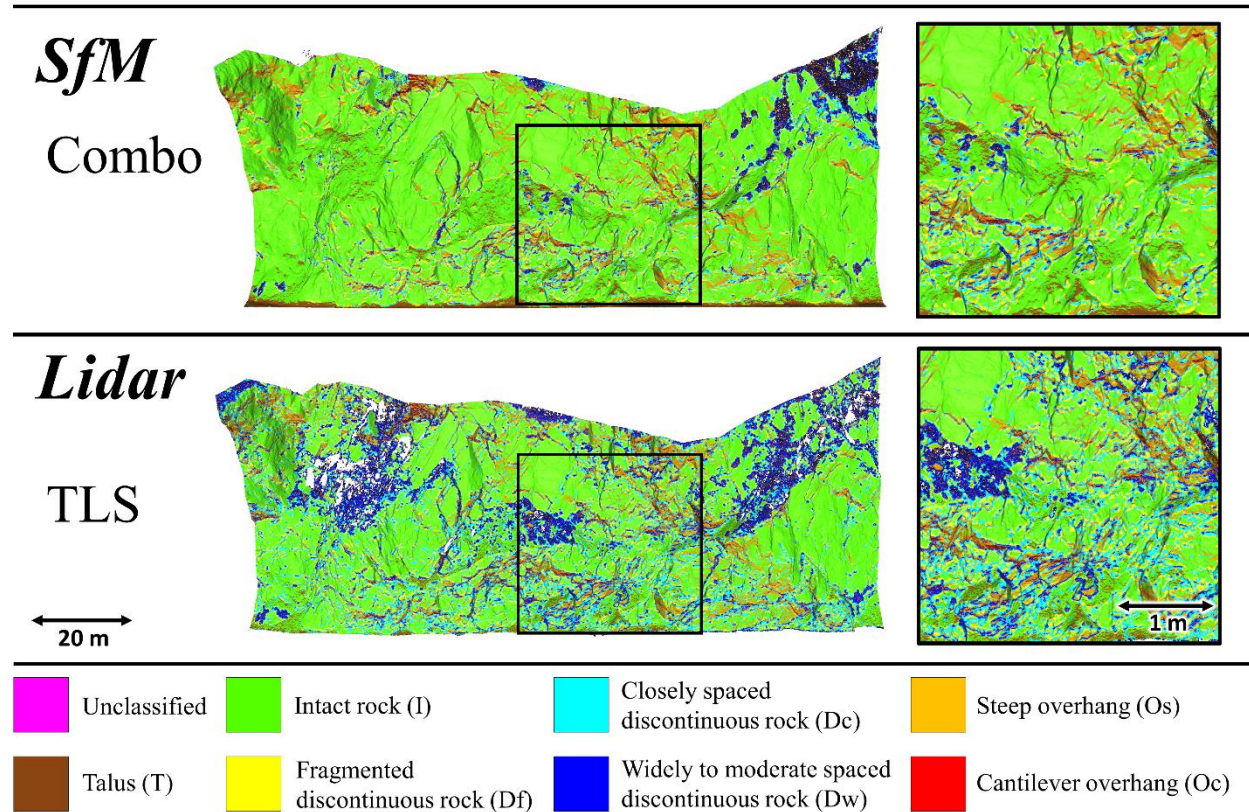
Figure 4-14: RAI classification for RS1.

4.6.2.5 GeoMat VR Inspection

Qualitative inspection of the TLS and SfM point cloud data in the GeoMat VR system revealed a prevalence of over-smoothing in the UAS and Combo SfM data. Many of the sharp edges associated with rock outcrop discontinuities, were observed to be more round and smooth when compared side-by-side with the TLS point cloud data (Figure 4-15). Over-smoothing was not as apparent in the Ground SfM point cloud data. Simultaneous visualization of the TLS and SfM point clouds also revealed the ability of UAS-based SfM to, in some scenarios, outperform TLS with respect to seeing beneath vegetation. This is attributed to the ability of UAS to occupy numerous advantageous points of view, allowing imaging around and beneath spurious vegetation (e.g., small trees and isolated shrubs). In areas of dense ground cover, TLS is observed to outperform UAS-based SfM methods.
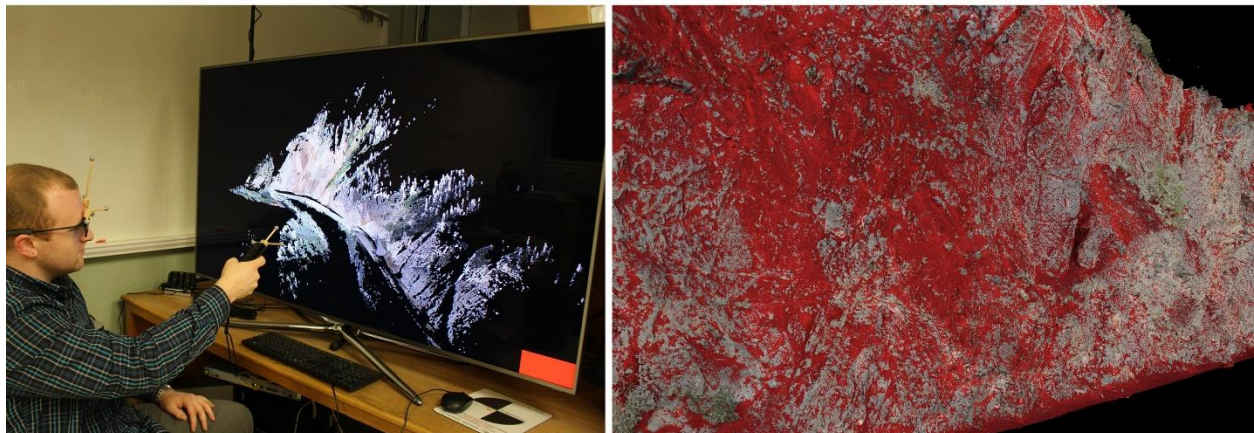
Figure 4-15: Overview image of the GeoMat VR image (left) and screen shot representing simultaneous visualization of the TLS Combo SfM point clouds datasets in GeoMat VR (right). The TLS data is in true color and the Combo SfM data is tinted red.

4.7 DISCUSSION

For study sites RS2 and RS3, the total number of points for the Ground SfM datasets is about three times that of the TLS point clouds. This is not the case for RS1 where the discrepancy may be attributed to differences in image acquisition that stem from both technique and the relatively large vertical and horizontal extent of RS1. Twenty-four additional images were used to create the Ground SfM point cloud for RS3 when compared to RS1. In retrospect, this amount is inadequate given RS1 is ~30 m longer and ~ 50 m higher than RS3. Nevertheless, when attempting to capture a large rock-slope like RS1 with overlapping handheld imagery, it can be difficult to judge if enough images have been acquired with sufficient overlap.

The significant difference in TLS total points between sites RS1 and RS3 is attributed to differences is scanning geometry. Given the larger vertical extent and near vertical orientation of RS1, the TLS instrument was placed further away from the slope than for RS3 to ensure capture of the upper reaches. Increasing the distance between the TLS instrument and the area of interest will increase point spacing and decrease the total quantity of points, assuming the scanning resolution is unchanged.

Having a greater number of points and higher mean point density for the Ground SfM models when compared to the Combo SfM models is counterintuitive given the additional images used to generate the Combo models. When including more images in an SfM reconstruction, one would expect the point quantity to increase. It is likely that this peculiar behavior stems from some automated optimization routine in PhotoScan that omits images and associated points if

other imagery is available for a given region and is thought to be of higher quality. Further investigation is required to validate this possibility.

It is worth noting that the Combo SfM models generated for this study used an average of 217 images per site, compared to an average of 5 TLS scans per site. Assuming a reasonable scanning resolution is chosen, acquisition of 5 TLS scans can be performed in approximately the same amount of time as acquiring a total of 217 images gathered with both UAS and ground-based cameras. In addition, the efficiency of TLS acquisition could be further increased by following direct geo-referencing techniques that eliminate the need for placing GCPs (Olsen et al., 2009; Silvia and Olsen, 2012; Olsen et al., 2015), a technique currently being researched and evaluated (Carbonneau and Dietrich, 2017) but not yet widely available for SfM image acquisition campaigns that need to meet accuracies similar to those achievable with TLS. Mobile laser scanning (MLS) is a possible alternative for surveying these road cuts; however, the point density of MLS data is often significantly lower than that for static TLS data. With regard to road cuts, car/truck-based MLS can suffer from more severe point of view limitations than TLS. Because an MLS system commonly drives along the road, the resulting view of the rock-slope is more restricted when compared to the field of view of a TLS system set up across the road in the opposing road shoulder. In a scenario where the geospatial extent of a study area is significantly larger than that of this study, the efficiency benefits of UAS-based SfM are clear. TLS acquisition over large geospatial extents becomes time-consuming due to the mobilization of equipment from one scanning position to another. A UAS can cover these larger areas relatively quickly and efficiently and is not limited by hard to navigate terrain.

4.7.1 Accuracy Assessment

There is good agreement between both the Ground and Combo SfM surface models and the TLS-derived surfaces. Results indicate accuracies (95% confidence) ranging between $\pm$ 0.044 m and $\pm$ 0.048 m for Ground SfM, $\pm$ 0.041 m and $\pm$ 0.048 m for Combo SfM, and $\pm$ 0.0748 m and $\pm$ 0.112 m for UAS SfM model. Discrepancies between the UAS SfM models and the TLS surfaces follow a pattern in which the intersection of the two planes follow a path roughly parallel to the layout of the GCPs placed along the base of the slope. For RS1, the UAS SfM model is tilted such that 94.1% of the surface lies in front of the TLS surface. This same behavior is observed across the three study sites; however, the percentage of SfM surface that lies in front of the TLS surface changes. The percentages are more balanced in the case of RS2, with 65.3% in front of the TLS surface. The presence of a clear intersection between the UAS SfM and TLS surfaces that appear to be associated with the layout of the GCPs indicates the lack of localized regions of significant deformation in the SfM surface that would affect the relative accuracy of the model. This differencing pattern is indicative of a global geo-referencing error as opposed to localized geometric distortions. The increased error identified in the UAS SfM models is attributed to both the inability to extract all GCPs in the UAS-based imagery, as well as, difficulties in accurately extracting the center of GCPs in the UAS imagery. Accurate extraction of GCPs is made difficult by the presence of pixilation in the imagery resulting from sampling at a large GSD relative to the ground-based imagery. This type of discrepancy pattern can also be attributed to errors in automated focal length calibration for the UAS camera; however, a review of the results indicates consistent focal length determination for the UAS camera across the different SfM models, and agreement with the focal length determined for the DJI Phantom Pro 3 camera used in Carbonneau and Dietrich (2017).

Ground-based SfM can result in high accuracy 3D data; however, it is plagued by numerous occlusions, similar to and often more severe than those seen in TLS data. The TLS outperformed ground-based SfM with respect to completeness even though images were acquired from many more locations/points of view than TLS scan positions (Table 4.1). This effect is likely attributed to the fundamental difference in passive and active remote sensing techniques employed by digital photography and TLS, respectively. In this case, the use of an active light source allowed TLS to capture meaningful geometric data at further distances than the handheld camera used for SfM image acquisition. While the TLS models were able to obtain more sampling directly below thick vegetation for creating a bare-earth surface model, the UAS SfM models demonstrated superior performance in capturing bare-earth behind and around sparser vegetation due to the flexible look angle.

Results of the surface-to-surface and surface-to-points (TS points) accuracy assessments reveal a consistent accuracy ranking of the SfM surface models, except for RS3. For RS1 and RS2, the Ground SfM model was identified as the most accurate based on the mean difference between the surface models and the references, followed by the Combo, and UAS SfM models. The accuracy assessments for RS3 indicate different accuracy rankings; however, this is reasonable given the similarity in accuracy reported for the Ground and Combo SfM models. Results of the rock-slope TS point accuracy assessment indicate higher accuracies when compared to the surface-to-surface assessment, which is a result of the significantly smaller sample size of differencing measurements used. The TS points accuracy evaluation validated the systematic accuracy of the TLS data, confirming TLS data is an appropriate choice for assessing the accuracy of SfM data. Additionally, The TS point accuracy assessment revealed relatively

balanced proportions of TLS data located behind and in front of the TS points, whereas, the SfM models were found to have variable proportions lying behind and in front of the TS reference points.

The Combo SfM models, which include both UAS and ground-based imagery, provide accuracies comparable to ground-based SfM while maintaining the completeness achieved with UAS image acquisition. Using both UAS and ground-based imagery for a SfM reconstruction exploits both the improved access afforded by a UAS and the resolution achieved from a ground-based handheld camera.

4.7.2 Quality Evaluation

4.7.2.1 Point Density

All SfM point clouds were found to have a more uniform point density when compared to TLS datasets, which is beneficial (visually, computationally, and accuracy-wise) in developing surface models with more consistent mesh elements and more uniform vertices for interpolation. Point density hotspots are a common occurrence in TLS point cloud data because scanning occurs at fixed angular increments, resulting in increased point spacing with distance for a given angular increment. Portions of the scanned environment that are close to a given scan position will have a significantly higher point density. Additionally, surfaces that are orthogonal to the laser pulse direction have a higher point density relative to surfaces that are oblique.

4.7.2.2 Completeness

The Combo and UAS SfM surface models are the most complete and Ground SfM models are the least complete, despite the fact that the Ground SfM models also have the greatest number of

total points. This result is attributed to the resolution and GSD of the handheld imagery used to generate the Ground SfM reconstructions. Even though the Combo SfM models utilized more imagery and are more complete, they include fewer points due to the incorporation of lower resolution UAS-based imagery with a larger GSD.

4.7.2.3   Surficial Parameters

The localized increase in surface slope values of ~40° observed for RS1 (Figure 4-10) represents regions of the rock-slope captured well with UAS and poorly captured with TLS and ground-based SfM. The majority of RS1 has a slope of ~60 to 80°; however, localized benches within the rock-slope are laid back at a shallower slope of between 40 and 45°. These localized benches proved difficult to capture with ground-based methods but were captured well with the advantageous point of view afforded by the UAS. Given the smaller vertical extent of RS2 and RS3, the majority of the slope was visible to both aerial and terrestrial capture methods. As such, we observe very similar distributions of surface slope among the SfM and TLS datasets.

The evaluation of SW and LW roughness reveals evidence for the over-smoothing of the UAS and Combo SfM data observed during the qualitative visual inspection. Across all three study sites, we observe a bias of UAS and Combo SfM data towards lower roughness values when compared to TLS, which is likely a result of the lower resolution, higher GSD images contributed by the UAS. The distributions for SW and LW roughness for the Ground SfM datasets correlate well with the TLS distributions; however, as previously discussed, the Ground SfM models are deficient with respect to completeness. In general, the roughness distributions for the SfM surface models are found to align best with the TLS distribution in the right (upper)

half of the distribution. This suggests that SfM is better suited for capturing surfaces with higher roughness as opposed to smoother surfaces.

4.7.2.4 Rock-Slope Monitoring Classification

The discrepancies in RAI classification observed for RS1 are attributed to the large vertical extent of the rock-slope combined with the UAS imagery acquisition strategy. Results of the accuracy and roughness evaluations for RS1, support the unconservative RAI classification discrepancies observed for RS1. The use of a consumer-grade UAS (DJI Phantom 3 Professional) combined with flight limitations associated with the active roadway resulted in the acquisition of imagery of insufficient resolution and GSD. RAI classification of RS1 could be improved by using a higher resolution camera and/or gaining approval to fly closer to the rock-slope. Fewer discrepancies in RAI classification were observed for RS2 and RS3 because of their relatively smaller vertical extents. For RS2 and RS3, the ground-based imagery acquired with a handheld camera captured a majority of the slope, providing the detail necessary to assist the UAS imagery during SfM reconstruction.

4.8 CONCLUSION

Based on results of the accuracy assessment, SfM photogrammetry used in this study is not as accurate as TLS, but is an appropriate tool for rock-slope assessment, assuming the images are tied to a rigorous survey control network by way of GCPs. Use of a survey control network enables accurate scaling and geo-referencing of the resulting 3D point cloud data. While, the equipment needed to perform SfM (e.g., digital camera, UAS) is around two orders of magnitude less expensive than TLS, it is important to consider the significant cost of survey equipment

needed to establish appropriate control. Also, the additional time required to setup the control network is often neglected when SfM acquisition times are discussed.

It is also imperative that an appropriate quantity of images be acquired with adequate overlap – a difficult task to judge in the field when utilizing manual image acquisition methods, as was done in this study. UAS imagery was not acquired using an automated flight plan due to the lack of a flight planning solution that is compatible with vertical features (e.g., a rock-slope) and can be trusted in an obstacle rich environment.

It is undeniable that UAS-based SfM techniques offer superior color imagery and accessibility when compared to traditional TLS techniques. While a key benefit of TLS is its ability to penetrate through gaps in vegetation while the SfM cannot directly penetrate, the flexibility in positioning the UAS from different vantage points can result in improved ground coverage in some vegetation cover.

The Combo SfM models were found to benefit from the improved completeness and accuracy of the UAS and Ground SfM models, respectively. Ground-based imagery also served to capture imagery under rock outcrop overhangs where the UAS used for this study was unable to view. The inability of the UAS to see under overhangs is attributed to the placement of the camera under the body of the aircraft – this effect could be mitigated by using a UAS with a front mounted camera that can rotate to achieve an unobstructed view above the horizontal plane. It may also be possible to omit acquisition of ground-based imagery if a digital image sensor of increased size and resolution is used on the UAS and/or the UAS can fly closer to the rock-slope. For example, the handheld camera used for this study has an image sensor which is approximately twice the size and resolution of the sensor used in the UAS camera. If the

handheld camera was mounted on the UAS, and the UAS was able to maintain a GSD similar to that achieved by ground-based image acquisition, the UAS-based imagery likely would result in a SfM reconstruction of similar accuracy and quality to that of the Ground SfM models.

With regard to monitoring rock-slopes using SfM techniques, caution must be exercised when performing change detection with SfM-derived point clouds and surface models. Artifacts, such as over-smoothing and geometric inconsistencies stemming from differences in image acquisition (e.g., lighting conditions and overlap) have potential to introduce error into detection of small changes. The inherent variability in SfM-derived geometry is demonstrated by the results of the TS point accuracy assessment. For the SfM-derived surface models, the accuracy and proportions of positive and negative discrepancies were found to be quite variable when compared to the consistent TLS results (Table 3). Useful studies have evaluated the performance of SfM with regards to change detection (Lato et al., 2015b; James et al., 2017b); however, further work is needed to improve the threshold of change that can consistently be detected on rock-slopes with SfM techniques.

The accuracies presented in this paper serve as an example of what can be achieved with SfM techniques when following sound surveying methods. Given the variety of environments where these techniques can be employed, as well as, the plethora of available tools/instruments, it is likely that better or worse results could be achieved. The situation is further complicated by the difference in factors that contribute to uncertainty for TLS and SfM techniques. For TLS and total stations, factors such as range, incidence angle, and internal calibration play a major role in the propagation of uncertainty. For SfM, uncertainty is introduced through errors in the determination of exterior and interior orientation of the exposure stations, lens distortion, lighting

conditions, and uncertainty in the automated process of keypoint matching, to name a few. Devising a real-world experiment that accounts for all the possible interactions amongst these factors is improbable. Evaluation of SfM experiments performed with simulated imagery of virtual, computer-generated environments provides an opportunity to further our understanding of how these factors may influence SfM point cloud quality and accuracy (Slocum and Parrish, 2017).

4.9 ACKNOWLEDGEMENTS

4.10 REFERENCES

Abellán, A., Calvet, J., Vilaplana, J.M., and Blanchard, J., 2010. Detection and spatial prediction of rockfalls by means of terrestrial laser scanner monitoring. Geomorphology, 119(3–4): 162–171.

Abellán, A., Jaboyedoff, M., Oppikofer, T., and Vilaplana, J.M., 2009. Detection of millimetric deformation using a terrestrial laser scanner: experiment and application to a rockfall event. Natural Hazards and Earth System Sciences, 9(2): 365–372.

Abellán, A., Oppikofer, T., Jaboyedoff, M., Rosser, N.J., Lim, M., and Lato, M.J., 2014. Terrestrial laser scanning of rock slope instabilities. Earth Surface Processes and Landforms, 39(1): 80–97.

Agisoft., 2017. PhotoScan v1.3.4. http://www.agisoft.com/.

Alba, M., Roncoroni, F., and Scaioni, M., 2009. Application of TLS for change detection in rock faces. 99–104.

Alba, M. and Scaioni, M., 2010. Automatic detection of change and deformation in rock faces by terrestrial laser scanning. Commission V Mid-Term Symposium on Close Range Image Measurement Techniques, 11–16.

Al-Rawabdeh, A., He, F., Moussa, A., El-Sheimy, N., and Habib, A., 2016. Using an Unmanned Aerial Vehicle-Based Digital Imaging System to Derive a 3D Point Cloud for Landslide Scarp Recognition. Remote Sensing, 8(2): 95.

Belowich, M., 2006. Matanuska Coal Field. Field Guide, Anchorage Alaska. Alaska Geological Society.

Bemis, S.P., Micklethwaite, S., Turner, D., et al., 2014. Ground-based and UAV-Based photogrammetry: A multi-scale, high-resolution mapping tool for structural geology and paleoseismology. Journal of Structural Geology, 69, Part A163–178.

Budetta, P. and Nappi, M., 2013. Comparison between qualitative rockfall risk rating systems for a road affected by high traffic intensity. Natural Hazards and Earth System Sciences, 13(6): 1643–1653.

Carbonneau, P.E. and Dietrich, J.T., 2017. Cost-effective non-metric photogrammetry from consumer-grade sUAS: implications for direct georeferencing of structure from motion photogrammetry. Earth Surface Processes and Landforms, 42(3): 473–486.

Chandler, J.H. and Buckley, S., 2016. Structure from motion (SFM) photogrammetry vs terrestrial laser scanning. In: M.B. Carpenter and C.M. Keane, eds., Geoscience Handbook 2016: AGI Data Sheets. American Geosciences Institute.

Dunham, L., Wartman, J., Olsen, M.J., O'Banion, M., and Cunningham, K., 2017. Rockfall Activity Index (RAI): A lidar-derived, morphology-based method for hazard assessment. Engineering Geology, 221: 184–192.

Eltner, A., Kaiser, A., Castillo, C., Rock, G., Neugirg, F., and Abellán, A., 2016. Image-based surface reconstruction in geomorphometry - merits, limits and developments. Earth Surface Dynamics, 4(2): 359–389.

Fassi, F., Fregonese, L., Ackermann, S., and Troia, V.D., 2013. Comparison Between Laser Scanning and Automated 3D Modelling Techniques to Reconstruct Complex and Extensive Cultural Heritage Areas. ISPRS - International Archives of the Photogrammetry, Remote Sensing and Spatial Information Sciences, XL-5-W173–80.

Fernández, T., Pérez, J.L., Cardenal, F.J., et al., 2015. Use of a Light UAV and Photogrammetric Techniques to Study the Evolution of a Landslide in Jaen (Southern Spain). ISPRS - International Archives of the Photogrammetry, Remote Sensing and Spatial Information Sciences, Copernicus GmbH, 241–248.

Fernández, T., Pérez, J.L., Cardenal, J., Gómez, J.M., Colomo, C., and Delgado, J., 2016. Analysis of Landslide Evolution Affecting Olive Groves Using UAV and Photogrammetric Techniques. Remote Sensing, 8(10): 837.

Fonstad, M.A., Dietrich, J.T., Courville, B.C., Jensen, J.L., and Carbonneau, P.E., 2013. Topographic structure from motion: a new development in photogrammetric measurement. Earth Surface Processes and Landforms, 38(4): 421–430.

Gigli, G. and Casagli, N., 2011. Semi-automatic extraction of rock mass structural data from high resolution LIDAR point clouds. International Journal of Rock Mechanics and Mining Sciences, 48(2): 187–198.

Girardeau-Montaut, D., 2017. Cloud Compare v2.9. http://www.danielgm.net/cc/.

Greenwood, W., Zekkos, D., Lynch, J., Bateman, J., Clark, M.K., and Chamlagain, D., 2016. UAV-Based 3-D Characterization of Rock Masses and Rock Slides in Nepal. American Rock Mechanics Association.

Harwin, S. and Lucieer, A., 2012. Assessing the Accuracy of Georeferenced Point Clouds Produced via Multi-View Stereopsis from Unmanned Aerial Vehicle (UAV) Imagery. Remote Sensing, 4(6): 1573–1599.

Hungr, O., Leroueil, S., and Picarelli, L., 2014. The Varnes classification of landslide types, an update. Landslides, 11(2): 167–194.

Jaboyedoff, M., Oppikofer, T., Abellán, A., et al., 2012. Use of LIDAR in landslide investigations: a review. Natural Hazards, 61(1): 5–28.

James, M.R. and Robson, S., 2012. Straightforward reconstruction of 3D surfaces and topography with a camera: Accuracy and geoscience application. Journal of Geophysical Research: Earth Surface, 117(F3): F03017.

James, M.R., Robson, S., d'Oleire-Oltmanns, S., and Niethammer, U., 2017a. Optimising UAV topographic surveys processed with structure-from-motion: Ground control quality, quantity and bundle adjustment. Geomorphology, 280(Supplement C): 51–66.

James, M.R., Robson, S., and Smith, M.W., 2017b. 3-D uncertainty-based topographic change detection with structure-from-motion photogrammetry: precision maps for ground control and directly georeferenced surveys. Earth Surface Processes and Landforms, 42(12): 1769–1788.

Javadnejad, F. and Gillins, D.T., 2016. Unmanned Aircraft Systems-Based Photogrammetry for Ground Movement Monitoring. American Society of Civil Engineers, 1000–1011.

Kashani, I., Wielgosz, P., and Grejner-Brzezinska, D.A., 2004. On the reliability of the VCV Matrix: A case study based on GAMIT and Bernese GPS Software. GPS Solutions, 8(4): 193–199.

Kemeny, J. and Turner, K., 2008. Ground-based LiDAR Rock Slope Mapping and Assessment. Federal Highway Administration.

Kreylos, O. (n.d.). "Low-Cost VR." Oliver Kreylos' Homepage, <http://idav.ucdavis.edu/~okreylos/ResDev/LowCostVR/> (Feb. 19, 2017).

Kromer, R.A., Abellán, A., Hutchinson, D.J., Lato, M., Edwards, T., and Jaboyedoff, M., 2015. A 4D Filtering and Calibration Technique for Small-Scale Point Cloud Change Detection with a Terrestrial Laser Scanner. Remote Sensing, 7(10): 13029–13052.

Lato, M., Hutchinson, J., Diederichs, M., Ball, D., and Harrap, R., 2009. Engineering monitoring of rockfall hazards along transportation corridors: using mobile terrestrial LiDAR. Natural Hazards and Earth System Sciences, 9(3): 935–946.

Lato, M.J., Gauthier, D., and Hutchinson, D.J., 2015a. Rock Slopes Asset Management: Selecting the Optimal Three-Dimensional Remote Sensing Technology. Transportation Research Record: Journal of the Transportation Research Board, 251: 07–14.

Lato, M.J., Hutchinson, D.J., Gauthier, D., Edwards, T., and Ondercin, M., 2015b. Comparison of airborne laser scanning, terrestrial laser scanning, and terrestrial photogrammetry for mapping differential slope change in mountainous terrain. Canadian Geotechnical Journal, 52(2): 129–140.

Leica Geosystems., 2012. Leica Geo Office v8.3. http://leica-geosystems.com/en-us/products/total-stations/software/leica-geo-office.

Leica Geosystems., 2015. Cyclone v9.1. http://hds.leica-geosystems.com/en/Leica-Cyclone_6515.htm.

Lim, M., Petley, D.N., Rosser, N.J., Allison, R.J., Long, A.J., and Pybus, D., 2005. Combined Digital Photogrammetry and Time-of-Flight Laser Scanning for Monitoring Cliff Evolution. The Photogrammetric Record, 20(110): 109–129.

Lim, M., Rosser, N.J., Allison, R.J., and Petley, D.N., 2010. Erosional processes in the hard rock coastal cliffs at Staithes, North Yorkshire. Geomorphology, 114(1–2): 12–21.

Lucieer, A., Jong, S.M. de, and Turner, D., 2014. Mapping landslide displacements using Structure from Motion (SfM) and image correlation of multi-temporal UAV photography. Progress in Physical Geography, 38(1): 97–116.

Manousakis, J., Zekkos, D., Saroglou, F., and Clark, M., 2016. Comparison of UAV-Enabled Photogrammetry-Based 3D Point clouds and Interpolated DSMs of Sloping Terrain for Rockfall Hazard Analysis. ISPRS - International Archives of the Photogrammetry, Remote Sensing and Spatial Information Sciences, Copernicus GmbH, 71–77.

Maptek., 2016. I-Site Studio v6.0. http://www.maptek.com/products/i-site/.

Murphy, R.R., Duncan, B.A., Collins, T., et al., 2016. Use of a Small Unmanned Aerial System for the SR-530 Mudslide Incident near Oso, Washington. Journal of Field Robotics, 33(4): 476–488.

Niethammer, U., James, M.R., Rothmund, S., Travelletti, J., and Joswig, M., 2012. UAV-based remote sensing of the Super-Sauze landslide: Evaluation and results. Engineering Geology, 128: 02–11.

O'Banion, M. (2016). Setup and Calibration of GeoMat VR: A 3D TV based Immersive Virtual Reality Visualization System. Oregon State University. DOI: 10.13140/RG.2.1.1746.9046

Olsen, M., Wartman, J., McAlister, M., et al., 2015. To Fill or Not to Fill: Sensitivity Analysis of the Influence of Resolution and Hole Filling on Point Cloud Surface Modeling and Individual Rockfall Event Detection. Remote Sensing, 7(9): 12103–12134.

Olsen, M.J., 2013. In Situ Change Analysis and Monitoring through Terrestrial Laser Scanning. Journal of Computing in Civil Engineering, 29(2).

Olsen, M.J., Johnstone, E., Driscoll, N., Ashford, S.A., and Kuester, F., 2009. Terrestrial Laser Scanning of Extended Cliff Sections in Dynamic Environments: Parameter Analysis. Journal of Surveying Engineering, 135(4): 161–169.

Ovstedal, O., 2000. Single Processed Independent and Trivial Vectors in Network Analysis. Journal of Surveying Engineering, 126(1): 18–25.

Pantelidis, L., 2009. Rock slope stability assessment through rock mass classification systems. International Journal of Rock Mechanics and Mining Sciences, 46(2): 315–325.

Pierson, L., 2013. Chapter 3: Rockfall Hazard Rating System. In: K. Turner and R.L. Schuster, eds., Rockfall Characterization and Control. Transportation Research Board.

Rabatel, A., Deline, P., Jaillet, S., and Ravanel, L., 2008. Rock falls in high-alpine rock walls quantified by terrestrial lidar measurements: A case study in the Mont Blanc area. Geophysical Research Letters, 35(10).

Rosser, N., Lim, M., Petley, D., Dunning, S., and Allison, R., 2007. Patterns of precursory rockfall prior to slope failure. Journal of Geophysical Research: Earth Surface, 112(F4): F04014.

Rosser, N.J., Petley, D.N., Lim, M., Dunning, S.A., and Allison, R.J., 2005. Terrestrial laser scanning for monitoring the process of hard rock coastal cliff erosion. Quarterly Journal of Engineering Geology and Hydrogeology, 38(4): 363–375.

Silvia, E.P. and Olsen, M.J., 2012. To Level or Not to Level: Laser Scanner Inclination Sensor Stability and Application. Journal of Surveying Engineering, 138(3).

Slocum, R.K. and Parrish, C.E., 2017. Simulated Imagery Rendering Workflow for UAS-Based Photogrammetric 3D Reconstruction Accuracy Assessments. Remote Sensing, 9(4): 396.

Trop, J.M., Cole, R.B., Sunderlin, D., Hults, C., and Todd, E., 2015. Bedrock geology of the Glenn Highway from Anchorage to Sheep Mountain, Alaska. http://archives.datapages.com/data/alaska/data/040/1_akgs0400001.htm.

Turner, D., Lucieer, A., and de Jong, S.M., 2015. Time Series Analysis of Landslide Dynamics Using an Unmanned Aerial Vehicle (UAV). Remote Sensing, 7(2): 1736–1757.

Turner, K. and Jayaprakash, G.P., 2013. Introduction. In: K. Turner and R.L. Schuster, eds., Rockfall Characterization and Control. Transportation Research Board.

Weaver, B., Gillins, D.T., and Dennis, M., 2018. Hybrid Survey Networks: Combining Real-Time and Static GNSS Observations for Optimizing Height Modernization. Journal of Surveying Engineering, 144(1).

Westoby, M.J., Brasington, J., Glasser, N.F., Hambrey, M.J., and Reynolds, J.M., 2012. "Structure-from-Motion" photogrammetry: A low-cost, effective tool for geoscience applications. Geomorphology, 179(Supplement C): 300–314.

Wilkinson, M.W., Jones, R.R., Woods, C.E., et al., 2016. A comparison of terrestrial laser scanning and structure-from-motion photogrammetry as methods for digital outcrop acquisition. Geosphere, 12: 1865–1880.

Manuscript # 4

Interactive Uncertainty Visualization of TLS Point Clouds with GLSL Shaders

Matthew S. O'Banion, Michael J. Olsen, Chris Parrish, and Michael Bailey

5   INTERACTIVE UNCERTAINTY VISUALIZATION OF TLS POINT CLOUDS WITH GLSL SHADERS

5.1   ABSTRACT

An unfortunate absence of application-specific solutions exists for the calculation and subsequent 3D visualization of spatial uncertainty for laser scanner-derived point cloud data. Nevertheless, the highly variable spatial uncertainty of the individual points in a point cloud can adversely affect both qualitative and quantitative observations. Intuitive communication of point cloud uncertainty can facilitate enhanced point cloud observations and measurements and raise awareness regarding the variability of uncertainty. The proposed terrestrial laser scanning (TLS) point cloud uncertainty calculation and visualization methodology utilizes the OpenGL Shader Language (GLSL). GLSL programs (shaders) along with modern computer graphics hardware, are well suited for the parallel processing of large quantities of geometry such as point clouds. Shader-based uncertainty visualization aided in the development of a new beamwidth-derived range error equation that includes laser beam exit diameter, and proved to be a valuable tool for exploring the behavior of range and angular-based error sources. This framework was tested on four unique datasets ranging from simple datasets to intuitively verify the capabilities of the visualization algorithm to complex scenes illustrating the potential of such visualizations.

5.2   INTRODUCTION

Laser scanning, also known as lidar, is being used for an increasing number of scientific and engineering focused applications (e.g., Williams et al. 2013; Telling et al. 2017). For many of these applications, the spatially-varying uncertainty of the resulting 3D point cloud can have a

significant impact on the validity of derived products as well as observations and findings. Unfortunately, currently available terrestrial laser scanning (TLS) point cloud visualization and processing software does not provide a solution for calculating and visualizing such uncertainty. It is of the authors' opinion that visualizing the per-point uncertainty of a point cloud is as valuable as visualizing fundamental TLS attributes such as laser pulse return intensity and camera-derived color when making observations and/or measurements in point cloud data. A major shortcoming in the current TLS, not to mention the more mature airborne laser scanning (ALS), industry, is that such information is not available to end users. As a result, end users can be misguided as to the quality of measurements derived from the point cloud in areas that are poorly captured (e.g., distant range, oblique data). This problem is further compounded when multiple scans are combined together, rendering it difficult to distinguish which points are of higher quality than others.

Within the broad field of geospatial data uncertainty, the past few decades of research have focused on typologies, conceptual models, and the computation of uncertainty (Mason et al. 2017). Recent work in this area has begun to shift towards visualization approaches that successfully communicate the various aspects of geospatial uncertainty (Mason et al. 2017). Nevertheless, the overwhelming majority of geospatial uncertainty visualization research has focused on 2D, map-based solutions, and 3D representations of uncertainty are rarely considered (Dübel et al. 2017). Following a similar trend, existing literature regarding point cloud uncertainty has focused on methods for modeling and calculating per-point uncertainty. Initially, work investigating this subject has focused on airborne laser scanning (ALS) systems (Baltsavias 1999; Morin 2002; Goulden and Hopkinson 2014) followed by research that addresses terrestrial

and kinematic (mobile) laser scanning (Lichti et al. 2005; Glennie 2007; Schaer et al. 2007; Hodge 2010; Cuartero et al. 2010; Soudarissanane et al. 2011; Hartzell et al. 2015; Fan et al. 2015; Chen et al. 2016; Mezian et al. 2016; Barbarella et al. 2017). Nevertheless, these works have concentrated on the determination of point cloud uncertainty estimates and tend to use limited visualization techniques when it comes to communicating the results.

Building upon these well-developed methods for point cloud uncertainty determination, this work explores new approaches to improve the utilization and communication of this information. One of the largest misconceptions with respect to laser scanning data is that all points are of equal quality and accuracy. This misconception is indirectly perpetuated by current visualization schemes where typically every point is rendered as a vertex of the same size, excluding any size differences that may be introduced due to perspective rendering. This mode of display is fundamentally incorrect if we consider just one source of uncertainty, laser beam divergence and the resulting change in laser footprint diameter with increased range. It is worth noting that a few commercially available software products provide the ability to visualize the relative laser footprint size of point as a potential setting, but most users typically use the default setting of a constant point size. When considering other error sources, the spatial uncertainty for each point increases, meaning that the true 3D position of a given point is likely located somewhere within an uncertainty-derived ellipsoid that is probably larger than the rendered vertex we are accustomed to. With that said, visualizing a point cloud with individual vertices is more computationally efficient than visualizing each point as a 3D volume that represents the region from which a laser pulse may have originated. As such, we must rely on intrinsic or extrinsic

techniques (Dübel et al. 2017) for communicating the level of spatial uncertainty while also visualizing the point cloud in an efficient manner.

In addition to aspects of visualization, it is also important to consider how the per-point uncertainty calculations are performed. Traditional methods for performing uncertainty propagation are assumed to rely on point cloud preprocessing that records the results as additional point attributes that can later be used for visualization. This results in an increased point cloud file size and can dramatically decrease the performance of point cloud visualization software due to the increase in required memory resources and data transfer.

This paper presents a novel, OpenGL Shader Language (GLSL)-based solution for both calculation and visualization of TLS point cloud uncertainty during active 3D visualization. GLSL shaders take advantage of modern graphics hardware, which are well suited for parallel processing of large quantities of geometry such as required in this application. This work focuses on uncertainty propagation and visualization for terrestrial laser scanning (TLS) point cloud data; however, the proposed out-of-core calculation and visualization techniques can be adapted for any 3D point cloud data granted *a priori* knowledge of error sources is available. Examples include, ALS, mobile laser scanning (MLS), and photogrammetric-derived 3D point clouds, to name a few. In addition to providing a solution for intuitively communicating uncertainty of TLS point cloud data, this paper explores the contribution of select error parameters and components, and validates the capabilities of the visualization tool using different TLS datasets. Lastly, the influence of laser beam exit diameter on TLS point cloud uncertainty is discussed.

5.3 METHODOLOGY

5.3.1 TLS Point Cloud Data Sources

Four TLS point cloud datasets (Figure 5-1) were used for development and demonstration of the proposed point cloud uncertainty visualization tool. Table 5.1 provides basic details for the TLS datasets. Scans A, B, and C were collected with a Leica Geosystems ScanStation P40 TLS instrument and Scan D was collected with a Riegl VZ-400 scanner. Scan A was performed in a controlled indoor environment containing the following geometric objects: two spherical objects (exercise balls), two cones (road safety cones), a small cylinder (metal cylindrical canister), and an angled plane (cork board resting on a table). The standard geometric objects facilitate efficient visual validation of the TLS uncertainty propagation due to the relatively intuitive error patterns they generate. Scan B, collected in Reser Stadium on the Oregon State University campus, is an example of a larger, outdoor scene with a variety of well-defined surfaces. Scan B was acquired near the center of the football field and provides examples of long and short-range returns as well as an extensive area (football field) that results in relatively large incidence angles. Scan C was performed near the entrance of a seismically-damaged train tunnel culvert in Kaikoura, New Zealand following the 2016 M_w 7.8 Kaikoura earthquake. In this dataset a variety of incidence angles are captured over a relatively short range. Lastly, Scan D was collected at Watershed 1 of the H.J. Andrews Experimental Forest near Blue River, Oregon. Scan D represents a naturally complex, dense forest environment that includes various types of ground vegetation, stream rocks, manmade objects (wood footbridge and storage shed), and numerous trees.

Table 5.1: Details of the TLS scans used as test cases for the uncertainty visualization.

Scan	TLS Instrument	Number of Pts.	Angular Resolution (°)	Approximate Min Range (m)	Approximate Max Range (m)
Scan A	P40	1,704,724	0.02	4	6
Scan B	P40	24,374,891	0.01	2	150
Scan C	P40	22,557,313	0.02	2	125
Scan D	VZ-400	40,912,731	0.03	2	50
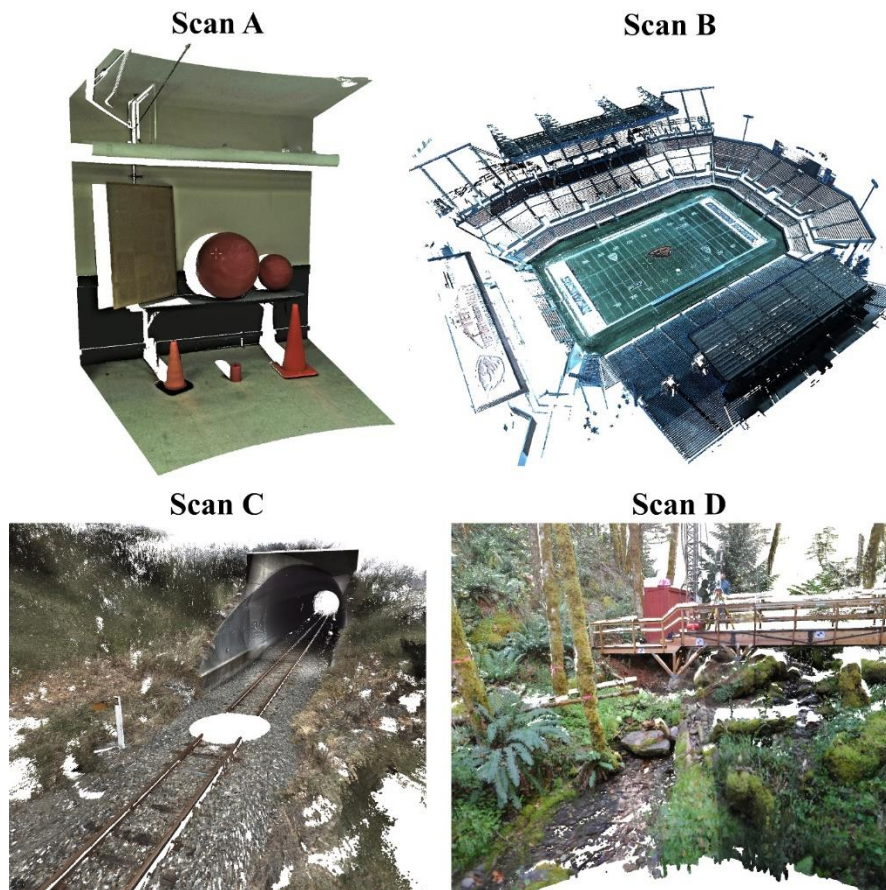
Figure 5-1: Screenshots of the TLS point cloud datasets used for development and demonstration of the uncertainty visualization tool. (A) Simple scene with basic geometric objects, (B) Football stadium with a variety of well-defined features at different orientations, (C) Train Culvert in New Zealand, and (D) Complex natural environment in the HJ Andrews Experimental Forest.

5.3.2   Point Cloud Processing

Processing the TLS data for this study included: importing the raw data for Scans A, B, and C to Leica's *Cyclone* software (Leica Geosystems 2015), uploading Scan D to Riegl's *RiScan Pro* software (Riegl 2016), and coloring the points with RGB values from the co-acquired imagery. All scans were leveled based on on-board inclination readings logged during scanning (Silvia and Olsen 2012). The ScanStation P40 utilizes a level compensator to correct individual scanlines during acquisition. In contrast, point cloud data from a VZ-400 is leveled using a rigid-body transformation that is based on an average inclination calculated from a 1Hz log of inclination values captured dynamically throughout the scan. Point cloud registration was not performed since only single scans were used for this proof of concept study.

The leveled TLS data was exported as E57 files (Huber 2011) to preserve the acquisition structure of the data and brought into *CloudCompare* v. 2.9 (Girardeau-Montaut 2017) for the calculation of normals using the *compute normal* tool. Normal vectors were calculated using a planar local surface model and a neighborhood with a radius of 2 cm. One limitation of this normal calculation method is, when the distance between neighboring points exceeds 2 cm, a normal vector cannot be calculated. Normal vectors are necessary for the chosen uncertainty propagation method (further discussed in Section 2.3). The point cloud datasets were exported from *CloudCompare* as PLY files (Turk 1998). The PLY file format was chosen because of its ability to store normal vector components for each point and its compatibility with the 3D visualization software used for this study, *Displaz v*. 0.4.0 (Foster 2017).

Displaz is an open-source 3D point cloud viewer that supports the use of GLSL vertex and fragment shaders. *Displaz* allows the modification of and re-compilation of shaders during

visualization of the point cloud data. This functionality enabled for efficient prototyping of an uncertainty calculation and visualization shader, as well as, interactive adjustment of the visualization based on manipulation of uncertainty propagation calculations and error parameters.

5.3.3   Point Cloud Uncertainty Propagation

Because not all TLS instrument details and raw data are usually provided by manufacturers, assumptions must be made prior to performing uncertainty propagation. For example, the actual observations in terms of range, horizontal angle, and vertical angle are not directly available, but must be computed inversely from coordinates derived from the geolocation equation (equation 4-1), which is greatly simplified from reality given the wide range of calibration corrections applied internally with many systems.

$$\begin{bmatrix} X \\ Y \\ Z \end{bmatrix} = \begin{bmatrix} \rho\cos\theta\cos\psi \\ \rho\cos\theta\sin\psi \\ \rho\sin\theta \end{bmatrix} \tag{4-1}$$

where, ρ = range, θ = vertical angle, ψ = horizontal angle, and *XYZ* are the resulting Cartesian coordinates of the individual points. Vertical angle is defined as 0° when aligned with the horizontal plane, 90° when aligned with the Z-axis and negative (-) when below the horizontal plane. Horizontal angle is defined as 0° along the positive (+) X-axis and increase clockwise to 360°. This set of equations is commonly used in the literature; however, it should be noted that the actual geolocation equation for a given TLS instrument is likely to have far more instrument specific variables. An example of additional variables could be systematic corrections that account for the internal temperature of hardware components. Amongst different manufacturers,

there are also unknowns associated with how discrete laser pulse returns or full waveform data are processed to calculate a range. All of these details are included in manufactures' sensor models; however, they are commonly proprietary and are not available to end users. Not having access to these models is a major limiting factor when developing uncertainty models. For uncertainty analyses based on the assumed geolocation equation, ρ, θ, and ψ are required for each point in the point cloud. For the unregistered and non-georeferenced single scans used in this study, the scanner origin is simply (0,0,0).

An additional assumption was made with regard to the instrument accuracy specifications published by the manufacturer. The published values for the ScanStation P40 (Leica Geosystems 2016) and VZ-400 (Riegl 2017) TLS instruments are provided in Table 5.2. Because we do not know the exact calibration and accuracy determination procedures followed by a given manufacturer, we assume that the published accuracies do not take into consideration laser beam divergence and the interaction of the laser beam footprint with scanned objects and the terrain. Note that a key benefit of using the proposed uncertainty calculation and visualization solution is the ability to vary the required accuracy parameters during interactive visualization of the results, enabling a user to perform efficient visual sensitivity evaluations of the chosen error sources rather than simply relying on manufacturer specifications.

Table 5.2: Summary of published accuracy specifications for the ScanStation P40 (Leica Geosystems 2016) and VZ-400 (Riegl 2017) TLS instruments.

TLS Instrument	Range σ (m)	Variable Range Error (ppm)	Horizontal Angle σ (°)	Vertical Angle σ (°)	Beam Divergence (mrad)	Beam Exit Diameter (m)	Inclination σ (°)
P40	0.0012	10	0.0022	0.0022	0.23	0.0035	0.00042
VZ-400	0.0050	N/A	0.0005*	0.0005*	0.30	0.0065**	0.00800

* Angular resolution reported by Riegl
** Beam exit diameter reported by www.geo-matching.com

3D uncertainty for each point in the TLS datasets was calculated based on the detailed methodology presented in Hartzell et al. (2015). Random error sources used in the uncertainty propagation include: laser ranging error (σ_ρ), horizontal (σ_ψ) and vertical (σ_θ) angle encoding error, inclination sensor error (σ_i), and laser beamwidth-derived errors ($\sigma_{BWangle}$ and $\sigma_{BWrange}$). Note that systematic errors were not considered as part of the uncertainty propagation. For example, systematic errors originating from non-standard atmospheric conditions were assumed to be accounted for during TLS data acquisition. Accuracies at one standard deviation (1-σ) confidence for range measurements, angular encoders, and inclination sensors as well as the laser beam divergence were gathered from instrument specifications published by the scanner manufacturer (Table 5.2).

The beam divergence of a laser beam results in the increase of beamwidth with increased distance/range. When using a reflected laser beam to measure a specific location in a scanned scene, the non-zero beamwidth contributes an angular and range-based uncertainty to the 3D coordinate of a given point. These uncertainties originate from the assumption that the location of a given range measurement is from the centerline of the laser beam; when in fact, it could have originated from anywhere in the projected beam footprint (Lichti et al. 2005). The equation

for calculating beamwidth angular uncertainty ($\sigma_{BWangle}$) was used directly from Hartzell et al. (2015) (equation 4-2). Beamwidth contributes to range uncertainty when the incidence angle of the laser beam is nonorthogonal (e.g., Baltsavias 1999; Laefer et al. 2009; Olsen et al. 2011; Hartzell et al. 2015). Oblique incidence angles result in an elongation of the laser beam footprint, which adds uncertainty to the range determination assigned to the centerline of the laser beam. For beamwidth range uncertainty ($\sigma_{BWrange}$), the equation from Hartzell et al. (2015) was modified to include laser beam exit diameter (equation 4-3). It is common for laser beam exit diameter to be omitted from beamwidth calculations for ALS applications because it is commonly negligible given the large ranges required for ALS. For TLS applications, ranges tend to be substantially shorter; hence, beam exit diameter can have a larger impact. For instance, when considering the 3.5 mm exit diameter and 0.23 mrad beam divergence specified for the ScanStation P40, choosing to not include beam exit diameter when calculating beamwidth at a given range is similar to calculating beamwidth with a range reduced by 15 m. In other words, it would take a 15 m range to generate a beamwidth of 3.5 mm assuming a 0.23 mrad beam divergence and an exit diameter equal to zero. The plot in Figure 5-2. further demonstrates the discrepancy in laser beam footprint size when not including the beam exit diameter in the calculation.
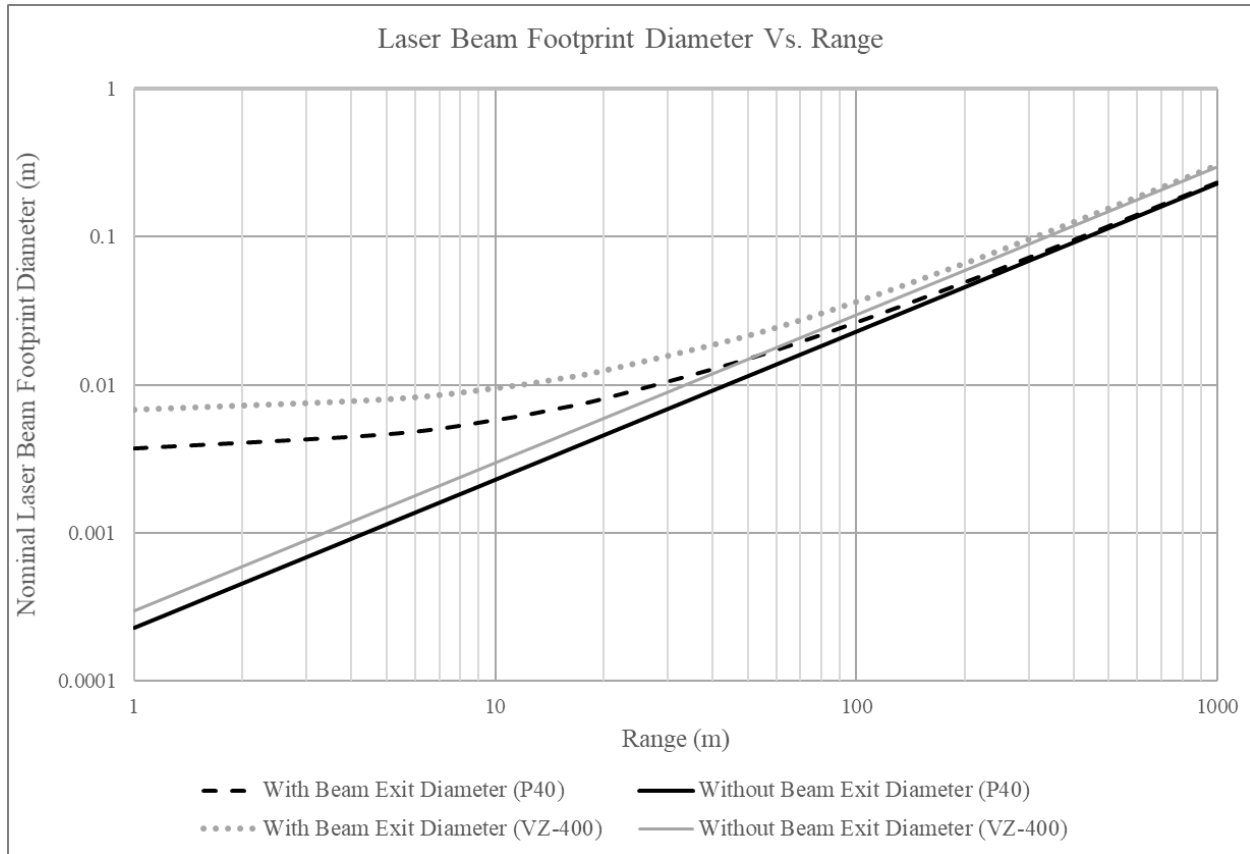
Figure 5-2: A plot demonstrating how the nominal laser beam footprint diameter varies when including and ignoring laser beam exit diameter. Laser beam values indicative of those specified for the ScanStation P40 and VZ-400 TLS instruments (Table 5.2) were used.

Based on Figure 5-2, the impact of laser beam exit diameter on laser footprint diameter becomes somewhat negligible at ranges greater than ~100 m for the ScanStation P40 and ~ 200 m for the VZ-400. This supports the common practice of neglecting beam exit diameter for ALS applications; however, many measurements collected with TLS instruments, especially those collected for civil engineering applications, are generally focused within the 1 to 100 m window where the beam exit diameter can significantly contribute to laser beam footprint size and therefore positional uncertainty of the measurements. These results are based on beam exit diameter beam and beam divergence values for both scanners (Table 5.2). If an instrument with

differing laser characteristics is used, the range cutoff where laser beam exit diameter becomes negligible would change.

$$\sigma_{BWangle} = \frac{\gamma}{4} \tag{4-2}$$

where, γ = beam divergence (radians).

$$\sigma_{BWrange} = \frac{1}{4}(d + \rho * \gamma) \cdot tan(\alpha) \tag{4-3}$$

where, d = laser beam exit diameter, and α = is the incidence angle. The beamwidth range uncertainty equation considers the beam footprint and its interaction with the scanned geometry, which is approximated by the computed normal vectors. Multiplying the beamwidth portion of equation 4-3 by (1/4) results in an uncertainty estimation that uses one-quarter of both the exit diameter and beam divergence and is consistent with the $\sigma_{BWangle}$ equation. Differences in 3D error resulting from incorporating beam exit diameter are presented and discussed in Section 3.1. Angular and range-based standard deviations stemming from beamwidth were added to the published specifications for angular and range accuracies in quadrature (equations 4-4, 4-5, and 4-6). Also included in the quadrature sum is the dual-axis inclination sensor accuracy. Adding the published inclination sensor accuracies to both the horizontal and vertical angle components represents a conservative strategy; however, it is more computationally efficient than propagating uncertainty through a rotational transformation, and the difference is expected to be negligible given the small magnitude of these errors relative to the other error sources.

$$\sigma_{total\,\rho} = \sqrt{\sigma_{\rho}^2 + \sigma_{BWrange}^2} \tag{4-4}$$

$$\sigma_{total\,\psi} = \sqrt{\sigma_{\psi}^2 + \sigma_{BWangle}^2 + \sigma_i^2} \tag{4-5}$$

$$\sigma_{total\,\theta} = \sqrt{\sigma_{\theta}^2 + \sigma_{BWangle}^2 + \sigma_i^2} \tag{4-6}$$

The resulting standard deviations were squared to generate variances and the uncertainty propagation was performed using a mathematical model according to the general law of propagation of variance (GLOPOV) (e.g., Ghilani 2010).

A simplified approach was implemented for calculating the 3D, horizontal, and vertical uncertainty from the resulting covariance matrix generated for each point in the point cloud data. The variances (σ_x^2, σ_y^2, σ_z^2) found along the diagonal of the covariance matrix were converted to standard deviations and used to generate the required uncertainties. For 3D and horizontal uncertainty, the root of sum of squares of (σ_x, σ_y, σ_z), and (σ_x, σ_y) were used, respectively. Magnitudes of uncertainty were calculated using the rectangular bounding box (standard error rectangle) of a given error ellipse (2D) or ellipsoid (3D) rather than the actual semi-axes. Given that the vector extending from the center to the corner of any standard error rectangle or rectangular box will always be greater than the semi-major axis of the associated error ellipse, this simplified approach results in a slightly conservative uncertainty value. The primary reason for choosing this method is to reduce the amount of computations necessary during visualization. Performing the eigenvalue decomposition that is required to identify the semi-axes and orientation of a given error ellipse are arguably not needed for the proposed method of point

cloud uncertainty communication. Ultimately, the chosen strategy for visualization of point cloud uncertainty relies on an approximated magnitude of error at each point, not on the orientation and exact dimensions of a computed error ellipsoid.

Following computation of 3D, horizontal, and vertical uncertainty, the resulting values were all scaled to 1-σ (68.3%) confidence following an established method for assigning confidence levels to a covariance based uncertainty (Ghilani 2010). 3D uncertainty values were scaled by 1.8786, and horizontal (2D) uncertainty values were scaled by 1.5158. Vertical (1D) uncertainty values were not scaled as they are assumed to already represent a 1-σ level of confidence. It is important to note that these scale factors are meant to be applied to the semi-major axis of an error ellipse or ellipsoid; however, as previously discussed, the scale factors have been applied to our standard error rectangle/ rectangular box-based estimates of uncertainty. This is in favor of prioritizing interactive visualization and is expected to be only slightly conservative.

5.3.4   GLSL Shader-based Visualization Tool

GLSL shaders represent the programmable portion of the OpenGL graphics pipeline. The two original shaders introduced in GLSL v1.10 in 2004 are the vertex and fragment shaders (Kessenich et al. 2004). Since then, additional GLSL shaders types have been created including: tessellation, geometry, and compute shaders (Kessenich et al. 2017). A vertex shader operates on vertices entering the graphic pipeline; while a fragment shader operates on the individual fragments (pixels) leaving the graphics pipeline. A vertex shader allows access to incoming vertices and their associated data, which can be used to perform vertex computations. When using a vertex shader, vertex computations are performed on model space coordinates prior to all projections and clipping that occurs later in the graphics pipeline (Bailey and Cunningham

2012). The primary purpose of the fragment shader is to determine the final color of the individual fragments (pixels) in each rendered frame displayed on the screen. It is important to note that all vertex-based geometry and color information is interpolated by the rasterizer prior to arriving at the fragment shader (Bailey and Cunningham 2012). As for the additional shaders, tessellation shaders operate on a patch of incoming vertices and are well suited for dynamic level of detail visualization, geometry shaders allow for the manipulation and creation of geometric primitives within the graphics pipeline, and compute shaders provide access to GPU parallel processing similar to OpenCL. The proposed uncertainty visualization framework relies solely on customized vertex and fragment shaders. Uncertainty propagation was performed in the vertex shader to ensure access to the original geometric coordinates as opposed to any interpolated and/or transformed geometry occurring further on in the graphics pipeline. The GLOPOV uncertainty propagation was performed in the vertex shader using built-in support for matrix operations. GLSL and graphics hardware, in general, are well suited to perform matrix operations because of the demand for large quantities of rapid coordinate transformations in interactive computer graphics.

The developed vertex shader requires the following inputs for each point cloud vertex: a position vector (X,Y,Z), a normal vector (N_x,N_y,N_z), a color vector (R,G,B), and an intensity scalar value (ranging from 0-1). With these inputs, the vertex shader supports the following visualization modes: Color, Intensity, Color/Int. Blend, and Uncertainty. Examples of these visualization modes are presented in Figure 5-3.
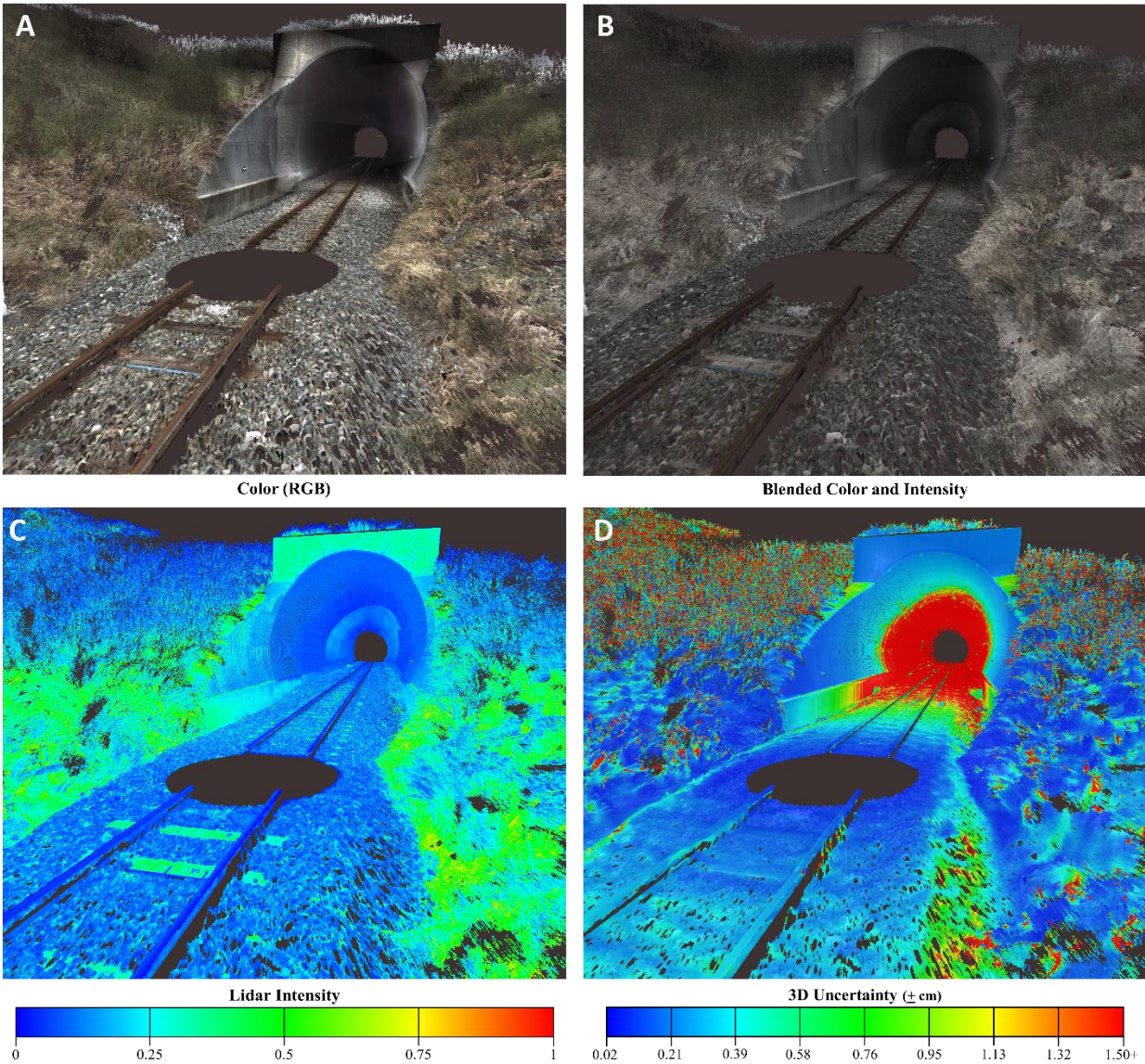
Figure 5-3: Scan C displayed using the four primary visualization modes: Color (A), Blended Color and Intensity (B), Intensity (C), and 3D uncertainty (D).

The color (RGB) and intensity modes simply color the point cloud data based on available camera-derived RGB values (previously mapped to the point cloud) or based on intensity values assigned to a Hue-Saturation-Value (HSV)-derived rainbow color ramp. The blended color and intensity mode allows the user to blend the RGB and Intensity color schemes for enhanced visualization of the point cloud data. The user is able to control the amount of blending using a

value slider embedded in the Graphic User Interface (GUI). The ability to blend the intensity values (generated with active remote sensing) with camera-derived color can reveal details not visible when using the RGB values alone. Because digital photography is a passive remote sensing technique, it is common for regions of co-acquired camera imagery to be under or over-exposed, resulting in regions of an RGB-colored point cloud that can be difficult to interpret. The benefit of blending intensity values with the camera imagery colors is depicted in Figure 5-3. Close examination of the color (RGB) image in Figure 5-3 reveals photographic artifacts on the upper concrete face of the tunnel entrance, as well as a lack of detail in the tunnel due to under exposed imagery. The Blended Color and Intensity example in Figure 5-3 demonstrates how the intensity helps add uniformity to the RGB colors and enhances the visible detail. For best results, the mapped RGB and intensity values need to be well-calibrated so a significant offset is not observed when blending.

In addition, a group of troubleshooting visualization modes were included that facilitate the display of calculated parameters that are critical to uncertainty propagation: incidence angle, horizontal angle, vertical angle, and range. Examples of the troubleshooting visualization modes are included in Figure 5-4. The troubleshooting visualization modes allow the user to visually validate that the key components of the uncertainty propagation for a given point cloud dataset appear correct. The incidence angle mode helps a user to visualize how incidence angle varies across the dataset using a color scheme that ranges from green to red (low to high incidence angle). For the purpose of better understanding how a selected scanner origin affects the incidence angle, the user can use the *ScannerX, ScannerY*, and *ScannerZ* GUI sliders to artificially move the scanner origin and immediately see the changes in incidence angle within

the data. Figure 5-5 includes a screenshot of the *Displaz* software environment and the custom GUI. Note, however, a major limitation of this simulation is that the scan data was acquired from the original scanner origin and the point cloud data from a different location would not be the same due to differing fields of view and object occlusions. In an effort to make the simulation more realistic, if the simulated scan position is moved behind a surface that was originally captured, the relevant points will disappear based on the interaction between the new scanner position and the previously established normal vectors. An example of this functionality is provided in Figure 5-6. For the horizontal angle visualization, the HSV color ramp should span the range of 0° to 360°, where 0° is aligned with the positive x axis. For a ScanStation P40 scanner, the vertical angle ranges from -55° to 90° (aligned with + Z-axis) for a total of 145°. Range is visualized with a blue to red (longer range) color ramp.
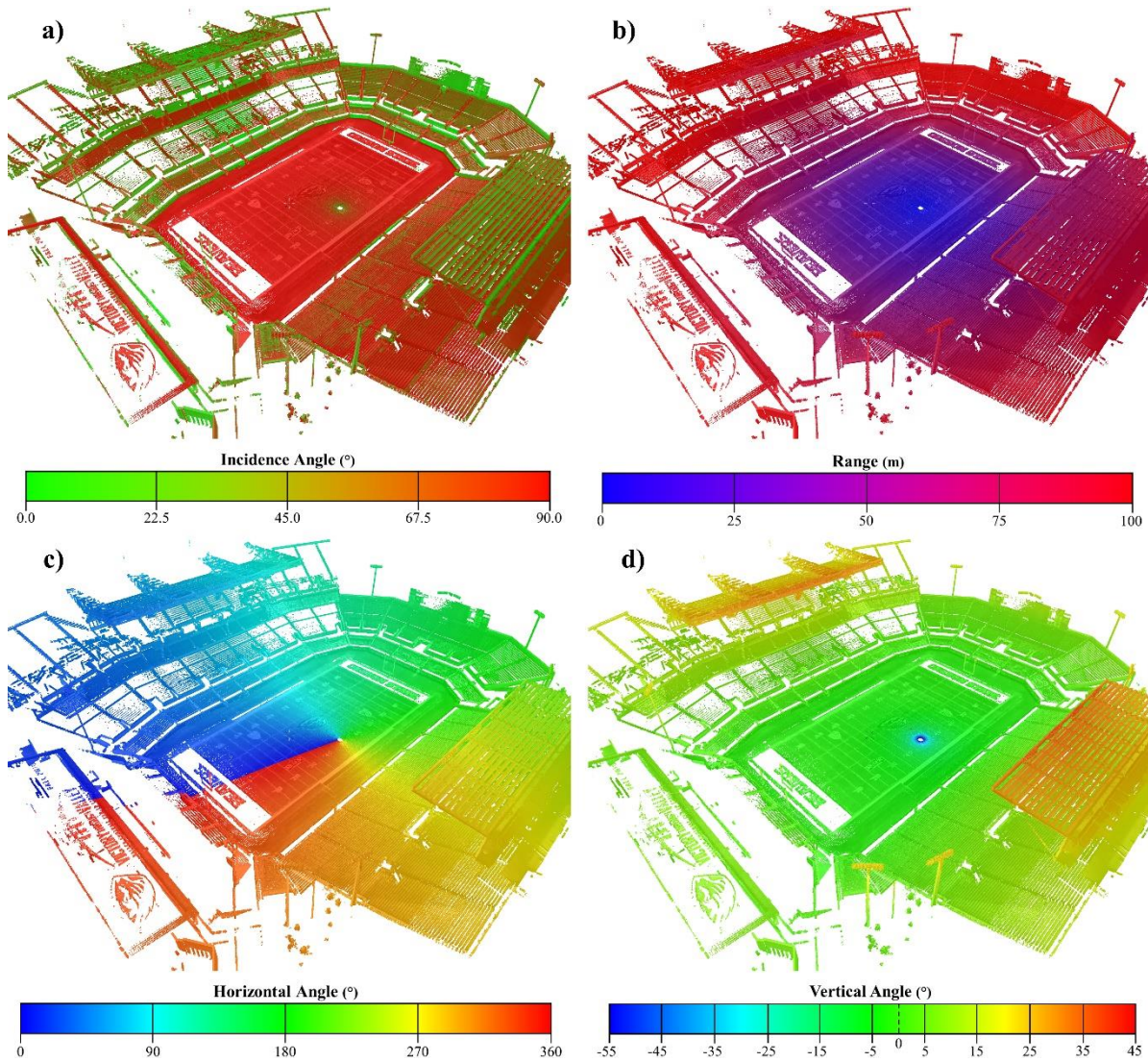
Figure 5-4: Visualizing Scan B using the four troubleshooting visualization modes: (a) Incidence Angle, (b) Range, (c) Horizontal Angle, and (d) Vertical Angle.
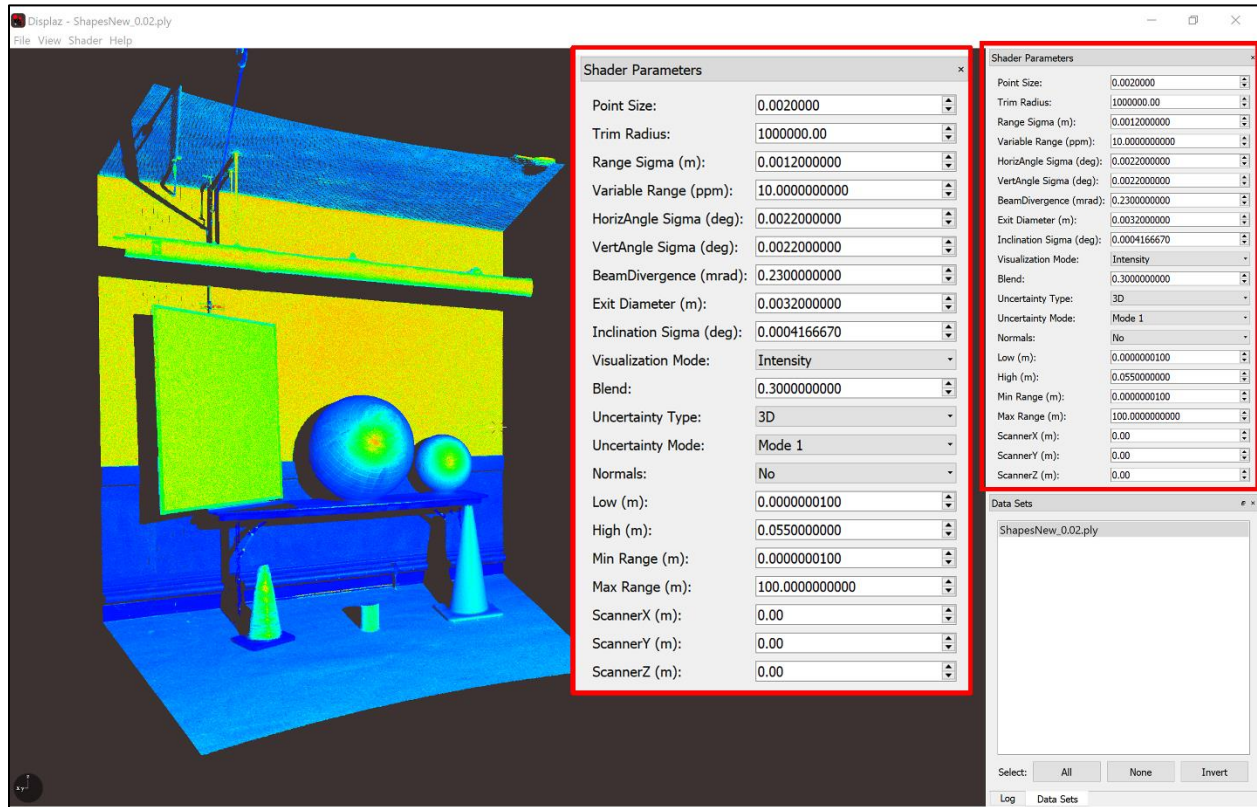
Figure 5-5: Screenshot of *Displaz* user environment and the custom GUI.
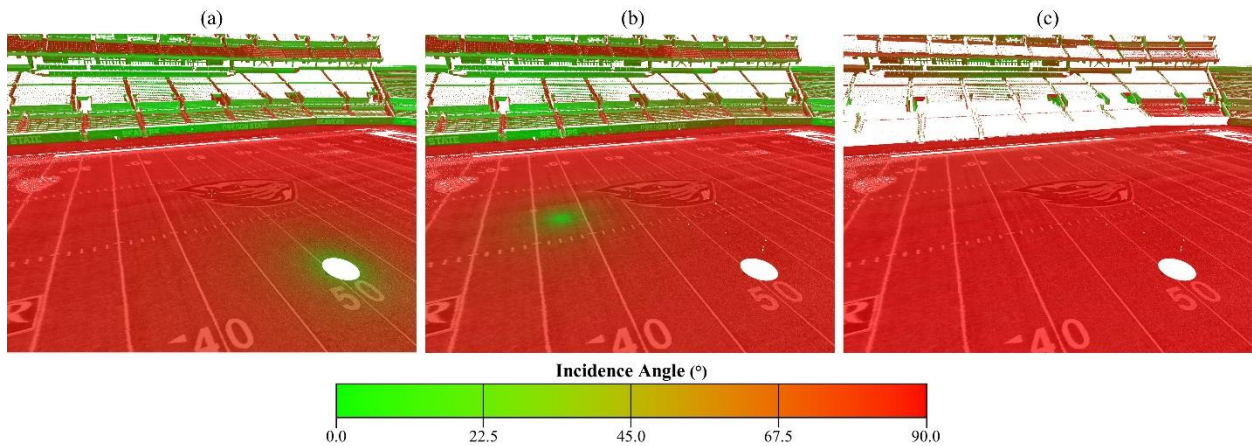
Figure 5-6: Scan B colored based on incidence angle using the original scanner origin (a), an offset scanner origin of 15 m in X and -8 m in Y (b), and a scanner origin that was moved beyond the outer wall, causing some of the data to disappear (c).

The uncertainty visualization mode includes three settings and two types of visualization. A user can choose to visualize 3D, Horizontal, or Vertical uncertainty using a HSV-derived rainbow color ramp blended with the RGB values (Mode 1), or by removing points from the visualization that that exceed a user specified (*High* GUI slider) uncertainty threshold (Mode 2). A side-by-side example of the two uncertainty visualization options are presented in Figure 5-7. Blending the color-coded uncertainty with the RGB color values allows visualization of uncertainty along with the visual cues afforded by the camera imagery (Figure 5-8). For similar effect, uncertainty could also be blended with intensity; however, it is recommended that a radiometric correction methodology (Kashani et al. 2015) be adopted to minimize the amount erroneous variation amongst the intensity values. To minimize the level of color manipulation occurring when the HSV-derived uncertainty colors are mixed with the RGB values, the RGB color is converted to grayscale, resulting in a manipulation when blending that is similar to varying the "Value" in a HSV color space. Alternatively, blending the original RGB values with the HSV uncertainty colors would erroneously change the "Hue" value.
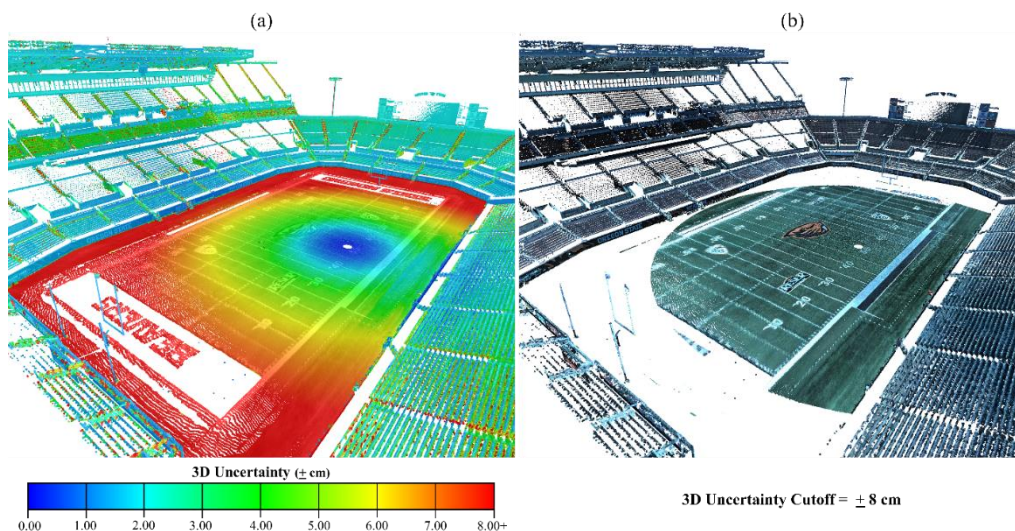
Figure 5-7: Examples of Mode 1 (a) and Mode 2 (b) point cloud uncertainty visualization.
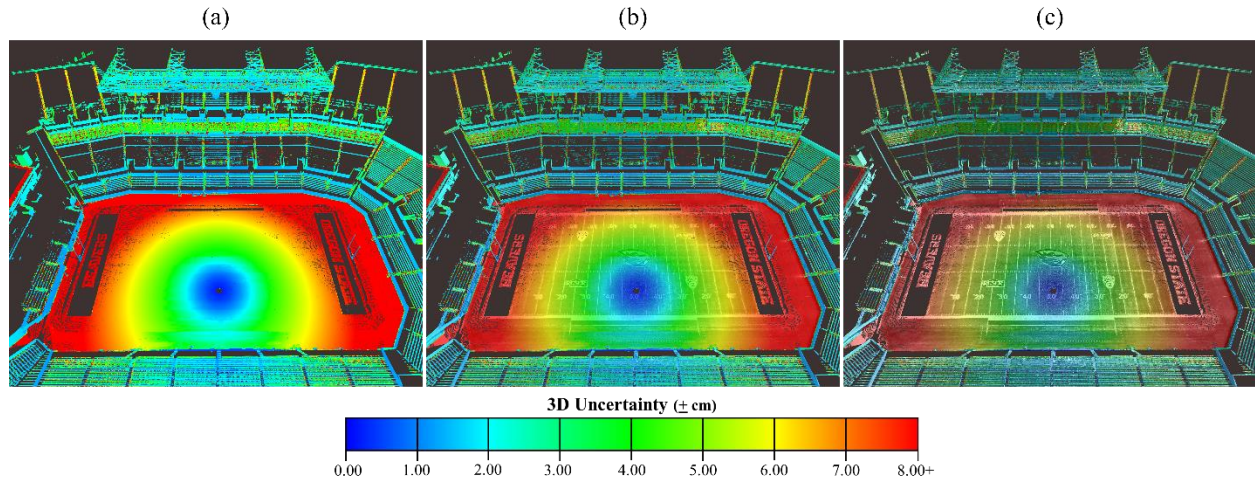
Figure 5-8: Mode 1 uncertainty visualization with 0% (a), 30% (b), and 60% (c) blending of RGB values with uncertainty color ramp.

The developed GUI in *Displaz,* includes value boxes for entering the following accuracy estimates commonly specified by laser scanner manufacturers: range σ (m), variable range (ppm), horizontal angle σ (°), vertical angle σ (°), beam divergence (mrad), beam exit diameter (m), and inclination sensor or level bubble σ (°) (Figure 5-5). To ensure compatibility with the chosen uncertainty propagation method, 1-σ accuracy estimates should be used and the beam divergence should be defined based on the location of the laser beam power distribution where power falls to the fraction $1/e^2$. This is a common way beam divergence is reported in instrument specifications, and it represents a 2-σ accuracy (Hartzell et al. 2015) assuming a Gaussian beam. Through the functionality of *Displaz* and the nature of GLSL shaders, these parameters can be adjusted on-the-fly without having to restart or recompile the graphics program. The uncertainty visualization model also supports the ability to observe immediate changes when manipulating the scanner origin with the previously mentioned *ScannerX, ScannerY, and ScannerZ* GUI sliders. When displaying point cloud data with an uncertainty or range-based color scheme, the

Low/High and Min Range/Max Range GUI sliders are used to the dynamically tune the color ramp to the range of values being displayed.

Lastly, all visualization modes are compatible with displaying the precomputed normal vectors as individual 3D vectors emanating from each point. One way to achieve this effect is through use of a geometry shader; however, since *Displaz* currently does not support geometry shaders, it was implemented in a fragment shader (Foster 2017). Figure 5-9 shows an incidence angle visualization of Scan C with normal vectors turned on. In this example, a sparse region of the point cloud was chosen so the individual normal vectors are clearer in the static screenshot image.
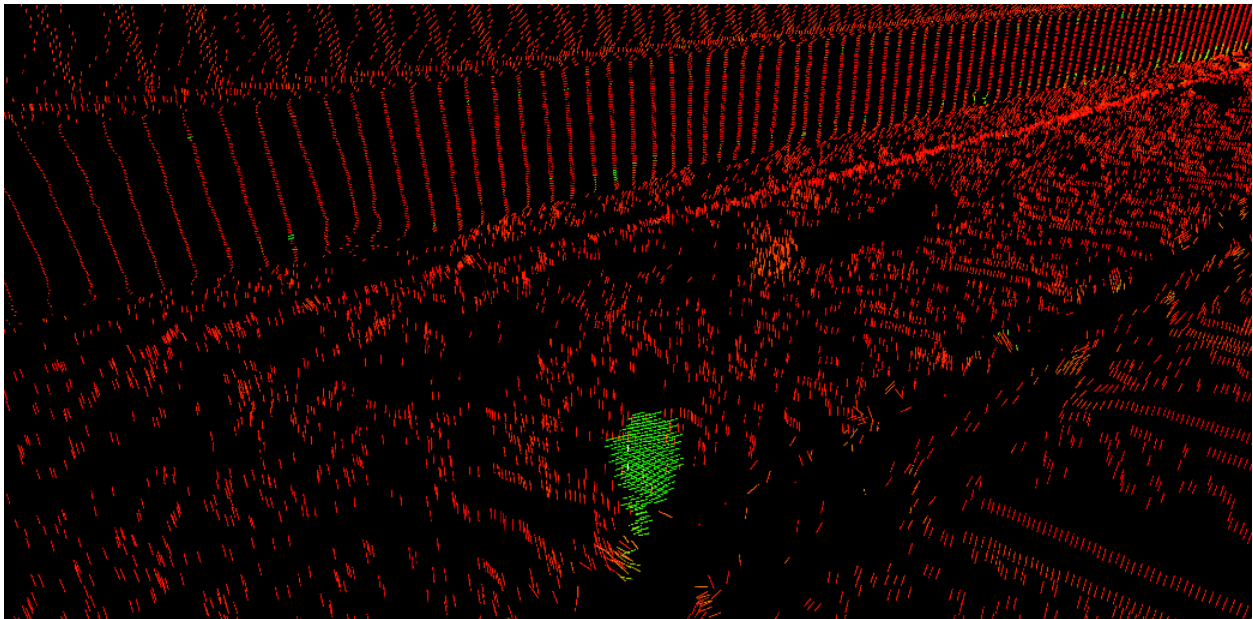
Figure 5-9: Example of normal vector visualization in combination with incidence angle-based color within the tunnel portion of Scan C. The red colored normal vectors in this image generate large incidence angles relative to the laser beam path. The small group of green normal vectors near the center of the image, represent points from a survey target that was oriented to achieve low incidence angle with the TLS laser beam.

5.4 RESULTS AND DISCUSSION

The proposed GLSL shader-based uncertainty calculation and visualization methodology was used to visually explore how the considered error sources behave with the chosen TLS datasets. The error sources have been divided into two categories: range, and angular, similar to the approach of Hartzell et al. (2015). Uncertainty visualization examples representing full uncertainty, range-only uncertainty, and angular-only uncertainty are presented for Scans A, B, and C (Figure 5-10). Across the three TLS datasets, the majority of 3D uncertainty is contributed by range-based errors. This finding will be further discussed in subsequent sections.

The recognizable geometric shapes visible in Scan A serve well as a simple example to communicate the variability in spatial uncertainty throughout a TLS point cloud. Additionally, given the short range and limited horizontal and vertical extent of the Scan A point cloud, it showcases the effects of beamwidth-induced range error. From the full uncertainty image for Scan A (Figure 5-10), relatively higher levels of uncertainty are observed on the floor and ceiling when compared with the wall. This is attributed to the adverse scanning incidence angle that is generated due to the relative location of the TLS instrument to these horizontal surfaces. Incidence angles on the back wall are more favorable (lower), and therefore the points have less uncertainty. Likewise, degradation in point accuracy is also observed on curved surfaces such as the two balls, the safety cones, and the pipe suspended from the ceiling. Curved surfaces result in somewhat of a specular highlight of lower uncertainty where incidence angles are favorable, followed by a degradation of accuracy at a rate proportional to the degree of curvature.
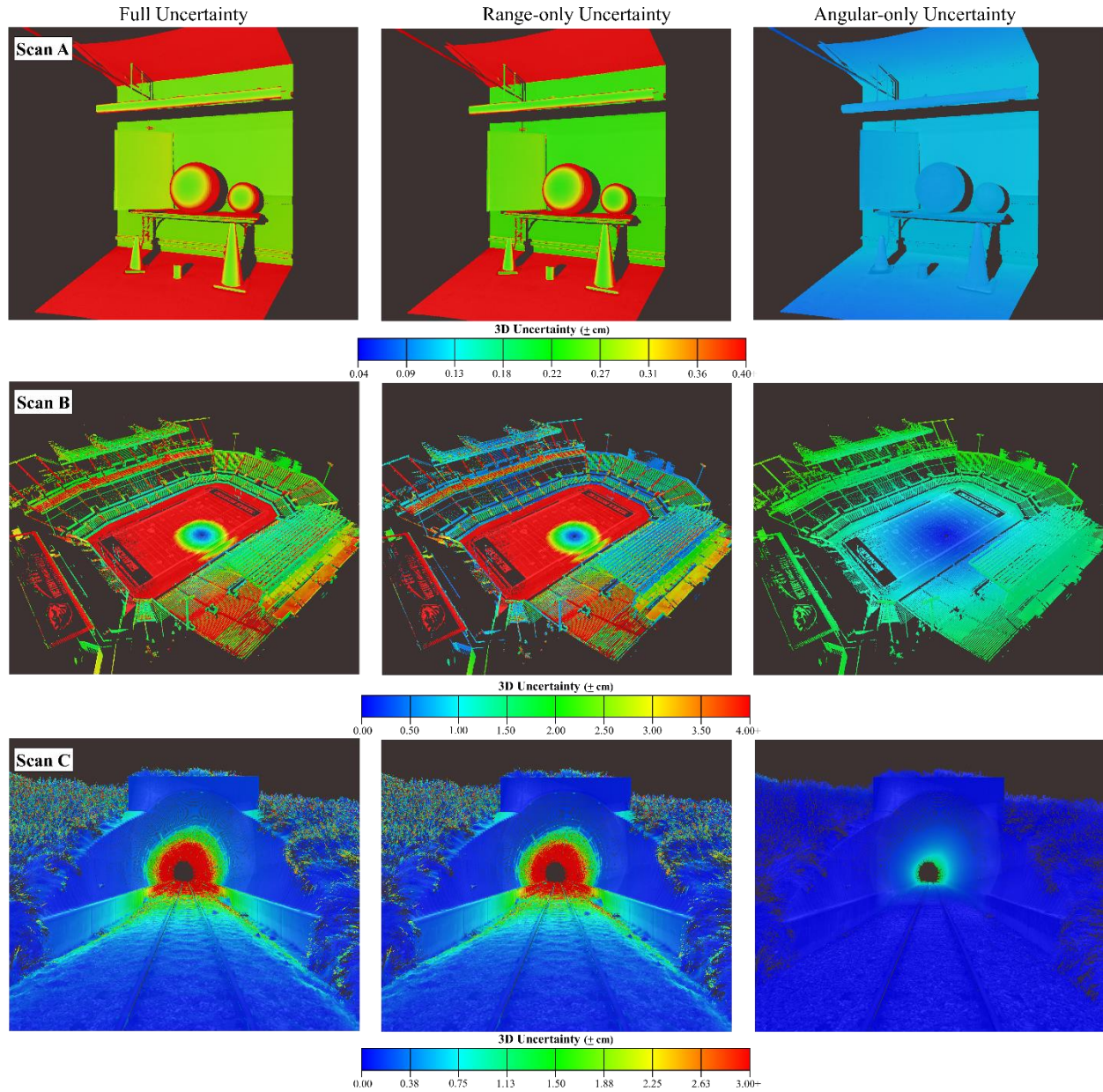
Figure 5-10: Uncertainty visualizations for Scans A, B, and C considering both range and angular-based uncertainty (full uncertainty), solely range-based uncertainty (range-only uncertainty), and only angular uncertainty (angular-only uncertainty).

Due to the extensive variation in range and surface orientation in Scan B, it will be used to further discuss range and angular-based uncertainty in subsequent sections. The train tunnel captured in Scan C represents a unique situation where both range and incidence angle rapidly increase together as the data extends into the tunnel. Given the scanner was located on a tripod set up on the train track, uncertainty increases more rapidly on the ground surface when compared to the top of the tunnel. Based on measurements made in the point cloud, the beginning of the red region ($\sim \pm$ 3 cm error) on the ground begins at $\sim$ 15 m from the scanner position. The actual TLS survey for this train tunnel included additional scans performed in the tunnel, which would provide more accurate data in this region. Visually communicating point cloud uncertainty, as demonstrated here, can inform future TLS acquisition decisions, as well as provide insight into what points from each scan position should be utilized (i.e., combination of data based on uncertainty).

It is important to note that a key contribution of this tool is its dynamic and interactive functionality when it comes to manipulating the magnitude of error sources and the mathematical relationships responsible for propagating the uncertainty. This capability can be difficult to communicate in written form with static images; hence, the reader is encouraged to take this into consideration.

5.4.1   Range Uncertainty

To understand better how range-based uncertainties behave with respect to the implemented uncertainty propagation, Scan B was visually analyzed using solely range-based errors for the uncertainty propagation. From Figure 5-10, it can be deduced that range-based errors contribute more to point cloud uncertainty than angular errors. This is attributed to the way in which

beamwidth range error is calculated (equation 4-3). Equation 4-3 strives to account for laser beam terrain/object interaction by using the incidence angle between the laser beam and the estimated normal vector for a given point.

5.4.1.1 Beamwidth-induced Range Error

To demonstrate the effect this interaction has on the uncertainty propagation, Figure 5-11 presents comparative 3D uncertainty visualizations where only the manufacturer specifications for range uncertainty are considered compared to using both the specifications and beamwidth-derived range error.
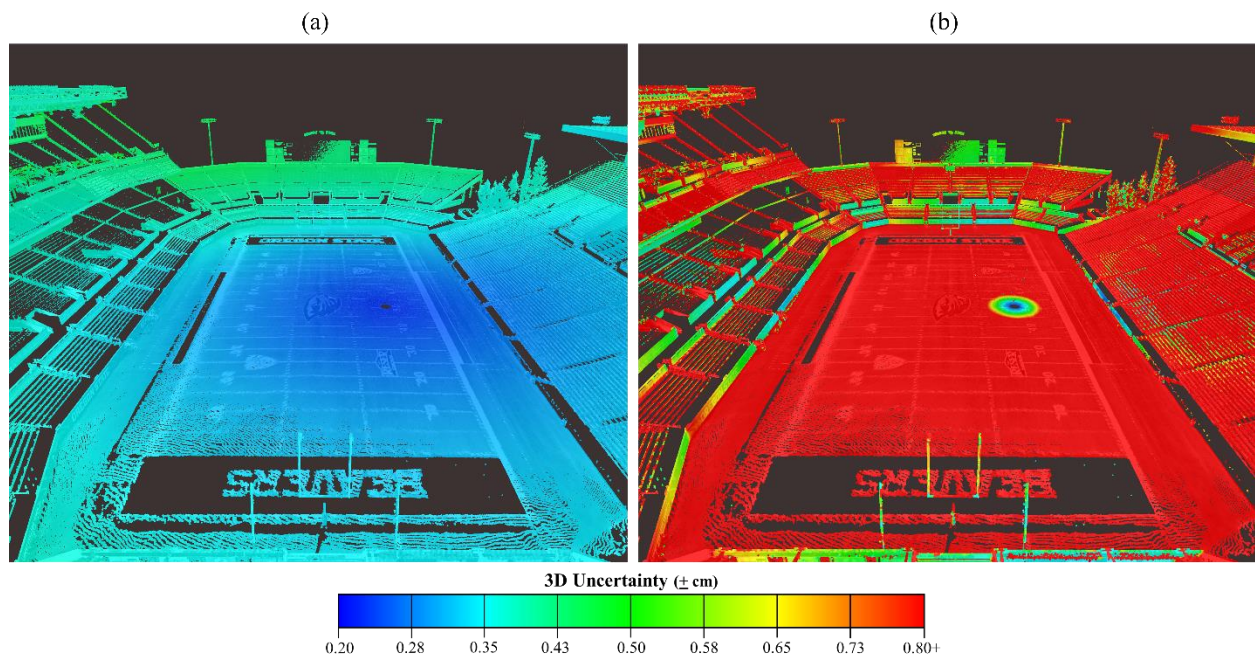
Figure 5-11: Visualization of range-based 3D uncertainty using only manufacturer specifications for range error (a) and results when including both specifications and beamwidth-derived range error (b).

From these results, we see a significant increase in uncertainty when we include beamwidth-derived range errors for the propagation of point cloud uncertainty. In Figure 5-11(a), 3D uncertainty appears to increase uniformly as the distance from the scanner origin (range) increases. Close examination indicates no response of uncertainty associated with abrupt changes in the orientation or geometry of scanned objects and the terrain. When including beamwidth range error, the changes in propagated uncertainty are clearly visible. In Figure 5-11(b), the points representing surfaces that are near horizontal have 3D uncertainties $> \pm$ 0.80 cm due to high incidence angles relative to the scanner origin (near middle of football field) and the resulting laser beam path. Significant changes in uncertainty are observed with rapid changes in the scanned geometry. For instance, a large decrease in 3D uncertainty is observed when transitioning from the football field to the vertical wall surrounding the field. The sharp transition from high to relatively low uncertainty is due to the rapid change in laser beam incidence angle associated with these surfaces.

5.4.1.2 Considering Laser Beam Exit Diameter

As described in Section 5.3.3, the beamwidth range error equation from Hartzell et al. (2015) was modified to consider laser beam exit diameter. To see what effect this has on the propagated uncertainty, the visualization tool was used to swap laser beam exit diameter in and out of the beamwidth range equation (

Figure 5-12).

Without Laser Beam Exit Diameter   With Laser Beam Exit Diameter

3D Uncertainty (± cm)

0.00   0.75   1.50   2.25   3.00   3.75   4.50   5.25   6.00+

3D Uncertainty Cutoff = ± 6 cm

Figure 5-12: Visualization of range-based 3D uncertainty with and without laser beam exit diameter using Mode 1 (top) and Mode 2 (bottom).

Scan B serves as an appropriate example for observing the differences in propagated uncertainty associated with using laser beam exit diameter because of the visible yardage markers on the football field. Following the bottom sideline of the football field,
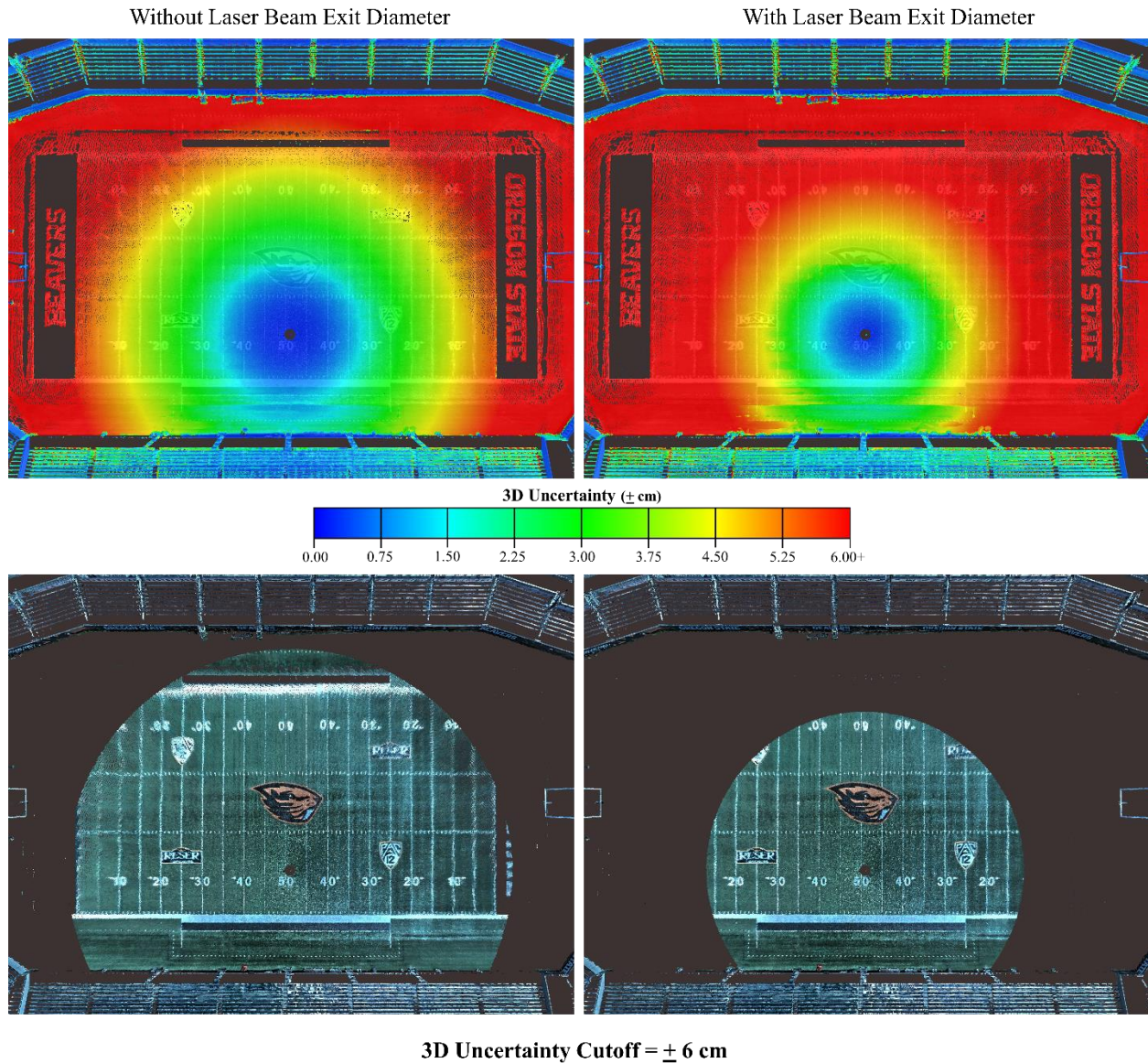
Figure 5-12 reveals that when omitting beam exit diameter from the beamwidth range equation, the $\pm$ 6 cm uncertainty cutoff lands near the beginning of the left ("BEAVERS") end zone; whereas, when incorporating beam exit diameter, the uncertainty cutoff lands near the 15-yard line. Likewise, the cyan colored area ($\pm$ 1.5 cm) lands near the 38-yard line when laser beam exit diameter is ignored, and moves to the 48-yard line when beam exit diameter is considered. These results demonstrate that including laser beam exit diameter makes a significant difference in the propagated uncertainty. The increase in uncertainty associated with including beam exit diameter is attributed to a larger projected laser beam footprint interacting with the scanned scene through the beamwidth range error equation (equation 3). This results in a larger extent for range creep to take place and, therefore, larger positional uncertainty.

5.4.1.3   3D, Horizontal, and Vertical Components of Range Uncertainty

Visualizations were generated that present 3D, horizontal, and vertical uncertainty for Scan B based on range-only error sources (Figure 5-13). The images in Figure 5-13 indicate the majority of the propagated 3D uncertainty for Scan B is contributed by horizontal uncertainty. Subtle variation in vertical uncertainty is observed in the upper reaches of the stadium, where the pulses become more oblique in the vertical direction. Surfaces that are both at a large distance and at high incidence angle relative to the scanner origin result in the highest vertical uncertainty. Higher uncertainty is observed on near horizontal surfaces when compared to vertical surfaces, which makes sense given the incidence angle component included in beamwidth range error equation (equation 3). As expected, the spatial distribution of error in the immediate vicinity of the scan origin appears different in the 3D and Horizontal uncertainty visualizations. The

reduction in the size of the $\pm$ 2 cm 3D uncertainty zone compared to the horizontal equivalent is due to the uncertainty contributed by the vertical component.
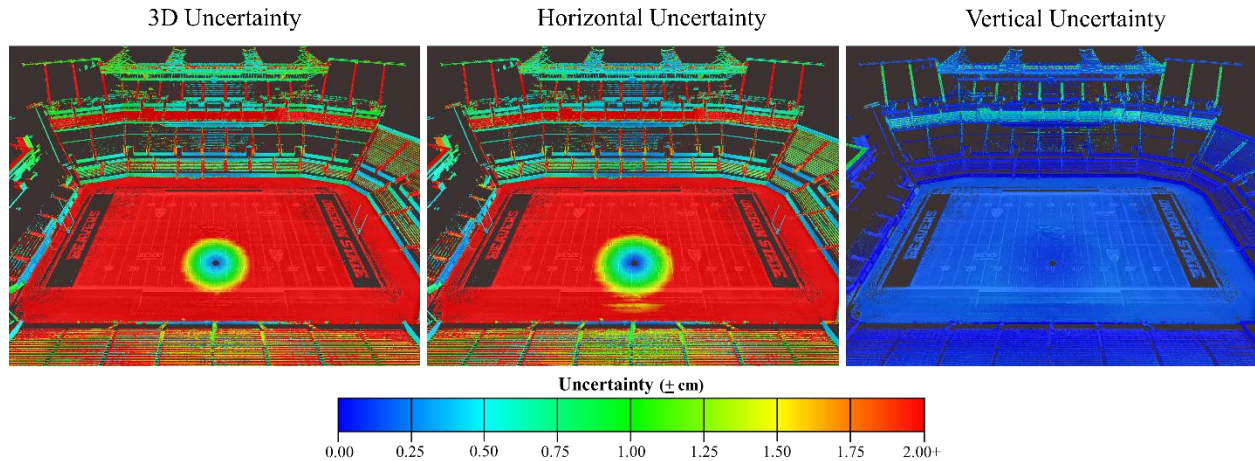
Figure 5-13: Visualizing the 3D, horizontal, and vertical components of range-based uncertainty.

5.4.2   Angular Uncertainty

For demonstration of how angular uncertainties behave with respect to the implemented uncertainty propagation, Scan B was visually analyzed using solely angular-based error components for the uncertainty propagation computations. Figure 5-10 shows that angular errors contribute significantly less to the point cloud uncertainty propagation when compared with range-based errors.

5.4.2.1   Beamwidth-induced Angular Error

When comparing visualization results for including and ignoring beamwidth angular error (Figure 5-14), an increase in 3D uncertainty is observed when including beamwidth angular error; however, the difference is not as large as that observed with the range-only uncertainty scenario (Figure 5-11). This is a result of how beamwidth contributes to angular error. Unlike beamwidth range error, beamwidth angular error (equation 4-2) does not consider incidence

angle and the interaction of the laser beam with the scanned scene. This results in a relatively lower level of uncertainty contributed by angular based errors and also explains why we do not see the same behavior in terms of abrupt changes in uncertainty between near horizontal and near vertical surfaces.
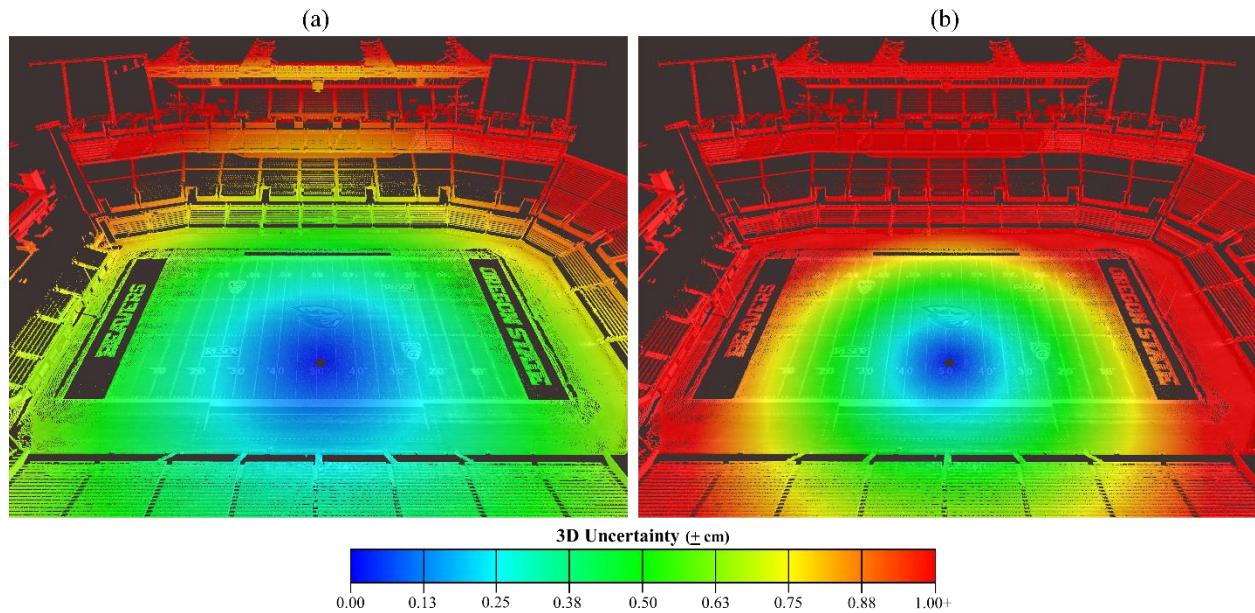
Figure 5-14: Visualization of angular-based 3D uncertainty using only manufacturer specifications for angular errors (a) and results when including both specifications and beamwidth-derived angular error (b).

5.4.2.2   3D, Horizontal, and Vertical Components of Angular Uncertainty

Results of calculating and visualizing 3D, Horizontal, and Vertical uncertainty for Scan B using only angular error sources (Figure 5-15) indicate similar uncertainty behavior as observed for the range-only scenario (Figure 5-13).

3D Uncertainty   Horizontal Uncertainty   Vertical Uncertainty

Uncertainty (± cm)

0.00   0.13   0.25   0.38   0.50   0.63   0.75   0.88   1.00+
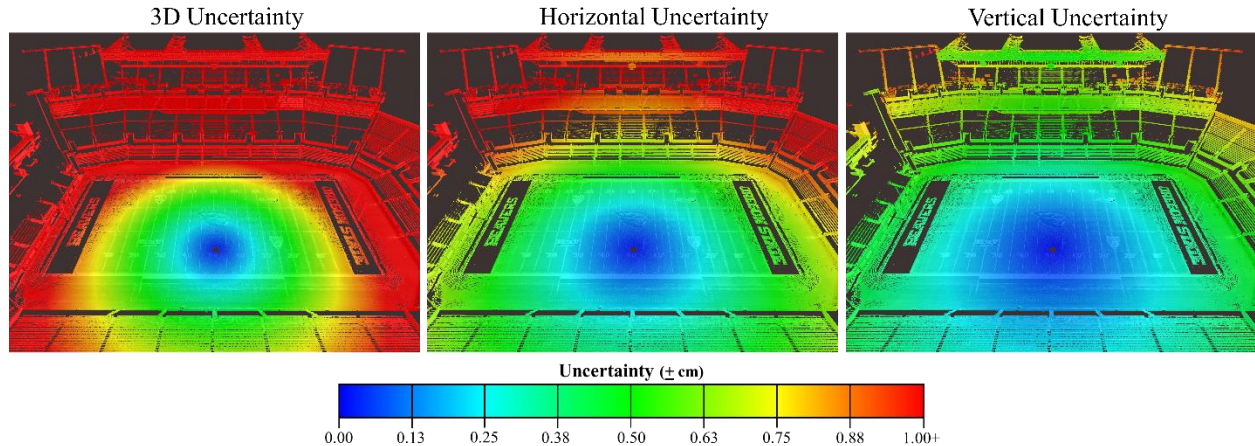
Figure 5-15: Visualizations of 3D, horizontal, and vertical angular uncertainty.

5.4.3   Uncertainty Visualization of a Complex Forest Environment

Scan D demonstrates the performance of the proposed visualization tool in a complex, highly variable environment (Figure 5-16). The point cloud of this densely forested environment affords numerous naturally irregular surfaces/objects, and uniform manmade surfaces that provide interesting examples of point cloud uncertainty visualization. Various examples of point cloud uncertainty behavior are presented in Figs. 16-20 and will be explored in this section.

The visualization results presented in Figure 5-16, indicate rapid changes in uncertainty occur across the complex natural features in the scanned scene (e.g., trees, ground vegetation, and rocks) compared to more gradual variation in uncertainty across the manmade objects (e.g., foot bridge and storage shed). A steady degradation of accuracy is observed as ranges increase into the further reaches of the forest. A closer look at some of the natural surfaces in Scan D are included in Figure 5-17.
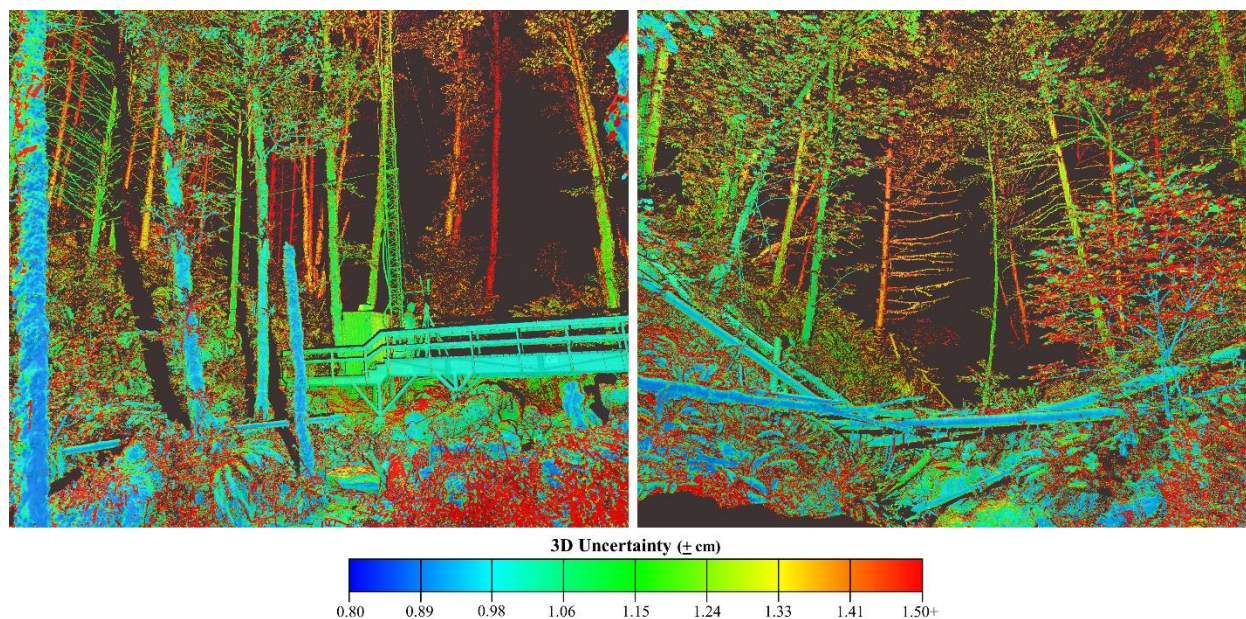
Figure 5-16: Two overview uncertainty visualization images of Scan D, looking through the forest.
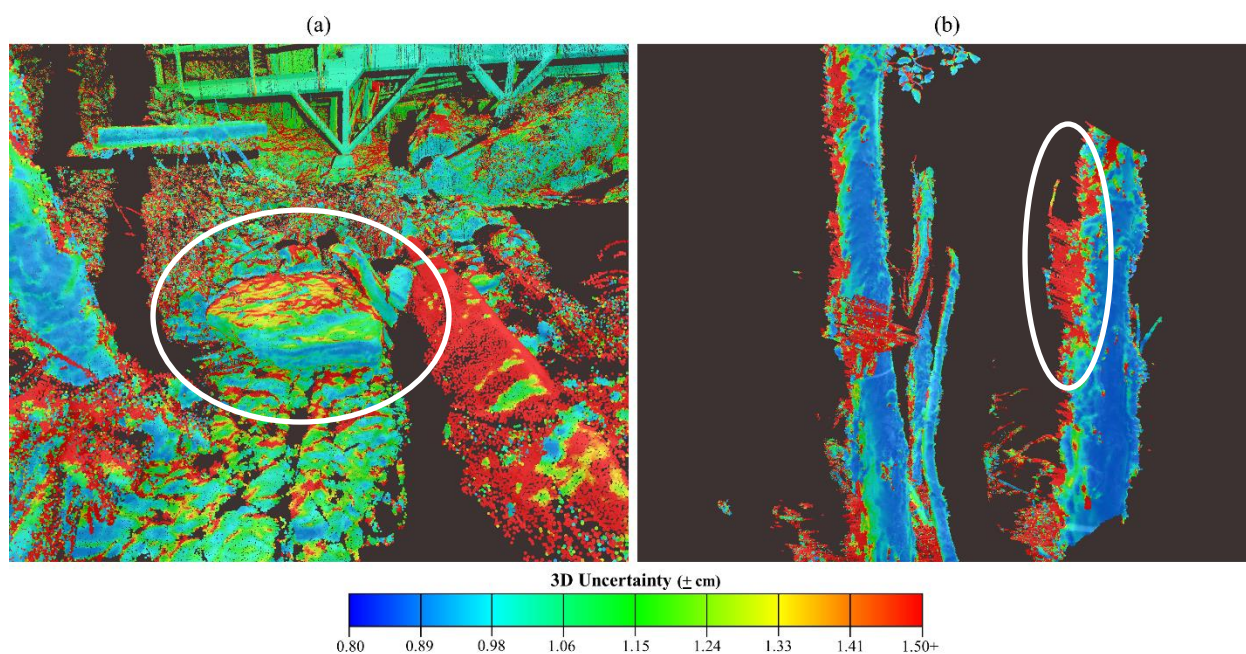
Figure 5-17: Close-up uncertainty visualization examples of complex natural surfaces including a rough rock (circled) (a) and mixed pixels located on the sides of tree trunks (b).

The large rock located in the center of the Figure 5-17(a) image is a good example of how uncertainty can erratically change across an irregular surface. The relative uncertainty of points that make up an object could be taken into consideration when making observations and/or measurements, and when generating mesh-based 3D models. The tree trunks displayed in Figure 5-17(b) show a degradation in accuracy as the incidence angle between the laser beam and cylindrically shaped tree trunk increases on the outer extents of the trunk. In addition, swaths of mixed pixel (Vosselman and Maas 2010) artifacts are visible in Figure 5-17(b) (circled in white). The erroneous geometry generated by mixed pixels tend to generate normal vectors that are oblique to the original path of the laser beam, which results in a higher level of uncertainty.

An additional example of uncertainty visualization for a natural object is included in Figure 5-18. The tree and its foliage displayed in Figure 5-18, provides insight into how 3D uncertainty can vary across the different parts of a deciduous tree. Uncertainty propagation results indicate that the trunk and branch structure of the tree is relatively more accurate than the adversely oriented and likely mixed pixel-inducing leaves. On the slope beneath the tree, patches of relatively lower uncertainty (blue and cyan) are observed amongst the higher uncertainty points (red) caused by the vegetation. The lower uncertainty patches are attributed to bare ground and exposed rocks, which are difficult to identify in the RGB colored point cloud. These regions have lower uncertainty relative to the vegetated areas because of their orientation relative to the incident laser beam and the lack of beam splitting noise (i.e., mixed pixels), which is very prevalent amongst the vegetated areas.

RGB Color   Uncertainty

3D Uncertainty (± cm)

0.80   0.89   0.98   1.06   1.15   1.24   1.33   1.41   1.50+
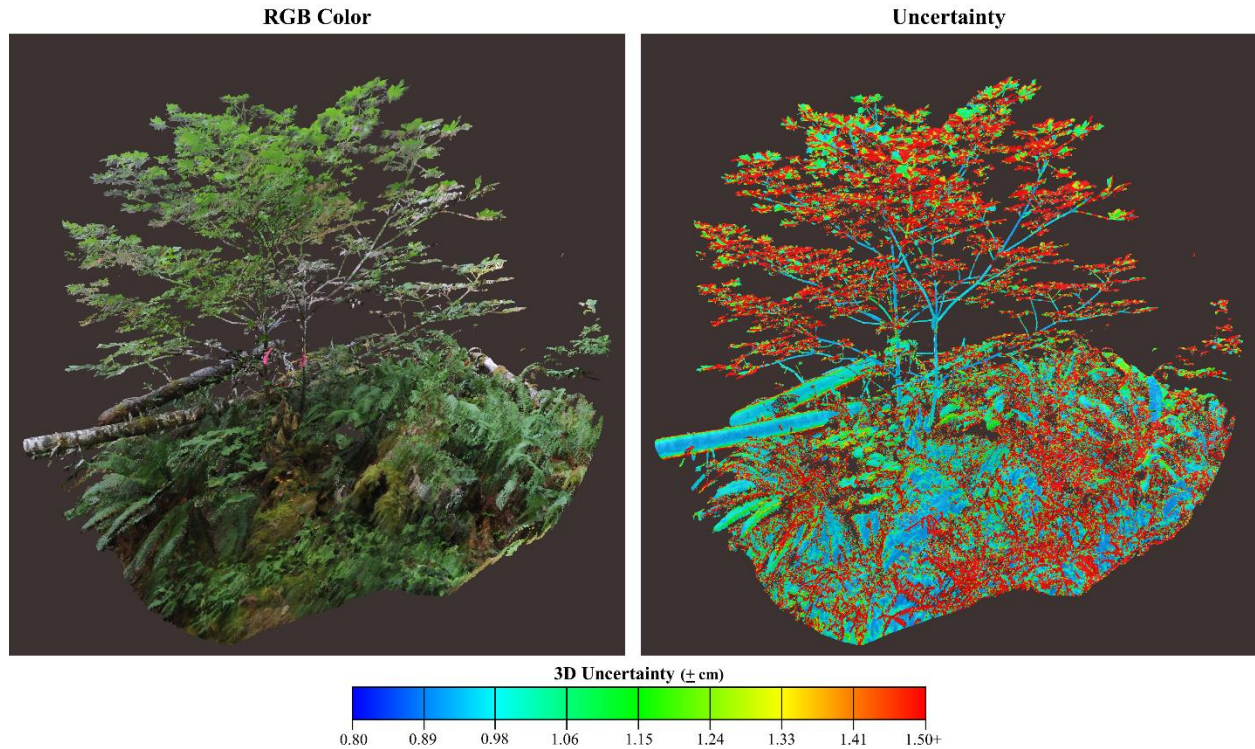
Figure 5-18: RGB color (left) and uncertainty (right) visualizations of a deciduous tree and its foliage.

The tall trees in close proximity to the scanner origin presented in Figure 5-19, provide an opportunity to observe a rapid increase in vertical uncertainty relative to the other TLS datasets. As the laser beam scans up the tree trunk, the incidence angle increases, resulting in an enlarged laser beam footprint that is stretched along a near vertical axis (Z-axis). This results in the majority of beamwidth-induced range error being transmitted to the vertical uncertainty component.

Vertical Uncertainty (± cm)

| 0.00 | 0.05 | 0.10 | 0.15 | 0.20 | 0.25 | 0.30 | 0.35 | 0.40+ |
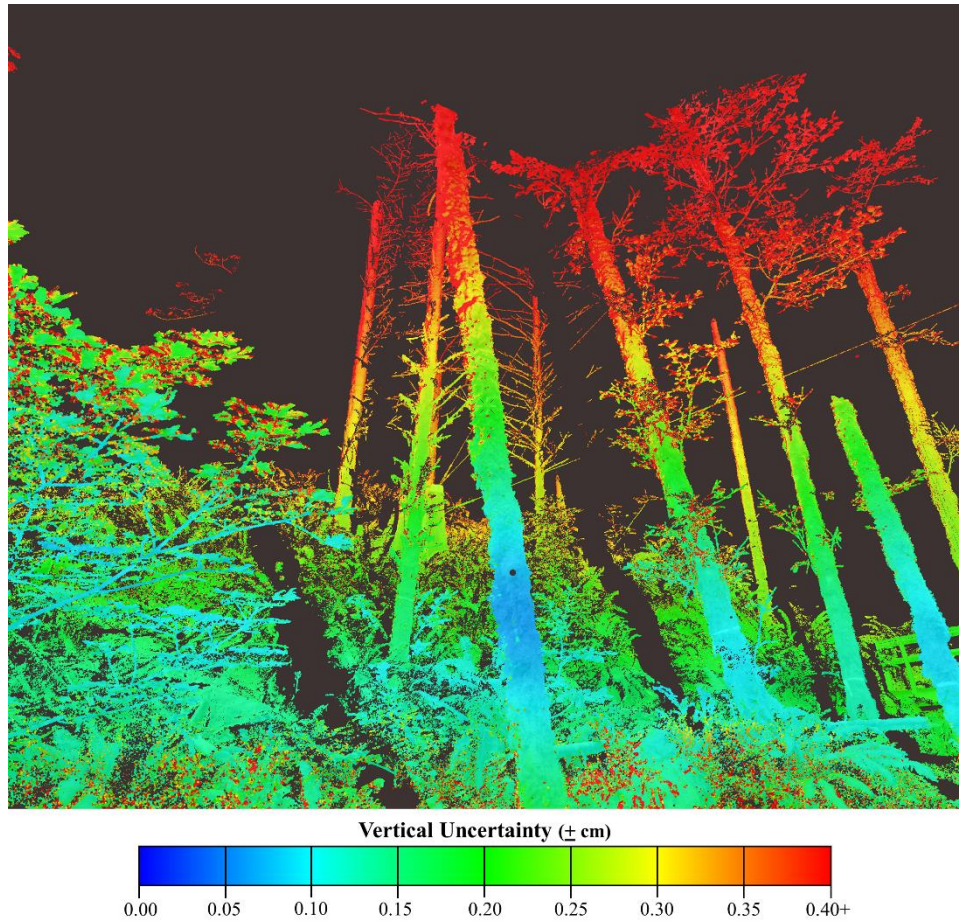
Figure 5-19: Variation in vertical uncertainty observed on tree trunks in close proximity to the scanner origin.

Focusing on the manmade objects present in the scanned scene, the structural elements beneath the wooden foot bridge (Figure 5-20), provide useful information regarding how point cloud uncertainty can vary in a relatively small area.
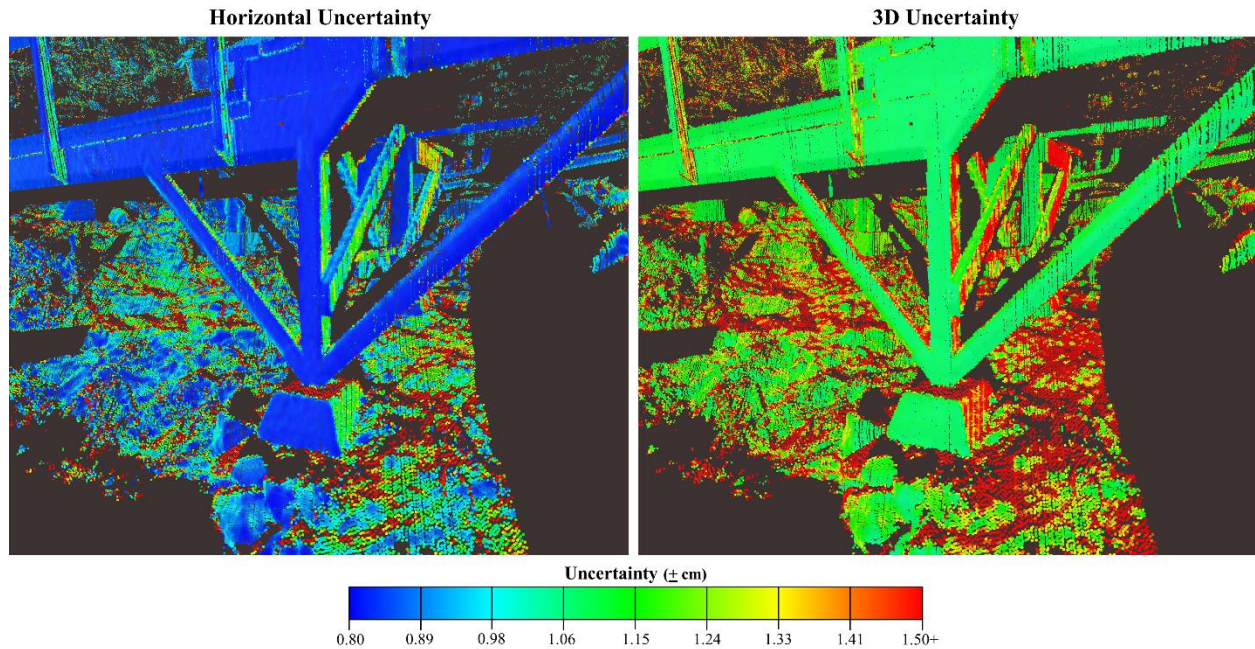
Figure 5-20: Uncertainty visualization of structural elements beneath wooden foot bridge.

The right-angle geometry of the wood elements and concrete footing block visible in Figure 5-20 provide a good example of how horizontal and 3D uncertainty can vary in TLS point cloud data. In the horizontal uncertainty image, each visible face of the concrete footing block has a different magnitude starting with ~ ± 8 mm (blue) for the front face, ~ ± 11.5 mm for the right side, and ≥ 15 mm for the top (red). This equates to ~ 3.5 mm of horizontal uncertainty change from the front face to the right face, and an ~ 7 mm change in horizontal uncertainty from the front face to the top of the footing. The 3D uncertainty image indicates an overall increase in uncertainty due to small contributions in vertical uncertainty. The magnitude of 3D uncertainty on the top, horizontal, surface of the footing is similar to the identified horizontal uncertainty due to the lack of vertical variation of the surface. As expected, surfaces of the wood members and concrete footing that are oriented obliquely relative to the laser beam path have a lower accuracy compared with surfaces that are oriented more orthogonally relative to the beam path.

5.5 CONCLUSION

The GLSL shader-based solution presented herein for calculation and visualization of point cloud uncertainty is both efficient and flexible. Leveraging the power of computer graphics hardware and software enables the efficient calculation and interactive visualization of point cloud uncertainty. Determination of per-point uncertainty for TLS point clouds can facilitate the combination of data (e.g., co-registration of point clouds) while accounting for uncertainty; as well as, enable the evaluation of uncertainty for downstream products such as digital elevation models, surface meshes, and 3D-solid models. The proposed uncertainty visualization framework provides insight into the primary factors affecting the spatial variability of point cloud uncertainty. Intuitive communication of point cloud uncertainty is necessary for informing end users of laser scanning data about the variable spatial quality of point cloud data and raising awareness regarding how scanning geometry affects point cloud uncertainty.

The interactive nature of the proposed tool enabled the efficient development of a new beamwidth-derived range error equation and fostered a better understanding of point cloud uncertainty behavior. When manipulating computations and/or the magnitude of error sources, the immediate visual feedback facilitates the user to perform an intuitive visual sensitivity analysis. The impact a given change has on the uncertainty propagation can be quite clear when the visual results respond quickly.

The existing framework does not consider errors stemming from anomalous surfaces such as retro-reflective materials (e.g., traffic signs), and very rough surfaces. When a laser beam is pointed at a retro-reflective surface, most of the light energy is returned to the source. This can

result in saturation of the laser scanner pulse sensor, which leads to error in range determination. Likewise, range error can result from the scattering of light caused by rough surfaces. For highly reflective surfaces, determination of range errors may be possible by utilizing the intensity information commonly recorded for each point. Normalized intensity (Kashani et al. 2015) values have potential for identifying surfaces in a scanned scene that may cause saturation-based range errors and aid in the calculation of their magnitude. For rough surfaces, utilizing normal vector uncertainty in the total uncertainty propagation may facilitate estimating range errors associated with the scattering of light energy. Future work will include developing support for point clouds comprised of multiple scans. Such a capability will require the theoretical development of additional uncertainty propagation terms and computations, which account for the registration and if applicable, the geo-referencing of the individual scans. As the uncertainty propagation methodology increases in complexity, further validation of the calculated uncertainty is necessary. This validation can be performed empirically by comparing TLS data with poor scanning geometry to a TLS dataset with optimal scanning geometry, or by using a control network and total station instrument similar to the methods presented in Chapter 3.

In addition, applications that utilize estimations of per-point uncertainty will be explored and developed. For instance, when making a point-to-point measurement in a 3D point cloud, a measurement uncertainty could be provided based on the computed spatial uncertainty of the two end points. Future work will also include, performing visual comparisons of additional uncertainty propagation models, exploring the potential for scanner manufacturers to use this visualization tool to virtually test scanner components with different accuracies, and implementing this shader code in other open-source point cloud viewers.

5.6 ACKNOWLEDGEMENTS

5.7 REFERENCES

Bailey, M., and Cunningham, S. (2012). Graphics Shaders Theory and Practice. Taylor & Francis Group, Boca Raton, FL.

Baltsavias, E. P. (1999). "Airborne laser scanning: basic relations and formulas." ISPRS Journal of Photogrammetry and Remote Sensing, 54(2), 199–214.

Barbarella, M., Fiani, M., and Lugli, A. (2017). "Uncertainty in Terrestrial Laser Scanner Surveys of Landslides." Remote Sensing, 9(2), 113.

Chen, X., Zhang, G., Hua, X., and Xuan, W. (2016). "An Average Error-Ellipsoid Model for Evaluating TLS Point-Cloud Accuracy." The Photogrammetric Record, 31(153), 71–87.

Cuartero, A., Armesto, J., Rodríguez, P. G., and Arias, P. (2010). "Error Analysis of Terrestrial Laser Scanning Data by Means of Spherical Statistics and 3D Graphs." Sensors, 10(11), 10128–10145.

Dübel, S., Röhlig, M., Tominski, C., and Schumann, H. (2017). "Visualizing 3D Terrain, Geo-Spatial Data, and Uncertainty." Informatics, 4(1), 6.

Fan, L., Smethurst, J. A., Atkinson, P. M., and Powrie, W. (2015). "Error in target-based georeferencing and registration in terrestrial laser scanning." Computers & Geosciences, 83, 54–64.

Foster, C. (2017). Displaz lidar viewer software. < http://c42f.github.io/displaz/>

Ghilani, C. (2010). Adjustment Computations. John Wiley & Sons, Hoboken, NJ.

Girardeau-Montaut, D. (2017). Cloud Compare software. < http://www.danielgm.net/cc/>

Glennie, C. (2007). "Rigorous 3D error analysis of kinematic scanning LIDAR systems." Journal of Applied Geodesy jag, 1(3), 147–157.

Goulden, T., and Hopkinson, C. (2014). "Mapping simulated error due to terrain slope in airborne lidar observations." International Journal of Remote Sensing, 35(20), 7099–7117.

Hartzell, P. J., Gadomski, P. J., Glennie, C. L., Finnegan, D. C., and Deems, J. S. (2015). "Rigorous error propagation for terrestrial laser scanning with application to snow volume uncertainty." Journal of Glaciology, 61(230), 1147–1158.

Hodge, R. A. (2010). "Using simulated Terrestrial Laser Scanning to analyse errors in high-resolution scan data of irregular surfaces." ISPRS Journal of Photogrammetry and Remote Sensing, 65(2), 227–240.

Huber, D. (2011). "The ASTM E57 File Format for 3D Imaging Data Exchange." Proceedings of the SPIE Vol. 7864A, Electronics Imaging Science and Technology Conference (IS&T), 3D Imaging Metrology, Pittsburgh, PA.

Kashani, A. G., Olsen, M. J., Parrish, C. E., and Wilson, N. (2015). "A Review of LIDAR Radiometric Processing: From Ad Hoc Intensity Correction to Rigorous Radiometric Calibration." Sensors, 15(11), 28099–28128.

Kessenich, J., Baldwin, D., and Rost, R. (2004). "The OpenGL Shading Language Version 1.10." 3Dlabs, Inc. Ltd.

Kessenich, J., Baldwin, D., and Rost, R. (2017). "The OpenGL Shading Language Version 4.6." The Khronos Group, Inc.

Laefer, D. F., Fitzgerald, M., Maloney, E. M., Coyne, D., Lennon, D., and Morrish, S. W. (2009). "Lateral image degradation in terrestrial laser scanning." Structural Engineering International, 19(2), 184–189.

Leica Geosystems. (2015). Cyclone. Leica Geosystems. < http://hds.leica-geosystems.com/en/Leica-Cyclone_6515.htm>

Leica Geosystems. (2016). "Leica ScanStation P30/P40 Product Specifications." < http://pdf.directindustry.com/pdf/leica-geosystems/leica-scanstation-p30-p40-data-sheet/14324-610554-_2.html>

Lichti, D., Gordon, S. J., and Tipdecho, T. (2005). "Error Models and Propagation in Directly Georeferenced Terrestrial Laser Scanner Networks." Journal of Surveying Engineering, 131(4), 135–142.

Mason, J. S., Retchless, D., and Klippel, A. (2017). "Domains of uncertainty visualization research: a visual summary approach." Cartography and Geographic Information Science, 44(4), 296–309.

Mezian, M., Vallet, B., Soheilian, B., and Paparoditis, N. (2016). "Uncertainty Propagation for Terrestrial Mobile Laser Scanner." International Archives of Photogrammetry, Remote Sensing and Spatial Information Sciences, Prague, Czech Republic.

Morin, K. W. (2002). "Calibration of Airborne Laser Scanners." University of Calgary, Calgary, Alberta.

Olsen, M. J., Johnstone, E., Driscoll, N., Ashford, S. A., and Kuester, F. (2009). "Terrestrial Laser Scanning of Extended Cliff Sections in Dynamic Environments: Parameter Analysis." Journal of Surveying Engineering, 135(4), 161–169.

Riegl. (2016). RiScan Pro. Riegl. < http://www.riegl.com/products/software-packages/riscan-pro/>

Riegl. (2017). "Riegl VZ-400 Datasheet." < http://www.riegl.com/uploads/tx_pxprieegldownloads/10_DataSheet_VZ-400_2017-06-14.pdf>

Schaer, P., Skaloud, J., Landtwing, S., and Legat, K. (2007). "Accuracy Estimation for Laser Point Cloud Including Scanning Geometry." International Archives of Photogrammetry, Remote Sensing and Spatial Information Sciences 36 (Part 5/C55),279-353, Padova (Italy).

Silvia, E. P., and Olsen, M. J. (2012). "To Level or Not to Level: Laser Scanner Inclination Sensor Stability and Application." Journal of Surveying Engineering, 138(3).

Soudarissanane, S., Lindenbergh, R., Menenti, M., and Teunissen, P. (2011). "Scanning geometry: Influencing factor on the quality of terrestrial laser scanning points." ISPRS Journal of Photogrammetry and Remote Sensing, 66(4), 389–399.

Telling, J., Lyda, A., Hartzell, P., and Glennie, C. (2017). "Review of Earth science research using terrestrial laser scanning." Earth-Science Reviews, 169, 35–68.

Turk, G. (1998). "The PLY Polygon File Format." Georgia Institute of Technology.

Vosselman, G., and Maas, H.-G. (2010). Airborne and Terrestrial Laser Scanning. Whittles Publishing, Scotland, UK.

Williams, K., Olsen, M. J., Roe, G. V., and Glennie, C. (2013). "Synthesis of Transportation Applications of Mobile LIDAR." Remote Sensing, 5(9), 4652–4692.

6   CONCLUSIONS AND FUTURE WORK

6.1   CONCLUSION

This dissertation presents novel research on the detection and classification of data gaps in TLS-derived DEMs (Chapter 2), the influence of TLS acquisition and DEM creation parameters on DEM completeness (Chapter 3), the suitability of UAS and handheld camera-based SfM for the automated assessment of unstable rock slopes (Chapter 4), and the propagation and visualization of TLS point cloud uncertainty. These studies raise awareness and contribute to the knowledge-base regarding the limitations of current 3D capture technology and techniques. Additionally, aspects of this research are directly applicable to both the research community and industry practitioners.

Chapter 2 presents an automated data gap detection and classification methodology for TLS-derived DEMs that can aid in the judgement of TLS survey quality and identify pooled water in certain scanned scenes. Additionally, knowledge of data gap sources can lead to better understanding of DEM quality and preferred post-processing techniques.

In Chapter 3, an upgradable empirical DEM completeness database and associated TLS acquisition planning tool is presented and demonstrated that can aid TLS surveyors in planning efficient field survey campaigns while meeting DEM quality requirements. Based on user provided inputs, the TLS planning tool provides recommendations for the minimum number of scan positions, scanning resolution, and estimated survey time.

Chapter 4 provides an accuracy assessment of SfM, which makes use of two high accuracy, high precision, independent references, which are tied to a rigorous survey control network. Prior

work in this area typically compares SfM results solely with ALS or TLS without a validation of the chosen reference. A quality assessment of the SfM data relative to TLS is provided that examines completeness, point density, and surface morphology. These metrics have not been rigorously evaluated in prior work, which tends to focus purely on geometric accuracy. Findings include: using both UAS and handheld camera-based imagery is a viable option for unstable rock slope characterization when tied to rigorous survey control, and concerns such as over-smoothing and inconsistencies question the suitability of SfM reconstruction for reliably detecting small rock slope changes over time.

In Chapter 5, a flexible and efficient solution for the calculation and intuitive visualization of TLS point cloud uncertainty is demonstrated and used to visually explore the behavior of different TLS point cloud error sources. The visualization solution utilizes a custom GLSL shader for both calculation (error propagation) and visualization of point cloud uncertainty. In addition, a new laser beamwidth-derived range error equation is proposed that considers laser beam exit diameter, which is very important for terrestrial laser scan data.

6.2 FUTURE WORK

The research included in this dissertation affords many opportunities for future work, which are included below:

For Chapter 2, classification of data gaps in TLS DEMs can enable optimization of post-processing techniques such as DEM hole filling by way of interpolation and/or surface patching. For instance, knowledge of data gap source could inform a method to fill occlusions using interpolation and use a hydro-flattening type technique to fill water-derived dropouts. Also, if the

scan line structure from ALS or MLS data could be reconstructed into a projected 2D image, this methodology could be applied to ALS- or MLS-derived DEMs.

Future work related to Chapter 3, involves incorporating additional empirical data into the DEM completeness database, which are representative of a variety of site conditions. Incorporating additional DEM completeness records combined with qualitative, site-specific, parameters for terrain complexity and obstacle quantity would dramatically improve the TLS planning tool's ability to provide realistic recommendations for a larger variety of site conditions. Additionally, in cases where *a priori* topographic data is available, the TLS planning tool could be used in combination with a new or existing scan placement optimization technique.

For Chapter 4, artifacts, such as over-smoothing and geometric inconsistencies stemming from differences in image acquisition have potential to introduce error into the detection of small changes. Further work is required to judge the performance of SfM for rock-slope monitoring and determine the threshold of change that can accurately and reliably be detected.

Future work for the research presented in Chapter 5 includes: development of support for point clouds comprised of multiple scans, perform visual comparisons of additional error propagation models, explore the potential for scanner manufacturers to use this visualization tool to virtually test scanner components with different accuracies, and develop support for reporting the uncertainty of point-to-point measurements based on the computed spatial uncertainty of the two end points. Future work will also include implementing the developed GLSL shader in the GeoMat VR immersive visualization system.

7 APPENDICES

7.1 APPENDIX A – TLS ACQUISITION PLANNING TOOL MATLAB SCRIPT

```
% DEM_ScanPlanning.m
% Author: Matt O'Banion
% Date Written: 07/09/17
% Last Modified: 09/25/17

clc
clear all

%Read in Database Csv
DataTable = csvread('DEMQualityDatabase.csv');
UserSize = input ('Please Enter the size of your site in sq. m: ');
UsrDemRes = input ('Enter the desired DEM Resolution in m: ');
UsrPtsCell = input ('Enter the minimum points/DEM pixel (1,2,5,10): ');
UsrComplete = input ('Enter the minimum completeness (%): ');

QtyScans = DataTable(:,1);
ScanRes = DataTable(:,2);
PtsCell = DataTable(:,3);
DemRes = DataTable(:,4);
Complete = DataTable(:,5);
Time = DataTable(:,6);
FinalScanQty = 0;

i =1;
for n = 1:length(QtyScans);
    if DemRes(n,1)<=UsrDemRes & PtsCell(n,1)>=UsrPtsCell & Complete(n,1)
>= UsrComplete
        SubQtyScans(i,1)=QtyScans(n,1);
        SubTime(i,1)=Time(n,1);
        SubScanRes(i,1)=ScanRes(n,1);
        i=i+1;
    end
end

minTime = 10000000;
RefScanQty =0;
RefScanRes = 0;
for n =1:length(SubTime);
    if SubTime(n,1) < minTime
        minTime = SubTime(n,1);
        RefScanQty = SubQtyScans(n,1);
        RefScanRes = SubScanRes(n,1);
    end
end
```

```
i=1;
for n=1:length(SubTime);
    if SubTime(n,1)== minTime
        Sub2QtyScans(i,1)=SubQtyScans(n,1);
        Sub2Time(i,1)=SubTime(n,1);
        Sub2ScanRes (i,1) = SubScanRes(n,1);
        i=i+1;
    end
end

maxScans = 0;
index = 0;
for n=1:length(Sub2QtyScans);
    if Sub2QtyScans(n,1) > maxScans
        maxScans = Sub2QtyScans(n,1);
        index = n;
    end
end
QtyMult=ceil(UserSize/300);
'Number of Scans: '
%ScanQty
if Sub2QtyScans(index)*QtyMult <=1
    FinalScanQty = (Sub2QtyScans(index)*QtyMult)+1
else
    FinalScanQty = Sub2QtyScans(index)*QtyMult
end
'Recommended Scan Resolution (deg): '
Sub2ScanRes(index)
'Estimated Time to Complete (Min): '
Sub2Time(index)*QtyMult
%ScanRes
```

7.2 APPENDIX B – GLSL SHADER CODE FOR TLS POINT CLOUD UNCERTAINTY VISUALIZATION IN DISPLAZ

```
#version 150
// Copyright 2015, Christopher J. Foster and the other displaz
contributors.
// Significantly modified and adapted by Matt S. O'Banion (9/15/2017)
// All uncertainty calculation and visualization related functionality
created by Matt S. O'Banion
// Use of this code is governed by the BSD-style license found in
LICENSE.txt

uniform mat4 modelViewMatrix;
uniform mat4 projectionMatrix;
uniform mat4 modelViewProjectionMatrix;

//----------------------------------------------------------------------
------
#if defined(VERTEX_SHADER)

uniform float radiusMultiplier = 0.002;//# uiname=Point Size; min=0.00001;
max=100

uniform float trimRadius = 1000000;//# uiname=Trim Radius; min=1;
max=1000000
//For Uncertainty Calculation
uniform float RangeSigma = 0.0012;          //# uiname=Range Sigma (m);
min=0.0; max=10.0
uniform float RangePPM = 10.0;          //# uiname=Variable Range (ppm);
min=0.0; max=100.0
uniform float HorizSigma = 0.0022;          //# uiname=HorizAngle Sigma
(deg); min=0.0; max=10.0
uniform float VertSigma = 0.0022;          //# uiname=VertAngle Sigma
(deg); min=0.0; max=10.0
uniform float BeamDivergence = 0.23;          //# uiname=BeamDivergence
(mrad); min=0.0; max=10.0
uniform float exitDiameter = 0.0032;          //# uiname=Exit Diameter (m);
min=0.0; max=10.0
uniform float IclinationSigma = 0.000416667;          //#
uiname=Inclination Sigma (deg); min=0.0; max=10.0

uniform int colorMode = 0;          //# uiname=Visualization Mode;
enum=Color|Intensity|Blend|Uncertainty|IncidenceAngle|HorizAngle|VertAngle
|Range
uniform float alpha = 0.3;          //# uiname=Blend; min=0.0; max=1.0

uniform int UncertType = 0;          //# uiname=Uncertainty Type;
enum=3D|Horiz|Vert
```

```
uniform int UncertViz = 0;           //# uiname=Uncertainty Mode; enum=Mode
1|Mode 2
uniform int NormalsOn = 1;           //# uiname=Normals; enum=Yes|No



uniform float Low = 0.0;             //# uiname=Low (m); min=0.0; max=10.0
uniform float High = 0.055;           //# uiname=High (m); min=0.0;
max=200.0
uniform float minRange = 0.0;          //# uiname=Min Range (m); min=0.0;
max=1000.
uniform float maxRange = 100;         //# uiname=Max Range (m); min=0.0;
max=1000.
uniform float ScanX = 0.0;           //# uiname=ScannerX (m); min=-100.0;
max=100.0
uniform float ScanY = 0.0;           //# uiname=ScannerY (m); min=-100.0;
max=100.0
uniform float ScanZ = 0.0;           //# uiname=ScannerZ (m); min=-100.0;
max=100.0


float PI = 3.14159265;

vec3 ScanOrigin = vec3(ScanX,ScanY,ScanZ);

uniform float minPointSize = 0;
uniform float maxPointSize = 400.0;

// Point size multiplier to get from a width in projected coordinates to
the
// number of pixels across as required for gl_PointSize
uniform float pointPixelScale = 0;
uniform vec3 cursorPos = vec3(0);
uniform int fileNumber = 0;

in vec3 position;
in vec3 color;
in float markersize;
in int markershape;
in float prop;//Matt: This is really intensity from CloudCompare PLY
in vec3 normal;

flat out float modifiedPointRadius;
flat out float pointScreenSize;
flat out vec3 pointColor;
flat out int markerShape2;
flat out vec2 lineNormal;
flat out float lineNormalLen;
flat out int NormalFlag;

float atan2(float y, float x)
{
```

```glsl
    return x == 0.0 ? sign(y)*PI/2 : atan(y, x);
}


vec3 hsb2rgb( vec3 c ){
    vec3 rgb = clamp(abs(mod(c.x*6.0+vec3(0.0,4.0,2.0),
                            6.0)-3.0)-1.0,
                    0.0,
                    1.0 );
    rgb = rgb*rgb*(3.0-2.0*rgb);
    return c.z * mix(vec3(1.0), rgb, c.y);
}
vec3 rgb2hsv(vec3 c){
    vec4 K = vec4(0.0, -1.0 / 3.0, 2.0 / 3.0, -1.0);
    vec4 p = mix(vec4(c.bg, K.wz), vec4(c.gb, K.xy), step(c.b, c.g));
    vec4 q = mix(vec4(p.xyw, c.r), vec4(c.r, p.yzx), step(p.x, c.r));

    float d = q.x - min(q.w, q.y);
    float e = 1.0e-10;
    return vec3(abs(q.z + (q.w - q.y) / (6.0 * d + e)), d / (q.x + e),
q.x);
}


vec3 hsv2rgb(vec3 c){
    vec4 K = vec4(1.0, 2.0 / 3.0, 1.0 / 3.0, 3.0);
    vec3 p = abs(fract(c.xxx + K.xyz) * 6.0 - K.www);
    return c.z * mix(K.xxx, clamp(p - K.xxx, 0.0, 1.0), c.y);
}
//Based on Rainbow transfer function from Graphics Shaders Theory and
Practice (Bailey and Cunningham, 2012)
vec3 Rainbow(float t,float min,float max){
    t=clamp(t,min,max);
    //t=t/(min+(max-min));
    t=(t-min)/(max-min);
    //b->c
    vec3 rgb=vec3(0.,4.*(t-(0./4.)),1.);

    //c->g
    if(t>=(1./4.))
        rgb=vec3(0.,1.,1.-4.*(t-(1./4.)));

    //g->y
    if(t>=(2./4.))
        rgb=vec3(4.*(t-(2./4.)),1.,0.);

    //y->r
    if(t>=(3./4.))
        rgb=vec3(1., 1.-4.*(t-(3./4.)),0.);

    return rgb;


}
```

```
vec3 GrayScaleColor(vec3 color){

    vec3 hsvB = rgb2hsv(color);
    hsvB[1]=0.0;
    vec3 colorB = hsv2rgb(hsvB);

    return colorB;

}

void main()
{
    NormalFlag = 0;
    vec4 p = modelViewProjectionMatrix * vec4(position,1.0);
    float r = length(position - cursorPos);
      float wInv = 1.0/p.w;
    modifiedPointRadius = radiusMultiplier * step(r, trimRadius);
    if (markersize != 0) // Default == 0 for in attributes.  TODO: this
isn't good in this case - what to do about it?
        modifiedPointRadius *= markersize;
     mat3x2 dProj = mat3x2(modelViewProjectionMatrix) -
                    outerProduct(wInv*p.xy,
transpose(modelViewProjectionMatrix)[3].xyz);
    // Remove aspect ratio - fragment coord system will be square.
    float aspect = projectionMatrix[1][1]/projectionMatrix[0][0];
    dProj = mat2x2(aspect, 0, 0, 1) * dProj;
    vec2 dirProj = dProj*normalize(normal);
    lineNormalLen = length(dirProj);
    lineNormal = vec2(-dirProj.y, dirProj.x) / lineNormalLen;
    pointScreenSize = clamp(2*pointPixelScale*modifiedPointRadius / p.w,
minPointSize, maxPointSize);
    markerShape2 = markershape;

//RGB
Color//////////////////////////////////////////////////////////////////
//////
    if (colorMode == 0)
        pointColor = color;

//Intensity Color with
HSV////////////////////////////////////////////////////////
    else if (colorMode == 1)
        pointColor = Rainbow(prop,0,1);

//RGB and Intensity
Blending/////////////////////////////////////////////////////////
    else if (colorMode == 2)
        pointColor = (color*alpha)+(prop*vec3(1))*(1.0-alpha);
```

```
//Uncertainty
Color//////////////////////////////////////////////////////////////////
////
    else if (colorMode == 3){
      float incidenceAngle;
      float BWrangeSigma;
      float RangeVAR;
      float VertVAR;
      float HorizVAR;
      vec3 ScanRay;
      mat3 A;
      mat3 B;
      mat3 C;
      float DotPrdct;
      float Range = sqrt(pow((ScanOrigin[0]-
position[0]),2)+pow((ScanOrigin[1]-position[1]),2)+pow((ScanOrigin[2]-
position[2]),2));
      float VertAngle;
      float HorzAngle;
      vec3 AdjNormal;
      int NoNormal=0;
      float error_x;
      float error_y;
      float error_z;
      float error;

      //Calculate BW angular error
      float BWangleSigma = (BeamDivergence/1000.)/4.;
      //float BWangleSigma=0.;

      //Calculate Horizontal Angle from Position Coordinates
      if (position[0] !=0.0){
          HorzAngle = atan2(position[1], position[0]);
          if (HorzAngle < 0.0) {
              HorzAngle = 2 * PI + HorzAngle;
          }
      }

      //Calculate Vertical Angle form Position Coordinates
      VertAngle = asin(position[2] / Range);

      //Calculate Incidence Angle
      ScanRay=ScanOrigin-position;
      ScanRay = normalize(ScanRay);

      DotPrdct = dot(ScanRay,normal);

      incidenceAngle=acos(DotPrdct);
      if(incidenceAngle == PI)
          incidenceAngle = 1.0;
      //Check for flipped inverse normals and flip them back
      if(incidenceAngle > PI*0.5){
```

```
        AdjNormal = normal*-1;
        DotPrdct = dot(ScanRay,AdjNormal);
        incidenceAngle=acos(DotPrdct);
    }
    if(incidenceAngle > 85*(PI/180.))
        incidenceAngle = 85*(PI/180.);

    //Calculate BW range error
    BWrangeSigma=(1./4.)*(exitDiameter+Range*(BeamDivergence/1000.))*tan
(incidenceAngle);
    //BWrangeSigma = 0.;

    //Identify points where a normal vector was not able to be
calculated and flag them
    if(length(normal)==0){
        BWrangeSigma = 0;
        NoNormal = 1;
    }
    //Calculate the 10ppm range sigma
    float RangeSigmaPPM = RangeSigma +(Range*(RangePPM/1000000));

    //Convert VertSigma and HorizSigma to Radians
    float VertSigmaRAD = VertSigma*(PI/180.);
    float HorizSigmaRAD = HorizSigma*(PI/180.);

    //Generate combined variances
    RangeVAR = pow(RangeSigmaPPM, 2)+ pow(BWrangeSigma, 2);
    VertVAR = pow(VertSigmaRAD, 2) + pow(BWangleSigma,
2)+pow(IclinationSigma*(PI/180.),2);
    HorizVAR = pow(HorizSigmaRAD, 2) + pow(BWangleSigma,
2)+pow(IclinationSigma*(PI/180.),2);

    // Propagate Uncertainty with GLOPAV (Adjustment Calculations,
Ghilani, 2010)

    //Jacobian Matrix
    A[0][0]= cos(VertAngle)*cos(HorzAngle);
    A[1][0]= -Range*sin(VertAngle)*cos(HorzAngle);
    A[2][0]= -Range*cos(VertAngle)*sin(HorzAngle);
    A[0][1] = cos(VertAngle)*sin(HorzAngle);
    A[1][1] = -Range * sin(VertAngle)*sin(HorzAngle);
    A[2][1] = Range * cos(VertAngle)*cos(HorzAngle);
    A[0][2] = sin(VertAngle);
    A[1][2] = Range * cos(VertAngle);
    A[2][2] = 0.;

    //Stocastic model
    B[0][0] = RangeVAR;
    B[1][0] = 0.;
    B[2][0] = 0.;
    B[0][1] = 0.;
    B[1][1] = VertVAR;
```

```
        B[2][1] = 0.;
        B[0][2] = 0.;
        B[1][2] = 0.;
        B[2][2] = HorizVAR;

        //Generate Covariance Matrix for each point
        C = A*B*transpose(A);
        error_x = sqrt(abs(C[0][0]));
        error_y = sqrt(abs(C[1][1]));
        error_z = sqrt(abs(C[2][2]));

        // Uncertainty visualization Mode 1 (HSV Rainbow with RGB)
        if(UncertViz == 0){
                if(UncertType == 1)
                        error = (sqrt(pow(error_x,2) + pow(error_y,2)))*1.5158;
                else if(UncertType == 2)
                        error = error_z;
                else if(UncertType == 0)
                        error = (sqrt(pow(error_x,2) + pow(error_y,2) +
pow(error_z,2)))*1.8786;

        //Color points flagged as having no normal vector as background
color
        if(NoNormal ==1){
                pointColor = vec3(0.235,0.196,0.192);
                NoNormal =0;
        }
        else
                pointColor =
(GrayScaleColor(color)*alpha)+Rainbow(error,Low,High)*(1.0-alpha);

        }

        //Uncertainty visualization Mode 2 (Transparent based on error
threshold)
        if(UncertViz == 1){
                if(UncertType == 1)
                        error = (sqrt(pow(error_x,2) + pow(error_y,2)))*1.5158;
                else if(UncertType == 2)
                        error = error_z;
                else if(UncertType == 0)
                        error = (sqrt(pow(error_x,2) + pow(error_y,2) +
pow(error_z,2)))*1.8786;

                vec3 BackgrndColor = vec3(0.235,0.196,0.192);
                //vec3 BackgrndColor = vec3(1,1,1);

                if(NoNormal ==1){
                        pointColor = vec3(0.235,0.196,0.192);
                        NoNormal =0;
                }
```

```
            else if(error<High)
                    pointColor = color;
            else
                    pointColor = BackgrndColor;



       }

}

//Incidence Angle
Visualization//////////////////////////////////////////////////////
else if (colorMode == 4){
      vec3 FromOrigin=vec3(0.,0.,0.)-position;
      vec3 AdjNormal;
      int flag = 0;

      //First check if any normals are flipped from origin by calculating
incidence angle
      FromOrigin = normalize(FromOrigin);
      float DotPrdct = dot(FromOrigin,normal);

      float incidenceAngle=acos(DotPrdct);
      if(incidenceAngle == PI)
            incidenceAngle = 1.0;
      if(incidenceAngle > PI*0.5){
            AdjNormal = normal*-1.;
            DotPrdct = dot(FromOrigin,AdjNormal);
            incidenceAngle=acos(DotPrdct);
      }
      else
            AdjNormal = normal;

      //Recalculate incidence angle based on adjustable scan position
      vec3 ScanRay = ScanOrigin-position;
      ScanRay = normalize(ScanRay);
      DotPrdct = dot(ScanRay,AdjNormal);
      incidenceAngle=acos(DotPrdct);
      if(incidenceAngle == PI)
            incidenceAngle = 1.0;

      //Check if new incidence angle means moved scan position has been
placed behind a surface, make points background color
      if(incidenceAngle > PI*0.5)
            flag =1;

      if(flag == 1){
            pointColor = vec3(1.,1.,1.);
            flag = 0;
      }
      else{
            incidenceAngle *=(180/PI);
```

```
            pointColor =
(GrayScaleColor(color)*alpha)+vec3((incidenceAngle/90.),(1-
(incidenceAngle/90.)),0)*(1.0-alpha);


    }
}

//Horizontal Angle
Visualization//////////////////////////////////////////////////////
else if (colorMode == 5){

        //Calculate Horizontal and Vertical Angle from Position
Coordinates
    float HorzAngle;
    if (position[0] !=0.0){
        HorzAngle = atan2(position[1], position[0]);

        if (HorzAngle < 0.0) {
            HorzAngle += (2 * PI);
        }
    }


    pointColor = (GrayScaleColor(color)*alpha)+Rainbow(((2*PI)-
HorzAngle),0.0,(2*PI))*(1.0-alpha);

}

//Vertical Angle
Visualization//////////////////////////////////////////////////////
else if (colorMode == 6){

    //Calculate Horizontal and Vertical Angle from Position Coordinates
    float VertAngle;
    float Range = sqrt(pow((ScanOrigin[0]-
position[0]),2)+pow((ScanOrigin[1]-position[1]),2)+pow((ScanOrigin[2]-
position[2]),2));

    VertAngle = asin(position[2] / Range);
    float VertAngleDeg = VertAngle*(180./PI);


    pointColor = (GrayScaleColor(color)*alpha)+Rainbow(VertAngleDeg,-
55.,45.)*(1.0-alpha);



}
else if (colorMode == 7){
```

```
      float Range = sqrt(pow((ScanOrigin[0]-
position[0]),2)+pow((ScanOrigin[1]-position[1]),2)+pow((ScanOrigin[2]-
position[2]),2));

      float R=clamp(Range,minRange,maxRange);

      R=(R-minRange)/(maxRange-minRange);
      pointColor = (GrayScaleColor(color)*alpha)+vec3(R,0.,1.-R)*(1.0-
alpha);

}

if(NormalsOn==0)
      NormalFlag=1;


    // Ensure zero size points are discarded.  The actual minimum point
size is
    // hardware and driver dependent, so set the markerShape2 to discarded
for
    // good measure.
    if (pointScreenSize <= 0)
    {
        pointScreenSize = 0;
        markerShape2 = -1;
    }
    else if (pointScreenSize < 1)
    {
        // Clamp to minimum size of 1 to avoid aliasing with some drivers
        pointScreenSize = 1;
    }
    gl_PointSize = pointScreenSize;
    gl_Position = p;

}

//------------------------------------------------------------------------
------
#elif defined(FRAGMENT_SHADER)

uniform float markerWidth = 0.3;

flat in float modifiedPointRadius;
flat in float pointScreenSize;
flat in vec3 pointColor;
flat in int markerShape2;
flat in vec2 lineNormal;
flat in float lineNormalLen;
flat in int NormalFlag;

out vec4 fragColor;
```

```
// Limit at which the point is rendered as a small square for antialiasing
// rather than using a specific marker shape
const float pointScreenSizeLimit = 2;
const float sqrt2 = 1.414213562;

void main()
{
if (NormalFlag == 1){
    if (pointScreenSize <= 0)
        discard;
    if (pointScreenSize > pointScreenSizeLimit)
    {
        float w = markerWidth;
        if (pointScreenSize < 2*pointScreenSizeLimit)
        {
            // smoothly turn on the markers as we get close enough to see
them
            w = mix(1, w, pointScreenSize/pointScreenSizeLimit - 1);
        }
        vec2 p = 2*(gl_PointCoord - 0.5);
        p.y = -p.y;
        float r = length(p);
        const float lineRad = 1.0;
        bool inLine = r*(1-w) < max(0.5*lineNormalLen, 2/pointScreenSize)
&&
                abs(dot(lineNormal,p))*(1-w)*(pointScreenSize) < lineRad;
        if (!inLine)
            discard;
    }

    fragColor = vec4(pointColor, 1);

}
else{
    if (markerShape2 < 0) // markerShape2 == -1: discarded.
        discard;
    // (markerShape2 == 1: Square shape)
#   ifndef BROKEN_GL_FRAG_COORD
    gl_FragDepth = gl_FragCoord.z;
#   endif
    if (markerShape2 != 1 && pointScreenSize > pointScreenSizeLimit)
    {
        float w = markerWidth;
        if (pointScreenSize < 2*pointScreenSizeLimit)
        {
            // smoothly turn on the markers as we get close enough to see
them
            w = mix(1, w, pointScreenSize/pointScreenSizeLimit - 1);
        }
        vec2 p = 2*(gl_PointCoord - 0.5);
        if (markerShape2 == 0) // shape: .
        {
```

```
            float r = length(p);
            if (r > 1)
                discard;
#           ifndef BROKEN_GL_FRAG_COORD
            gl_FragDepth += projectionMatrix[3][2] *
gl_FragCoord.w*gl_FragCoord.w
                            // TODO: Why is the factor of 0.5 required
here?
                            * 0.5*modifiedPointRadius*sqrt(1-r*r);
#           endif
        }
        else if (markerShape2 == 2) // shape: o
        {
            float r = length(p);
            if (r > 1 || r < 1 - w)
                discard;
        }
        else if (markerShape2 == 3) // shape: x
        {
            w *= 0.5*sqrt2;
            if (abs(p.x + p.y) > w && abs(p.x - p.y) > w)
                discard;
        }
        else if (markerShape2 == 4) // shape: +
        {
            w *= 0.5;
            if (abs(p.x) > w && abs(p.y) > w)
                discard;
        }
    }

        fragColor = vec4(pointColor, 1);
}
}
#endif
```